This is to certify that the

thesis entitled

STRUCTURE AND MIXING IN A
LOW REYNOLDS NUMBER FORCED WAKE
IN A CONFINING CHANNEL

presented by

KIRK E. NELSON

has been accepted towards fulfillment
of the requirements for

MS degree in Mech. Engr.

M. M. Koochesfahani

Major professor

Date Aug. 23, 1996

STRUCTURE AND MIXING IN A LOW REYNOLDS NUMBER FORCED WAKE IN A CONFINING CHANNEL

By

Kirk E. Nelson

A THESIS

Submitted to
Michigan State University
in partial fulfillment of the requirements
for the degree of

MASTER OF SCIENCE

Department of Mechanical Engineering

1996

ABSTRACT

STRUCTURE AND MIXING IN A LOW REYNOLDS NUMBER FORCED WAKE IN A CONFINING CHANNEL

By

Kirk E. Nelson

The mixing field of a forced, low Reynolds number ($Re_\theta \approx 100$) splitter plate wake is studied using chemically reacting laser induced fluorescence. Results indicate that forcing one free stream at high amplitude greatly increases the amount of scalar mixing downstream. At the farthest downstream location investigated the wake forced at 9% amplitude exhibits about sixteen times more chemical product than the unforced wake at the same location. Three-dimensionality originating from the test section side walls is primarily responsible for this increase in mixing. Marked three-dimensionality resulting in increased mixing is also observed in a higher Reynolds number wake flow.

Two additional wake flows, one employing a false wall in the test section and another using a peg near the splitter plate tip, are also studied. Both flows produce streamwise vorticity providing other examples of no-slip boundaries leading to wake three-dimensionality and increased mixing.

ACKNOWLEDGMENTS

This thesis would not have been possible without the help of numerous individuals. First on the list is my advisor, Dr. Manooch Koochesfahani. His advice, knowledge, and guidance throughout my Master's research has been invaluable. I am also indebted to Drs. J.F. Foss and M. Zhuang for reviewing this manuscript. Thanks to everyone in the lab, past and present: Greg Ambrose, Steve Beresh, Rich Cohn, Chuck Gendrich, Greg Katch, Scott Krueger, Figen Lacin, Bernd Stier, and especially Colin MacKinnon whose mastery of the shear layer facility made things much easier for me.

My parents, Paul and Brenda Nelson, deserve special thanks for putting up with me all these years. The patience and companionship of my family and friends is also greatly appreciated.

The experimental facilities and image acquisition system used for this study were purchased with funding provided by the Air Force Office of Scientific Research.

TABLE OF CONTENTS

LIST OF TABLES

LIST OF FIGURES

LIST OF SYMBOLS

Symbol	*Description (page or Figure of first reference)*
A	test section cross-sectional area (12)
A_m	mixed-fluid area (12)
A_1	1% area (24)
A_P	product area (23)
C_d	instantaneous dye concentration (19)
C_{do}	free stream dye concentration (22)
C_P	product concentration (18)
$(C_P)_{max}$	product concentration at fluorescence turn on threshold (18)
C_P^*	normalized product concentration (22)
$\overline{C_P^*}$	mean normalized product concentration (23)
d	peg diameter (71)
f	forcing frequency (6)
f_o	wake natural roll up frequency (6)
g	gravitational acceleration (19)
h	peg height (71)
I	pixel intensity (19)

I_{corr}	corrected pixel intensity (22)
I_f	fluorescence intensity (18)
$(I_f)_{max}$	intensity at fluorescence turn on threshold (18)
I_{fo}	intensity corresponding to free stream dye concentration (22)
I_{ref}	intensity from uniform concentration reference image (22)
K_a	acid dissociation constant (91)
k	intensity correction scaling factor (22)
M_A	molarity of the acid solution (90)
M_B	molarity of the base solution (90)
n	number of absorbing dye molecules at time t (79)
n_o	number of absorbing dye molecules at time t = 0 (79)
n_A	number of moles of acid (90)
P_0	probability of pure lower stream fluid (12)
P_1	probability of pure upper stream fluid (12)
P_m	probability of mixed fluid (12)
Re_θ	Reynolds number based on momentum thickness at the splitter plate tip: $U_o\theta/\nu$ (6)
Ri	Richardson number: $\dfrac{\Delta\rho g\delta}{\bar{\rho}U_o^2}$ (19)
t	time (22)
Δt	time between fields (41)
T	total length of time record
U_o	wake free stream velocity (Fig. 1)
U_1	shear layer high speed stream velocity (Fig. 1)

U_2	shear layer low speed stream velocity (Fig. 1)
$\bar{u}(y)$	mean streamwise velocity at y (Fig. 1)
V_{peak}	three-dimensionality propagation velocity (94)
v_A	acid volume (78)
v_B	base volume (78)
x	streamwise coordinate (Fig. 1)
x^*	nondimensional streamwise coordinate: xf/U_o (39)
y	transverse coordinate (Fig. 1)
z	spanwise coordinate (Fig. 8)
z_{peak}	spanwise location of δ_P maxima (94)
α	dye absorption coefficient (19)
γ	consecutive rows below free stream intensity for image filtering (83)
δ_1	wake 1% thickness (24)
$\langle\delta_1\rangle$	span-averaged wake 1% thickness (51)
δ_m	mixed-fluid thickness (24)
δ_P	product thickness (23)
$\langle\delta_P\rangle$	span-averaged product thickness (51)
δ_{P1}	product thickness referenced to the upper free stream (24)
δ_{P2}	product thickness referenced to the lower free stream (24)
ϵ	velocity/frequency correction factor (39)
ε_o	dye molar absorption coefficient (19)
ζ	change in molarity due to reaction (91)

θ	momentum thickness (xvii)
λ	initial wake roll up wavelength (39)
ν	kinematic viscosity (xvii)
ξ	fluid concentration (81)
ξ_B	base volume fraction (18)
ξ_S	concentration at fluorescence turn on threshold (Fig. 6)
ρ	fluid density (19)
$\Delta\rho$	density difference between the two fluid streams (19)
$\bar{\rho}$	mean fluid density (19)
τ_b	dye bleaching time constant (79)
ω	vorticity (3)

Chapter 1

INTRODUCTION

This study is concerned with the mixing field resulting from forcing a confined wake. Wakes resulting from a splitter plate are a special case of a two-stream shear layer, which is illustrated in Figure 1a. A two-stream shear layer arises when two fluid streams of different velocity interact downstream of a thin interface—for example a splitter plate. A wake results when the two fluid streams have the same velocity, as shown in Figure 1b.

Both wakes and shear layers occur in many natural and manmade phenomena. Chemical lasers and combustors are two important applications. Both applications rely on the mixing of reacting species; therefore, methods either to enhance or to control molecular mixing in shear layers and wakes are of paramount importance.

Wakes are inherently unstable and shed vortices from the splitter plate tip at high enough Reynolds number. One result of this vorticity is an increase in the length of the passive scalar interface between the two fluids, thus an increase in chemical reaction and combustion downstream. For relatively low Reynolds number, though, the vorticity is not strong enough to elicit strong mixing. Introducing an external perturbation into one or both streams, however, can introduce stronger vorticity that results in not only a further increase in interface area, but also an amplification of three-dimensionality in the flow due to vortex stretching and reorientation. This three-dimensionality is accompanied by an increase in small scales and a dramatic increase in molecular mixing compared with the unforced wake (Roberts, 1985; MacKinnon & Koochesfahani, 1993).

Experimenters have used two primary methods to introduce three-dimensionality into the nominally two-dimensional wake flow. The first method relies on a spanwise periodic disturbance to generate streamwise vorticity (e.g., Meiburg & Lasheras, 1988; Weygandt & Mehta, 1995). The second method relies on the interaction of the spanwise vortices with the flow facility side walls to generate streamwise vorticity (e.g., Roberts, 1985; MacKinnon & Koochesfahani, 1993). This second method was used for the present study and required oscillating one approach stream at sufficiently high amplitude to generate strong spanwise vorticity.

The purpose of this study is to measure the molecular mixing in a wake using an acid-base reaction between the two free streams and a pH sensitive dye. More specifically, the present study investigates how the interposition of a nominally two-dimensional disturbance of varying amplitude affects the downstream evolution and mixing in the wake. The following sections give a historical summary of the work to date related to the present study. This historical research can be divided into three areas: natural shear layers and wakes, forced shear layers and wakes, and mixing in shear layers and wakes. The final section of Chapter 1 discusses the specific goals of the present study.

1.1 Natural Shear Layers and Wakes

The study of wakes dates back several decades. In 1954 Roshko showed that coherent vortical structures exist in the wakes of two-dimensional bodies at moderate to high Reynolds number. These observations were confirmed and expanded by Townsend (1956), Taneda (1959), and Morkovin (1964). Many of these early investigators noted periodic signals in hot wire data that suggested some kind of random secondary structure. Grant (1958) concluded that the turbulent wake, after first being dominated by an essentially two-dimensional Kármán vortex street, began to develop three-dimensionality as counterrotating vortices inclined to the wake. The onset of three-dimensionality also appeared to be coupled to turbulence transition. Cimbala et al. (1988), using smoke-wire visualization, also observed three-dimensionality in the wake of a circular cylinder. Their plan views of a Re = 150 wake show three-dimensionality downstream of x/d = 100. Three-dimensionality seems to occur at lower x/d for higher Reynolds number (Re = 190), where the wake becomes turbulent, although the investigators never suggest this in their report.

Hayakawa & Hussain (1989) conjectured that three-dimensionality should exist even in the near field of a turbulent wake. Their experiments, in fact, proved this by finding significant three-dimensionality in the moderately near field (x/d = 20) of a turbulent (Re = 1.3×10^4) cylinder wake. These investigators, using X-wire rakes, found concentrations of transverse vorticity (ω_y) with strengths and scales comparable to the spanwise vorticity (ω_z). Based on these and earlier observations, they concluded that their data showed strong three-dimensionality in the wake caused by longitudinal 'ribs' formed in the braid regions connecting the spanwise structures.

Recently, Williamson (1992) has extensively studied wake three-dimensionality. Williamson and his colleagues initially noted the presence of spot-like 'vortex dislocations' that appeared at random locations in the wake of a circular cylinder. These dislocations were caused by adjacent spanwise vortex cells shedding at different frequency causing a localized discontinuity in the spanwise structure. To study these structures in a controlled manner, Williamson triggered the vortex dislocations by placing a ring of larger diameter at a fixed location on the cylinder. This created a localized difference in shedding frequency, and effectively triggered symmetric vortex dislocations downstream of the ring. Excellent flow visualization photographs clearly show the stretching and reorientation of the primary vortex tubes caused by the dislocation. Williamson concluded that the vortex dislocations are an essential element in wake transition. Also, the similarity of the vortex dislocations to structures observed in shear layers (see Browand & Troutt; 1980, 1985) suggests that they may be a feature common to all shear flows.

Interest in shear layers and wakes produced by splitter plates was spurred by the results of Brown & Roshko (1971, 1974). Their shadowgraph pictures show the presence of large, coherent, spanwise structures developing from the splitter plate tip and convecting downstream. Dimotakis and Brown (1976) furthered this research by showing that these structures persist up to high Reynolds number: 3×10^6 based on the high speed stream velocity and downstream distance. Another finding was that these large structures play an important role in the entrainment process. The structures pull initially irrotational fluid into the shear layer where rapid mixing then occurs.

Konrad (1976), in a gas layer, and Breidenthal (1978, 1981), in a liquid layer, used methods to investigate the molecular mixing in shear layers. These researchers found a dramatic increase in mixing at some distance downstream of the splitter plate that seemed coupled to the presence of a streamwise disturbance. Breidenthal suggested that the streamwise structures were pairs of counterrotating streamwise vortices. Furthermore, he postulated that these structures were responsible for increased small-scale motions in the shear layer. Streamwise structures of this type had previously been observed by Bradshaw (1966) and Miksad (1972). Most of these researchers observed the streamwise structures in plan view. Bernal (1981), however, was the first to observe the streamwise structures in cross-sectional view of the mixing layer.

Because the streamwise structures seemed to be coupled to the rapid increase in mixing led to a more thorough investigation of their origin and characteristics. Lasheras, et al. (1986) concluded that the streamwise vortices originated from upstream disturbances. The streamwise structures appeared first in the braid regions connecting the cores of the spanwise structures, then propagated to the cores themselves. Bernal & Roshko (1986) also concluded that the streamwise vortices originated from available upstream disturbances. Also, by studying the onset of the structures under many flow characteristics they found that the critical Reynolds number for the streamwise structures decreased with the shear layer velocity ratio. In other words, wake flows exhibit more three-dimensionality than shear layers.

1.2 Forced Shear Layers and Wakes

Some early results from forcing a shear layer are reported in Ho & Huang (1982) and Oster & Wygnanski (1982). These researchers showed that forcing the shear layer at its natural frequency, or a subharmonic of its natural frequency, would lead to very different growth characteristics compared with the unforced case. In addition, Oster & Wygnanski showed that changing the forcing *amplitude* would also alter the shear layer development.

This work was extended by Roberts (1985) who studied wakes forced at several frequencies by oscillating one fluid stream. Roberts' forcing method, it should be pointed out, was effectively the same as the present study. His chemically reacting laser induced fluorescence (LIF) photographs of a $Re_\theta = 160$ wake show some very interesting results. The unforced flow exhibits a "somewhat tenuous Kármán vortex street with mixing occurring on a thin interface" (Roberts, 1985). Forcing the flow at a frequency close to its natural frequency (in his study, $f = 4.4$ Hz; $f_o = 5$ Hz) results in a more organized version of the natural flow. The interface becomes more tightly rolled-up, suggesting increased vorticity. Forcing at less than the natural frequency ($f = 1.7$ Hz) produces a double Kármán vortex street: structures form at a frequency close to the natural frequency and are modulated at the forcing frequency. The tendency for amalgamation of these structures in a shear layer (see Ho & Huang, 1982) is not seen in Roberts' wake photograph. In cases where the forcing frequency is higher than the natural frequency (f = 6.5, 9.8 and 10.75 Hz) a noticeable breakdown in the large structures is seen. Also evident is a dramatic increase in the amount of product (mixing) accompanying the breakdown. The highest forcing frequency also shows a new, larger scale vortex street downstream of the breakdown. Plan views of the wake at this Reynolds number show the test section side walls are largely responsible for introducing three-dimensionality into the flow.

In contrast to Roberts, MacKinnon & Koochesfahani (1993) examined the effects of changing the forcing *amplitude*. Their experiments investigate a $Re_\theta \approx 100$ wake forced at near its natural frequency ($f = f_o$ = 6 Hz). Forcing was achieved by oscillating one fluid stream using an electromagnetic bellows mechanism—the same mechanism used in the present work. Using the nonreacting LIF technique they found that increases in the forcing amplitude led to dramatic changes in both the resulting flow structure and the amount of molecular mixing achieved. Like Roberts, they also observed that wake/side wall interaction led to the formation of streamwise vorticity and the resultant increased mixing.

Another, perhaps more direct, method of introducing streamwise vorticity into wakes and shear layers is perturbing the flow at or near the splitter plate tip. Lasheras & Choi (1988), studying a shear layer, and Meiburg & Lasheras (1988), studying a wake, both used this type of forcing. To produce streamwise vorticity they used splitter plates with tips either corrugated (vertical undulation) or indented (horizontal undulation) at various frequencies and amplitudes. Both investigations employed a test section 9 cm high × 25 cm wide to intentionally de-emphasize side wall effects. They concluded that in this forcing configuration, the Kelvin-Helmholtz instability developed first, leading to the familiar nearly two-dimensional spanwise vortex structures. The secondary streamwise instability developed from the strain field existing in the braid regions of the primary structures. Because the spanwise vortex tubes remain essentially two-dimensional during the development of streamwise vorticity, the investigators concluded that the two instabilities are nearly independent of one another.

A similar approach was used by Nygaard and Glezer (1991). They used a heater mosaic on the splitter plate surface to impose spanwise disturbances into a shear layer. Their research shows that the streamwise vortices resulting from the upstream perturbation are accompanied by distortions in the mean streamwise velocity field. These distortions result in spanwise-periodic flow regions where perturbations are amplified and subsequently break down to small-scale motion. Nygaard and Glezer believe this breakdown leads to mixing transition farther downstream.

Although investigators have used many methods to force wakes and shear layers two characteristics seem universal: forcing alters the structure and development of these flows, and three-dimensionality (as streamwise vortices) is instrumental in enhancing the mixing in these flows.

1.3 Mixing in Shear Layers and Wakes

Most of the studies of shear layers and wakes to date have concentrated on the transport properties of these flows, such as the velocity fields, the vorticity fields, the Reynolds stresses, etc. A much smaller body of work exists related to the actual mixing properties of these flows. However, mixing is an important feature of these flows especially in combustion and chemical reactions.

Koochesfahani (1984) built on the foundation laid out first by Konrad (1976) and Breidenthal (1978, 1981) using a new technique: laser induced fluorescence. Although the chemically reacting version of LIF was incorporated on a limited basis, Koochesfahani's work primarily employed the passive scalar, nonreacting version of LIF. In nonreacting LIF one fluid stream is premixed with a fluorescent dye that becomes diluted downstream of the splitter plate due to mixing with the other fluid stream. A laser is used to excite the dye and the resulting fluorescence is recorded. The average concentration within a finite sampling volume, for example that imaged in one pixel, is the ratio of fluorescence at that point to the free stream fluorescence. As noted by Breidenthal (1981), the passive scalar technique will always overestimate mixing if the recording device is unable to resolve the smallest mixing scales of the flow. Consider, for example, the situation illustrated in Figure 2. Imagine that each of the three large rectangles represents one imaging pixel. In each case the average concentration in the three large rectangles is the same, but only one of these cases is uniformly mixed at 1:1. The nonreacting LIF technique would consider *all of the cases* in Figure 2 to be mixed 1:1 (cf. Koochesfahani & Dimotakis, 1985). Despite its limitations, the nonreacting LIF technique remains a quick and simple method for finding the concentration field of a shear layer or wake.

Roberts (1985) extended the use of LIF to study the mixing in forced shear flows. One of his test cases, a moderate Reynolds number wake ($Re_\theta = 160$) forced at 9.8 Hz (about twice the natural frequency), clearly showed an increase in mixing over the unforced case. Passive scalar LIF measurements at the wake centerline found a mixing increase of more than an order of magnitude for the highly mixed case over the unforced flow.

Roberts attributed much of this product increase to the streamwise vorticity generated by reorientation of the spanwise vortex structures near the side walls of the test section. Figure 3, reproduced from Roberts (1985), shows this side wall effect very clearly in plan view. Moving downstream, the regions of the wake exhibiting the most mixing convect away from the side walls toward midspan. These highly mixed regions eventually merge at the test section midspan. Downstream of this location the greatest mixing in the wake is concentrated in about the central one-third of the test section. A single cross-stream image of the same flow as in Figure 3 taken at x = 12 cm, although somewhat blurry, shows evidence of pairs of counterrotating streamwise vortices. Roberts proposed that the no-slip condition imposed on the flow at the side walls caused the spanwise structures to be tipped in the walls' boundary layers. This tipping produces pairs of streamwise vortices with opposite signs. Mutual induction of these vortices cause them to move away from the side walls. The vortex pairs move toward midspan quickly at first, but begin to slow as they approach the vortex pair originating from the other side wall. Eventually an equilibrium condition is reached where no further spanwise displacement is observed. The result is a wake that is highly mixed in the center of the test section, but with virtually no mixing near the side walls (Roberts, 1985; Roberts & Roshko, 1985).

Intrigued by the highly mixed flow caused by the side wall/vortex interaction, Roberts conducted an experiment to test the effect of the wall boundary layer thickness on the wake development. To do this, he placed a false side wall within the test section. A triangular notch was cut into the false wall so that its leading edge was 3 cm upstream of the splitter plate tip. With this setup the boundary layer had only developed for 3 cm at the tip of the splitter plate for the false wall, in contrast to approximately 60 cm for the test section true walls. Phenolphthalein flow visualization photographs revealed that although the flow was no longer symmetric, the vortex tipping process still occurred on the false wall. From these observations Roberts concluded that a no-slip condition alone was sufficient to reorient the spanwise vorticity, and thus, produce a highly mixed wake flow (Roberts, 1985).

Roberts' work contains much useful information. Unfortunately, it does not provide much quantitative data, especially dealing with wake flows. The first investigation concentrated on quantifying the mixing field of a forced wake is that of MacKinnon and Koochesfahani (1993). This study uses the nonreacting (passive scalar) LIF technique to investigate the sensitivity of $Re_\theta \approx 100$ wake flows to forcing amplitude. In contrast to Roberts' work, MacKinnon and Koochesfahani kept a fixed forcing frequency (the natural wake roll-up frequency $f = f_o$) while varying the forcing amplitude. Cross-stream (spanwise) flow image sequences were recorded at five distinct downstream x locations. At each location the wake was forced at three different forcing amplitudes (velocity perturbation RMS amplitude) corresponding to 1.6%, 5.6%, and 9.1% of the free stream flow speed. Besides the forced cases, the unforced wake was investigated for comparison.

Quantities of interest were calculated by statistically evaluating the image sequences. The primary statistical tool used in nonreacting LIF is the probability density function (pdf) of the concentration field. Other quantities can be calculated from the pdf, such as the total mixed-fluid probability $P_m(y, z)$, and the probabilities of finding fluid from either the lower or upper free streams $P_0(y, z)$ and $P_1(y, z)$. Another quantity, the mixed-fluid area A_m, can be found from the span-averaged pdf. Dividing A_m by the test section cross-sectional area A results in the fraction of the test-section occupied by mixed fluid. A plot of A_m/A as a function of downstream distance, reproduced from MacKinnon and Koochesfahani (1993), is shown in Figure 4. Notice that the value of the mixed-fluid fraction A_m/A can be as high as 41% for the wake forced at 9.1% amplitude at a downstream distance of x = 24 cm. This value represents more than an order of magnitude increase over the unforced case at the same location.

The work of MacKinnon and Koochesfahani conclusively proves that forcing a wake, especially at high amplitude, can drastically increase the amount of molecular mixing downstream. It does not, however, provide mixing data that can be considered reliable on an absolute basis. Their investigation used the nonreacting LIF method, which always provides an upper bound on the actual amount of mixing. To get reliable mixing measurements using LIF it is necessary to use the chemical reaction method.

1.4 Objectives of the Current Work

It is the objective of this report to provide quantitative data on the actual amount of chemical product in a $Re_\theta \approx 100$ wake perturbed at various forcing amplitudes. All product calculations are based on the reacting LIF technique; therefore, they are not subject to the inherent limitations of the nonreacting technique. Mixing measurements are calculated from image sequences with a laser sheet illuminating the xy-plane (streamwise imaging) and the yz-plane (spanwise imaging) at several locations. These measurements are the chemically reacting LIF analogs of the measurements of MacKinnon & Koochesfahani (1993), which were performed in the same flow facility using the same forcing method. In addition, mixing measurements are made for a higher Reynolds number wake flow in a similar manner.

In addition to the quantification of the mixing field in the wake, this work provides significant information regarding the structure of the forced wake in the form of flow images. Pictures illustrating the forced wake at different amplitudes in both streamwise and spanwise views are included. Additionally, passive scalar, spanwise flow images are presented for two extensions to the base flow situation. The first extension uses a thin vertical plate mounted in the test section downstream of the splitter plate tip. This vertical plate is similar to Roberts' 'false wall.' The second extension uses a small cylindrical peg mounted on the upper surface of the splitter plate to produce a secondary, three-dimensional disturbance in the wake. These two extensions are investigated to further examine the effects of forcing, especially no-slip boundaries, on the structure and mixing of the wake.

Chapter 2

EXPERIMENTAL FACILITY AND INSTRUMENTATION

All of the experiments used for this study were performed in the Turbulent Mixing Laboratory's small liquid shear layer facility. Experiments executed in this facility have previously been reported by Koochesfahani & MacKinnon (1991), MacKinnon & Koochesfahani (1993), and Katch (1994). The present study is based on results from both streamwise and spanwise imaging. This chapter will explain the experimental facility, forcing mechanism, diagnostics, and data reduction used for these two imaging setups.

2.1 Experimental Facility

All of the experiments were performed in the gravity-driven, liquid, two-stream shear layer facility illustrated in Figure 5. Fluid for the two streams was pumped from two 210 L barrels into overhead, constant head supply tanks placed approximately 2.5 m above the test section. These overhead tanks were connected to the contraction by flexible hoses. Beyond the splitter plate tip, the two streams mix in the test section and exit the facility through a hose discharging into a downstream, constant head dump tank. The acrylic test section used in this study had inside dimensions of 4 cm (height) × 8 cm (width) × 32 cm (length).

The flow rate through the facility was controlled by three valves: one each along the two fluid supply lines upstream of the contraction, and one downstream of the test section. Two separate wake speeds were investigated: $U_o = 10$ cm/s and $U_o = 20$ cm/s. Throughout this report the nominally 10 cm/s wake and the 20 cm/s wake will be termed the 'low speed' and 'higher speed' wakes, respectively. The Reynolds number Re_θ based on the momentum thickness at the splitter plate tip has been previously determined from LDV data to be approximately 100 for this facility for the low speed wake. MacKinnon & Koochesfahani (1993) found these conditions result in a natural Kármán roll-up frequency of about 6 Hz. The present investigation found the value to be closer to 7 Hz. Uniform, laminar flow was ensured in both streams by using a series of honeycombs and fine screens upstream of the contraction. Extreme care was taken in filling the test section to reduce bubbles and air pockets that could upset the symmetry and flow characteristics of the approach streams.

A titration reference chamber was placed on top of the test section during each experiment. The chamber was required because, unlike nonreacting LIF, the maximum intensity $(I_f)_{max}$ is not available in the test section during the experiments. The titration reference chamber is a rectangular glass container with an adjustable cover. Before each experiment the chamber was filled with 1.5 L of fluid from the acid/dye supply reservoir. Fluid from the base reservoir was then added until the intensity maximum was achieved. During the titration and the experimental runs the fluid in the reference chamber was continuously mixed with an electric stirrer to ensure both a uniform mixture and to reduce the effects of dye photobleaching (see Appendix A).

2.2 Forcing Mechanism

Forcing was achieved by an oscillating bellows mechanism positioned in the upper stream supply line slightly upstream of the honeycombs and screens (see Figure 5). The motion of the bellows was controlled by a magnetic coil vibrator and amplifier (Vibration Test Systems VTS 50) that received its input from a function generator (Hewlett Packard HP3314A).

The bellows input signal for all the low speed wake forced cases was set at a frequency of 6 Hz; the same forcing frequency used by MacKinnon & Koochesfahani (1993). The higher speed wake was forced at a frequency of 12 Hz. In each case, the input waveform was symmetric and sinusoidal. The forcing amplitude was varied from case to case. The low speed wake was forced with amplitudes corresponding to velocity perturbations of about 2%, 5%, and 9% RMS of the free stream velocity. These values were found from previous LDV data (MacKinnon & Koochesfahani, 1993). A linear variable differential transformer (LVDT) and a linear velocity transformer (LVT) were available to monitor the bellows' position and velocity.

2.3 Diagnostics

The principle diagnostic tool used in this study was chemically reacting laser induced fluorescence. As noted in the introduction, the chemically reacting mode of LIF does not suffer from the resolution problems present in the nonreacting LIF technique.

Chemically reacting LIF is an extension of the nonreacting LIF technique described in §1.3.

Reacting LIF uses a diffusion-limited, acid-base reaction of the type A + B → P between the two free streams. One free stream fluid is premixed with an acid, in this study sulfuric acid (H_2SO_4), and the other stream is premixed with a base: sodium hydroxide (NaOH). A fluorescent dye is also premixed with the acid. The dye used for this study was disodium fluorescein. This dye exhibits strong greenish fluorescence when excited by an argon-ion laser, but only if it is in an alkaline environment (see Appendix A). Because of this, initially the fluorescence is 'turned off' with the dye in the acidic stream. When the two streams mix, the acid-base reaction is initiated and the pH increases with a corresponding sharp and rapid increase in the fluorescent intensity. Using this technique the dye becomes a marker for chemical product. Figure 6 illustrates product concentration C_P versus base volume fraction ξ_B. The fluorescence behaves in a similar fashion leading to the relation

$$\frac{C_P}{(C_P)_{\max}} = \frac{I_f}{(I_f)_{\max}} \tag{2.1}$$

Equation 2.1 is the basis for all product calculations. The fact that the product concentration is proportional to fluorescence is the fundamental premise used in chemically reacting LIF. The presence of fluorescence indicates product generation and, thus, molecular mixing. Because fluorescence is only observed when mixing has occurred there is no overprediction of mixing from time-averaged data—which is the primary limitation of the nonreacting LIF technique. These concepts are discussed more thoroughly in Appendix A.

For this study fluorescein dye was mixed with the acid stream at a concentration of approximately 2×10^{-7} M (moles/L). Koochesfahani (1984) measured the absorption coefficient α of fluorescein dye to be 0.157 cm^{-1} for a dye concentration $C_d = 1 \times 10^{-5}$ M. The absorption coefficient scales with the dye concentration as $\alpha = \varepsilon_0 C_d$ where ε_0 is the dye molar absorption coefficient. The dye concentration used in this study is a factor of 50 more dilute than Koochesfahani's. Thus, an absorption coefficient $\alpha = 3.14 \times 10^{-3}$ cm^{-1} is expected. Attenuation of the fluorescent intensity at a distance y is given by $I = I_0 e^{-\alpha y}$. In the worst case—the entire test section filled with fluorescent dye—the difference in fluorescent intensity would be about 1.2% between the top and bottom of the test section. Based on these calculations, attenuation was considered negligible.

Effort was also taken to ensure that the two fluid streams had equal density. Addition of acid and base to the two fluid streams could sufficiently change the density to the point where buoyancy effects could no longer be neglected. Buoyancy effects can be evaluated using the Richardson number, Ri, defined as

$$Ri = \frac{\Delta \rho g \delta}{\bar{\rho} U_o^2} \tag{2.2}$$

where $\Delta\rho$ is the density difference between the two free streams, g is the acceleration due to gravity, δ is a representative wake dimension, and $\bar{\rho} = (\rho_1 + \rho_2)/2$ is the mean fluid density. In this study, sodium sulfate (Na_2SO_4) was added to the stream with the density deficit whenever a sufficient density difference was measured. In each experiment the densities of the two streams were matched to within a specific gravity of 0.0005. Therefore, in the worst case—the wake filling the entire test section height—the largest possible Ri is 0.02, based on $\delta = 4$ cm and $U_o = 10$ cm/s. Koop & Browand (1979) found buoyancy effects could be neglected for Ri < 0.05 based on the vorticity thickness of a shear layer at x = 1 cm.

A Lexel model Excel 3000 argon-ion laser operating in light mode (i.e., constant power) was used as the light source. The power requirements varied from experiment to experiment, but generally values of 3-3.5 W were necessary. The optical setup is illustrated in Figure 7. As shown, the beam was passed through a converging lens, then through a cylindrical lens to produce a laser sheet. This configuration produced a sheet that was about 0.5 mm thick.

The streamwise imaging arrangement is shown in Figure 8a. One camera was used to image the test section and the titration reference chamber simultaneously. For these experiments a Sony XC-77RR CCD camera was used. The camera has a resolution of 480 (vertical) × 512 (horizontal) pixels, and was operated with an exposure time of 1 ms. Either Nikkor 50 mm f/1.2 or 58 mm f/1.2 lenses were mounted on the camera with an orange filter (number 15) to eliminate scattered laser light. Standard video framing rate (30 frames/s or 60 fields/s) was digitized to 8 bits and recorded onto hard disk in real time by an image acquisition system (Recognition Concepts, Inc. TRAPIX-5500). For each individual case, a total of 512 frames (1024 fields) were captured requiring 128 MB of disk space. This corresponds to the passage of about 100 structures for the low-speed wake, and 200 structures for the higher speed wake.

Figure 8b illustrates the arrangement used for spanwise imaging. As a result of the facility geometry, an additional camera (not shown in Figure 8b) was needed to image the titration reference chamber. The Sony XC-77RR was used to image the test section. The same settings and lenses were used as those for streamwise imaging (except the x = 24 cm cases, where a 35 mm f/1.7 lens was used). An NEC TI-24A CCD camera was used to photograph the titration reference chamber. The titration chamber and test section were not imaged simultaneously in spanwise experiments because of acquisition limitations. Instead, the titration reference chamber was imaged between experimental runs.

Similar spatial resolutions for both streamwise and spanwise imaging were obtained. The test section height of 4 cm was imaged onto about 250 vertical pixels. Thus, the entire test section span of 8 cm could be imaged onto 500 pixels. The corresponding resolution was 160 × 160 μm. For streamwise imaging only 8 cm of the test section streamwise extent could be imaged at one time. Therefore, three different camera/laser sheet positions were required to cover the x range of interest (x ≈ 5-24 cm).

2.4 Data Reduction

The LIF technique relies on the fact that the ratio of the product concentration C_P at any location to its value at fluorescence turn on $(C_P)_{max}$ is the same as the ratio of the fluorescent intensity I_f at that location to its maximum value $(I_f)_{max}$ (Equation 2.1). Because of this, it is imperative that any nonuniformities in either the laser sheet or the camera (i.e., nonuniform pixel response or black level 'offset') be removed. This was accomplished by first adding each camera's offset to all nonzero intensities (see Appendix B) and then dividing all images by a uniform dye concentration reference image. The reference image was generated at the end of each experiment by running the facility in closed-loop mode until a condition of uniform dye concentration resulted throughout the test section. In practice, this was accomplished by letting the facility run continuously for approximately one hour. For the reference images, the titration reference chamber was emptied and refilled with the uniform dye concentration fluid. This was acheived, of course, without altering the positions of the cameras, laser sheet, test section, or reference chamber.

Each frame in an image sequence was then corrected pixel-by-pixel using the formula

$$I_{corr} = k\frac{I}{I_{ref}} \tag{2.3}$$

where I_{corr} is the corrected pixel intensity, k is a scaling factor (usually selected to produce peak intensity values close to the original values), I is the original pixel intensity, and I_{ref} is the fluorescent intensity of the same pixel from the reference image. Intensities in the titration reference chamber were corrected in the same manner.

The corrected intensities could then be used to calculate the normalized product concentration C_P^*, defined as

$$C_P^*(x,y,z,t) = \frac{C_P}{C_{do}} = \frac{I_f}{I_{fo}} \tag{2.4}$$

where $I_{fo} = (I_f)_{max}/[1 - \xi_S]$ from Figure 6 and Equation 2.1.

The wake's development is best illustrated by evaluating time-averaged quantities. The normalized, time-averaged product concentration at each location in the wake is defined as

$$\overline{C_P^*}(x,y,z) = \frac{1}{T}\int_0^T C_P^*\,dt \tag{2.5}$$

where T is the length of the time record. $\overline{C_P^*}$ can be calculated from experimental image sequences by taking the corrected average intensity (at each pixel) over the entire sequence and dividing by the normalization intensity I_{fo}.

It is customary to quantify the amount of mixing product across the wake using the product thickness δ_P (e.g., Breidenthal, 1981; Roberts, 1985) . Product thickness is defined as

$$\delta_P(x,z) = \int_{-\infty}^{+\infty} \overline{C_P^*}(x,y,z)\,dy \tag{2.6}$$

Integrating δ_P across the test section span results in the total amount of product at a downstream distance x. This quantity is called the product area A_P and is defined as

$$A_P(x) = \int_{-\infty}^{+\infty} \delta_P(x,z)\,dz \tag{2.7}$$

The product thickness has units of length, but it is not a physical distance. The wake, however, does have a physical width. One way to quantify this width would be to measure the thickness of the wake from time exposure or time-averaged images. This method has been used in the past and is called the visual thickness of a wake or shear layer (Roberts, 1985). Another way to quantify the wake width is to define a 1% thickness δ_1. The one percent thickness is the distance between the points where $\overline{C_P^*}$ has fallen to 1% of its maximum value on the top and bottom sides of the wake. Other investigators have found that the 1% thickness and the visual thickness are often nearly equivalent (Koochesfahani, 1984). Figure 9 illustrates the definitions of δ_P and δ_1 graphically.

The wake 1% area A_1 can be evaluated by integrating δ_1 across the test section span

$$A_1(x) = \int_{-\infty}^{+\infty} \delta_1(x,z)\,dz \tag{2.8}$$

Defining a normalized product thickness δ_P/δ_1 is also useful. The normalized product thickness is thus the product *per unit width* of the wake, and can be thought of as a measure of mixing efficiency. Likewise, a normalized product area can be defined as A_P/A_1.

Figure 4, discussed in §1.3, uses a quantity called the mixed-fluid area A_m. In nonreacting LIF the mixed-fluid thickness δ_m is calculated by finding the area under the mixed-fluid pdf, P_m. A_m is then found by integrating δ_m across the test section span. It can also be shown that $\delta_m = \delta_{P1} + \delta_{P2}$ where δ_{P1} and δ_{P2} are the product thicknesses referenced to the upper and lower free streams, respectively (Koochesfahani & MacKinnon, 1991). In the present study, the dye was always carried in the upper stream, thus $\delta_P = \delta_{P1}$. Finding δ_{P2} by flipping the upper and lower streams so that the acid/dye is in the lower stream is possible, but would require each experiment to be performed twice: once with the dye in the upper stream, and once with the dye in the lower stream. If it is assumed that the wake flow is symmetric and, thus, has a unity entrainment ratio—which appears valid at least for highly mixed cases (see MacKinnon & Koochesfahani, 1993)—then $\delta_{P1} = \delta_{P2}$ and $\delta_m = 2\delta_P$ leading to $A_m = 2A_P$.

Chapter 3

RESULTS FOR THE LOW SPEED WAKE

This chapter presents visual and quantitative results for the low speed (U_o = 10 cm/s) wake. This flow was forced at a frequency f = 6 Hz at amplitudes corresponding to approximately 2%, 5%, and 9% RMS of the free stream speed U_o. The unforced wake at these flow conditions was also studied for comparison.

3.1 Streamwise Results

Streamwise data for the low speed wake were obtained for a total of four complete spanwise planes: z = 0.0 cm (also referred to as 'midspan'), z = +0.8 cm, z = -0.8 cm, and z = -2.0 cm. To cover the complete streamwise range of interest, x ≈ 5 - 25 cm, three separate laser sheet positions were required.

3.1.1 Flow Visualization

Figures 10-25 are chemically reacting LIF images of the low speed wake. For each case sample instantaneous images and images averaged over the entire sequence (1024 fields) are shown. The streamwise (x) range of each image is indicated below the images. The transverse range covered in each image is y = -1.8 to 1.8 cm. Note that the images are presented at actual size. Each page illustrates a single forcing condition and flow in each image is from right to left. Colors used in the images are directly related to the normalized product concentration through the colormap shown at the bottom of each Figure.

z = 0.0 cm (midspan)

Figure 10 shows the unforced wake at the test section midspan (z = 0.0 cm). The mixing interface appears as a thin, sinuous line. Weak spanwise vorticity originating from the splitter plate tip (not shown in these images) causes the waviness of the interface. The interface gradually grows in amplitude and starts to crest in the central image (x = 12-19 cm). The highest x locations seem to show a 'bunching' effect—the waves appear compressed in the streamwise direction. This may lead to eventual pairing of the structures farther downstream, similar to the pairing observed in shear layers (e.g., Winant & Browand, 1974). Overall, the unforced wake has a much more random development than the forced cases to be described next. Events such as the 'bunching' evident in the high x image of Figure 10a seem to occur randomly, possibly as a result of some external, unintentional disturbance. Figure 10b, the average image, shows the overall low level of mixing achieved in the unforced case. The wake increases in width moving downstream, but shows very little increase in mixing throughout the streamwise range shown.

Figure 11, images of the wake at midspan with 2% forcing, shows the wake has a more periodic, repeatable structure compared with the unforced case. The gap between x = 11 cm and x = 14.5 cm is an actual gap in the acquired data. The forcing clearly alters the flow leading to a more rapid, organized roll-up of the interface. Another interesting feature is shown in Figure 11b. After initially increasing in width (δ_1), like the unforced case, the 2%

forced case width levels off—and perhaps decreases a little—before increasing again for higher x. The high x (19 cm ≤ x ≤ 25 cm) image of Figure 11b, in particular, shows definite streaks of higher intensity fluid. These streaks are caused by the same features of the structures passing in nearly identical positions throughout the image sequence. Discontinuities do exist between average images acquired for different laser positions (see, for example, the center and left image in Figure 11b). Each image contains data from a different experimental run, therefore the flow and forcing conditions can be slightly different from image to image. The effects of various flow parameters on the development of the wake will be addressed later in this report.

The 5% forcing case is shown in Figure 12. The structures appear more tightly rolled up than the 2% case and a 'dot' of mixed fluid appears in the center of each structure above the wake centerline. This dot is most likely caused by the C_P versus ξ_B behavior of the dye. Product concentrations are at their peak for ξ_B near ξ_S (see Figure 6), so wake regions with a large excess of upper stream fluid appear bright in the flow images. The cores of the vortices shed from the upper surface of the splitter plate are probably this type of wake region.

The roll-up continues as the structures move downstream, and eventually (the high x image of Figure 12a) the structures take on a teardrop shape. Figure 12b shows a pattern similar to that seen in Figure 11b: the width of the wake is fairly constant in the range x ≈ 8-15 cm then begins to increase for x > 15 cm.

Figure 13 shows midspan images of the wake at 9% forcing amplitude. The structures resulting from this highest forcing condition are characterized by a distinct 'mushroom' appearance at low x. In contrast to the lower forcing cases, 9% forcing causes the vortex cores to be centered very close to the wake centerline. Structures resulting from vortices shed from the top surface of the splitter plate are, like the 5% case, characterized by a dot of fluid at the vortex cores. In fact, the structures originating from the top surface of the splitter plate ($-\omega_z$) appear more rolled-up than those originating from the bottom surface ($+\omega_z$). Moving downstream, the vortex structures in Figure 13a grow and begin to exhibit large amount of mixed fluid in their cores. This highly mixed fluid is a direct result of three-dimensionality in the flow. By the time the wake has reached the third image (x = 19 cm) it has grown to fill the entire height of the test section and the original spanwise vortex structure is completely absent. The average images, Figure 13b also show this development. The wake width increases constantly moving downstream. The breakdown to three-dimensionality observed in the center image of Figure 13a translates to the highly mixed condition evident in Figure 13b. $\overline{C_P^*}$ values are fractionally higher in the upper half of the test section in the high x image of Figure 13b, although the entire wake is well-mixed on average.

z = +0.8 cm

Slightly off-center there are some subtle differences. Figure 14 shows the unforced low speed wake at z = +0.8 cm. The instantaneous images, Figure 14a, show a pattern very similar to the midspan images. The average images, Figure 14b, show some differences from the unforced midspan cases (Figure 10b). For one thing, the wake is clearly narrower off midspan. Also the average images in Figure 14b are not as continuous across the three images as the midspan average images were. It has already been mentioned that the unforced cases seem more random than the forced cases, thus the discontinuities across the images may stem partly from the more random nature of the unforced wake. Also, the overall product concentration levels are so low for the unforced wake that small intensity decreases can cause $\overline{C_P^*}$ to be mapped to black in the images.

Figure 15 depicts the 2% forced wake at z = +0.8 cm. Its basic structure is much the same as the midspan case, Figure 11. Once again, the average images show that the wake width remains fairly constant downstream after initially growing for low x. Another feature of Figure 14b is the presence of streamwise nonuniformities. Careful examination of the low x image reveals a herringbone-like pattern. These nonuniformities can be seen in several other time-averaged images, as well. Briefly, the framing rate of the camera is such that the image from the eleventh field will be slightly out of phase with the image from the first field. After some large number of fields, the entire phase of the wake will have been covered and the entire process repeats. If the mixing interfaces are very thin, it is possible that the interfaces may 'miss' columns and these columns will appear black in the average images. The nonuniformities are a direct result of the digitization and are only seen for flows with little mixing, thus should not greatly affect calculated mixing quantities.

At 5% forcing, shown in Figure 16, there are substantial differences from the midspan case.

After developing similarly to the midspan case for low x, the upper ($-\omega_z$) vortex structure stretches and the uppermost band of the interface begins to jut out over the top of the like-signed, downstream vortex. The lower ($+\omega_z$) vortex structures appear to continue downstream largely unchanged. Recall that the midspan wake with 5% forcing exhibited a teardrop shaped structure at high x—this structure is entirely absent from the z = +0.8 cm case. These differences suggest that there is some three-dimensionality in the wake at this downstream distance.

The 9% forcing case at z = +0.8 cm, shown in Figure 17, is also slightly different from the midspan case. The characteristic mushroom shape develops initially, but three-dimensionality is observed at earlier x than the midspan case. Also, the wake growth rate seems slightly lower. The wake does not fill the entire test section until well into the far left instantaneous image ($x \approx 22$ cm). Also, even though the wake is well mixed at high x, the streamwise periodicity is still preserved. Although three-dimensionality appears to be responsible for the increase in mixing, three-dimensionality does not seem to destroy the primary spanwise structure of the wake. It is likely, judging from the high x image of Figure 17a, that the streamwise periodic structure is destroyed when the spanwise rollers move into the boundary layers at the top and bottom of the test section. The average images (Figure 17b) show development much like the midspan case: constant growth and an increase in mixing until the wake fills the entire test section.

z = -0.8 cm

In general, the structure of the wake at z = -0.8 (Figures 18-21) is very similar to the structure at z = +0.8 cm. This implies that the wake is symmetric about the z = 0 cm plane. One notable exception, however, is Figure 20. At low x, the structure of the wake forced at 5% is similar whether the plane of the laser sheet is at z = 0.0 cm (Figure 12), z = +0.8 cm (Figure 16), or z = -0.8 cm (Figure 20). The high x images, however, are different. There are at least two possible explanations for this. Either the wake is slightly asymmetric or the differences may be the result of case to case flow variations and not the result of wake asymmetry at all.

z = -2.0 cm

The structure of the wake midway between the midspan and the wall of the test section is substantially different from the structure near the midspan. Many of the differences can be attributed to the presence of three-dimensionality at smaller x locations. The unforced case, shown in Figure 22, develops in its usual manner: initially a sinuous line of gradually increasing amplitude moving downstream. Well downstream, however, an interesting pattern is observed. Streams of fluorescent product appear to break off the main interface and protrude well above and below the wake centerline. Although it is possible that these structures are, in fact, not connected to the rest of the interface, it is more probable that three-dimensionality has moved a portion of the interface out of the plane of the laser sheet. The existence of these structures is also seen in the high x average image of Figure 22b. Near the centerline there is a narrow band of mixed fluid, then bands above and below the centerline that are separated by regions of largely unmixed fluid. There is a large discontinuity between the mid x and high x images in Figure 22b, but the overall product concentration levels are so low the discontinuity probably does not significantly affect product thickness results.

The structure of the wake forced at 2% amplitude, Figure 23, is also similar to the midspan case for low x. Downstream at $x > 18$ cm, though, a slightly different structure arises where the spanwise vortices are 'stacked.' Structures of opposing vorticity are clearly above and below the wake centerline with a region of more highly mixed fluid between them. This suggests three-dimensionality in the wake downstream of $x = 18$ cm. Despite the differences seen in the instantaneous images, the average images are similar to the midspan cases, although there is more product downstream.

The wake at 5% forcing amplitude, Figure 24, shows three-dimensionality for $x > 12$ cm. The highly mixed, three-dimensional fluid is initially confined to the vortex cores, but gradually encompasses most of the wake as it moves downstream. The 'stacked' vortex pattern observed in the 2% case is also seen here. The average images of Figure 24b show that the wake is much more well-mixed, but narrower, than the corresponding midspan case.

Figure 25, 9% forcing amplitude, shows perhaps the most interesting wake development. The instantaneous images of Figure 25a show the wake becomes three-dimensional very early ($x \approx 7$ cm) leading to a fairly well-mixed condition by $x = 11$ cm. Moving downstream, though, the wake narrows slightly and there is a large decrease in product. This development is especially striking when viewing the image sequence in real time: the wake appears to 'unmix' as it moves downstream. Actually, what is really occurring is the region of strong mixing is moving out of the laser sheet plane with increasing downstream distance. Spanwise images will show this phenomenon more clearly.

3.1.2 Calculated Quantities

Figures 26-29 present the results calculated from the streamwise average images in Figures 10-25. δ_P and δ_l both consider only the transverse region y = -1.8 to +1.8 cm, thus the maximum value of δ_l is 3.6 cm. Each Figure contains data from several experimental runs that are marked identically for clarity. Different symbols indicate different forcing conditions only.

z = 0.0 cm (midspan)

Figure 26 presents the calculated data for the low speed wake at midspan. The development of δ_l for all forcing conditions is plotted in Figure 26a. Many of the features in the flow images are also seen in this plot. The unforced wake is very narrow for low x and its width increases continuously moving downstream. The wakes forced at 2% and 5% show initial growth for low x, then each enters a region of virtually fixed δ_l before resuming growth at higher x. The wake forced at 9%, on the other hand, shows no reduction in growth rate. The wake forced at 9% increases in width until it has filled the entire test section (δ_l = 3.6 cm).

Figure 26b depicts the development of the product thickness δ_P for each forcing condition at z = 0.0 cm. The clear pattern emerging from this graph is that increasing the forcing amplitude drastically increases mixing, especially at high x. At x = 24 cm, the wake forced at 9% has a product thickness a factor of 40 higher than the unforced wake at the same location. Normalized product thickness curves are shown in Figure 26c. Increases in forcing amplitude are accompanied by large increases in the amount of normalized product. The 9% forcing case approaches a value of $\delta_P/\delta_1 \approx 0.42$, close to the value of 0.5 for perfect 1:1 mixing.

Figures 26b and 26c, in particular, show significant data spread for the 9% forcing condition. Keep in mind that each individual forcing condition shows data from at least three experiments (low, mid, and high laser sheet locations). In some cases there is also a redundancy in data for a certain laser sheet position. The middle laser sheet location (x ≈ 12-20 cm), for example, shows data from three different 9% forcing cases. Each individual case is easy to recognize on the plots. Because each plot shows data from many experiments, it is not surprising that discontinuities and data spread are common in Figures 26-29. Slight variations in the forcing amplitude are the most probable reason for discrepancies between data sets and will be discussed further in §3.1.3.

z = +0.8 cm

Figure 27a illustrates δ_1 versus x for each forcing amplitude at z = +0.8 cm. δ_1 values are similar between the midspan and z = +0.8 cm cases. The product thickness (Figure 27b) is also similar except for the 9% forcing case. At 9% forcing δ_P is higher than at the midspan for low x, but its ultimate level is considerably lower. The reduction in δ_P at high x also results in a decrease in normalized product thickness (see Figure 27c).

z = -0.8 cm

Results for z = -0.8 cm are shown in Figure 28. The wake width δ_l is very similar to both the midspan and z = +0.8 cm cases. The product thickness increases very quickly for 9% forcing and reaches an ultimate value of about δ_P = 1.5 cm at x = 24 cm. This is close to the value found at midspan. The normalized product thickness reaches an ultimate value of about 0.41 at x = 24 cm, again close to the midspan value.

z = -2.0 cm

As was the case in the flow images, the calculated quantities at z = -2.0 cm are quite different from their midspan counterparts. Figure 29a shows the development of δ_l versus x. Both the 2% and 5% forced cases show development similar to the midspan cases. The 9% forcing case, though, is substantially different. For 9% forcing, δ_l is close to its value at the midspan for x = 5 cm. However, after initially growing in width more quickly than the midspan case, the width at z = -2.0 cm reaches a maximum value at x ≈ 12 cm, then begins to decrease for higher x. Another feature evident in Figure 29a is the large jump in δ_l for the middle laser sheet location of the unforced wake. This discontinuity is also evident in the corresponding flow image, Figure 22b.

The product thickness for the unforced case, shown in Figure 29b, is much more continuous than δ_1. The overall levels of mixing are so low that the increased width apparently does not greatly affect δ_P. The downstream evolution of δ_P is quite striking for the 9% amplitude case. δ_P rises very quickly for 9% forcing, but reaches a maximum at x = 10.5 cm, then begins to fall. The maximum value of the product thickness is $\delta_P = 0.62$ cm, only 40% of the maximum attained at the midspan. In fact, both the 2% and 5% forcing cases eventually show more product than the 9% forcing case at high x. Normalized product thickness, Figure 29c, shows similar trends. The cases with lower forcing amplitude have higher δ_P/δ_1 than the 9% amplitude case for high x due to their increased amount of product.

3.1.3 Factors Leading to Variation in Streamwise Data

As noted above, the data in Figures 26-29 often do not collapse onto a single curve. These figures all contain data measured from several different experimental runs. Although the experiments are nominally identical, there are several factors that may vary slightly between runs. Flow properties that may vary include the free stream velocities of the two streams, the forcing frequency, and the forcing amplitude. This section discusses the extent each of these factors can affect the calculated wake data.

Error in Forcing Amplitude

Figures 26b-29b show that the product thickness of the wake is strongly dependent on the forcing amplitude. Because of this, a small error in setting the forcing amplitude can translate into significant variations in the measured δ_P. Based on the method used for setting the forcing amplitude (monitoring the bellows velocity trace with an oscilloscope), a 5% error in forcing amplitude is considered reasonable.

Since data are available for the wake at several forcing frequencies, it is possible to estimate the error introduced by forcing the wake at amplitudes slightly different from a nominal value. The first step is to plot δ_P versus forcing amplitude for several x locations. One example is provided in Figure 30. The data points in Figure 30 are the mean values of the δ_P data at z = 0.0 cm (Figure 26). The solid lines connecting the points in Figure 30 were generated using a third order curve fit to the data points. The slope of these lines, shown in Figure 31, shows the sensitivity of δ_P to variation in forcing amplitude. The x = 19 cm curve, for example, passes through $\Delta\delta_P/\Delta amp = 0.44$ at 8.5% forcing amplitude. Thus, a ±5% error in setting the forcing amplitude would produce an error in δ_P of $0.44 \times (8.5 \times 0.05) = \pm 0.187$ cm. This corresponds to a 16% uncertainty in δ_P at this location.

Figures 32-35 are plots of mean δ_P (solid lines) versus x showing a ±5% error envelope in the forcing amplitude (dashed lines) for the cases forced at 5% and 9% amplitude. The error envelope was determined using data similar to Figure 31. Experimental data sets are shown by various symbols. The Figures show that a ±5% amplitude error band can account for most of the variation among the various data sets at the same nominal conditions.

Error in Free Stream Speed and Frequency

The downstream evolution of the product thickness may be expected to scale in terms of a nondimensional streamwise parameter x* defined as

$$x^* = \frac{x}{\lambda} = \frac{xf}{U_o} \tag{3.1}$$

where λ is the forcing wavelength of the wake. With this scaling, changes in forcing frequency and free stream velocity result in a perceived expansion or compression of x*. The total uncertainty contributed by the free stream velocity and the forcing frequency can be lumped into a single parameter ϵ. Thus, x* can be rewritten as $x^* = xf(1 + \epsilon)/U_o$ to account for variation from the nominal values of frequency and free stream velocity.

The first step in rescaling the data using the ϵ correction factor is to pick one data set as a 'baseline.' All other data sets for the same forcing amplitude and z locations are then scaled using different values of ϵ until they fit the baseline data set optimally. Data can be forced to fit very well if no constraints are put on ϵ. From a practical point of view, though, the combined speed/frequency error is not expected to be large. The free stream velocities can be monitored accurately with the flow meters and the forcing frequency is dialed into a function generator. Based on this, a total error of less than 5% is expected (in contrast, the effects of much larger variations in the free stream speed are discussed in Appendix C). Therefore, a more reasonable method of rescaling is to allow ϵ to fall within a certain, constrained, range. Thus, for a ±5% total error the difference between the maximum and minimum values of ϵ should differ by no more than 0.10. Figure 36 shows a representative example of ϵ rescaling. Figure 36a shows δ_P versus x* for data with no rescaling. Figure

36b shows the same data rescaled such that $\Delta\epsilon \leq 0.10$, and Figure 36c shows the data rescaled without any constraints on ϵ. The data can be forced to fit very well if no constraints are placed on ϵ (see Figure 36c), but results are nearly as good if ϵ is constrained to ±5% (Figure 106b).

In conclusion, some of the variation between data sets can be accounted for by uncertainty in the forcing frequency and the free stream velocity. However, both of these parameters can be set quite accurately during an experiment. Thus, these parameters may account for a little variation between data sets, but the majority of the variation can be attributed to error in setting the forcing amplitude.

3.2 Spanwise Results

Streamwise imaging allows observation of the downstream evolution of the wake both visually and quantitatively. Unfortunately, only a thin slice of the wake span is seen at one time. Spanwise imaging, on the other hand, allows the entire cross-section of the wake to be viewed in one experiment. Spanwise viewing allows several vital questions to be answered. For example, what fraction of the test section is occupied by mixed fluid for each forcing condition?

Because of this, spanwise data for the low speed wake were acquired at five different x locations: x = 4, 8, 12, 16, and 24 cm. One difficulty with this imaging setup is light from the laser sheet must pass through much more fluid than for streamwise imaging (typically about 30 cm for spanwise imaging compared with 4 cm for streamwise imaging) before reaching the camera lens. The chemical reaction between the two streams results in index of refraction variations, thus possible optical problems, in the test section. For this reason, data from streamwise imaging is considered more accurate—especially at low x. However, spanwise imaging is the only method that allows the entire test section to be imaged simultaneously, and for this reason spanwise data were collected. Comparisons of streamwise and spanwise data will be presented later.

3.2.1 Flow Visualization

Figures 37-56 are chemically reacting LIF images of the low speed wake. Each Figure contains a total of ten images corresponding to one complete forcing cycle of the wake. The images are separated in time by $\Delta t = 1/60$ s and the sequence proceeds down the left column, then down the right column. Thus, the first image in the sequence is in the upper left position and the last image is in the lower right. The range in each image is approximately $z = -3.9$ to $+3.9$ cm and $y = -1.9$ to $+1.9$ cm. The greyscale mapping varies and is indicated by the colorbar shown in each Figure. The lowest value of C_P^* that has been mapped to white is noted in the caption of each Figure.

x = 4 cm

The unforced wake at x = 4 cm is depicted in Figure 37. Like the streamwise images of the unforced wake at low x, the spanwise views show a single, thin mixing interface between the two fluid streams. The interface is nearly two dimensional, although there appears to be some slight distortion near the test section side walls. The intensity levels are also very low, a feature common to many of the spanwise cases at low x.

The 2% forcing case is shown in Figure 38. Once again, the intensity levels are quite low and it is difficult to discern some of the features of the flow. However, a single interface is evident in each image. Unlike the unforced case, the interface moves considerably in the y direction from image to image. Also, the presence of three-dimensionality is clearly seen near the edges of the images. Three-dimensionality is even more well defined in Figure 39, the 5% forcing case. There appear to be several streamwise vortices near both sides of the images. The middle part of the test section is two-dimensional and exhibits a more convoluted interface than the unforced and 2% forcing cases. Figure 40, 9% forcing, is somewhat similar—streamwise vortices near the sidewalls connected by a nearly two-dimensional central region. The intensity values in the regions of streamwise vorticity are considerably higher than in the two-dimensional central region.

x = 8 cm

The unforced wake at x = 8 cm, Figure 41, shows the three-dimensionality first observed at x = 4 cm more clearly. Like at x = 4 cm, there is a single, nearly two-dimensional interface over most of the test section span. Near the walls, though, there is definite vertical displacement of the interface indicating streamwise vorticity.

At 2% forcing amplitude, Figure 42, there is considerable change compared to the same case at x = 4 cm. Although the intensities are still low, there is much more activity in the center of the test section, also the three-dimensionality near the side walls is more evident. The major difference in Figure 43, 5% forcing, is the overall intensities are substantially higher than they were at x = 4 cm indicating more chemical product at x = 8 cm than upstream. In addition, the overall width of the wake has increased.

9% forcing, shown in Figure 44, is the most dramatic illustration of the streamwise vortex structures yet seen. Two areas of high mixing can be observed in each image, while the central portion of the test section continues to show the passage of the tightly rolled-up spanwise structures. Careful examination of the central portion of each image shows the passage of the braid regions that connect the core regions followed approximately two or three images later by the passage of the core regions themselves.

x = 12 cm

Figure 45, the unforced wake at x = 12 cm, illustrates the behavior of the wake with increasing downstream distance. The wake is no longer two-dimensional: there is considerable variation across the test section span. The unforced wake still shows only a single mixing interface, though. The 2% forced wake shown in Figure 46 is a more developed version of the same case at x = 8 cm, as is the case for 5% forcing, Figure 47. Although the central portions of the images in Figures 46 and 47 are still primarily two-dimensional, there is some spanwise undulation of the interfaces beginning to appear.

A large portion of the wake forced at 9%, shown in Figure 48, is dominated by streamwise structures. Tightly rolled-up spanwise mixing interfaces are still evident (e.g., the fourth image in the right-hand column), but at x = 12 cm three-dimensionality is starting to encroach all the way to the middle of the test section. Despite the presence of the well-mixed streamwise vortices across most of the structure, there are still areas in the center of the test section with little or no mixing evident.

x = 16 cm

The structure of the unforced wake at x = 16 cm, Figure 49, is quite similar to the structure at x = 12 cm. The interface moves more in the transverse direction from image to image, however, and one image (bottom right) shows a partial second interface below the primary interface. This shows that the wake is starting to crest, at least sporadically, at this x location. Streamwise vorticity near the side walls tends to distort the mixing interface into a 'horseshoe' shape. The 2% and 5% forcing cases, Figures 50 and 51, are similar to the same cases at x = 12 cm. Three-dimensionality is still primarily confined to near the two side walls, but there is some indication of increased waviness to the spanwise interfaces in the center of the test section. The wake width is close to its value at x = 12 cm for these two forcing cases. This agrees well with the observations from streamwise imaging (Figures 11-12).

The 9% forcing amplitude case at x = 16 cm is shown in Figure 52. Streamwise structures completely dominate the wake structure. The last vestiges of the spanwise vortex structures can be seen as a very faint, thin interface at either the top or bottom of the images, depending on the location in the forcing cycle. Although the entire center of the test section shows three-dimensionality at certain times, the streamwise structures originating from each side wall can still be discerned—there is still a small area at the very center of the test section that can contain unmixed fluid. Also, the regions near the test section side walls have very little mixing.

x = 24 cm

The structure of the unforced wake at x = 24 cm, Figure 53, exhibits up to three mixing interfaces in the center of the test section. This indicates that at x = 24 cm, the unforced wake crests fairly consistently. The 2% and 5% forcing cases are presented in Figures 54 and 55. Three-dimensionality, especially in the 5% case, appears to be gradually moving toward the center of the test section.

Figure 56 depicts the 9% forcing amplitude case at x = 24 cm. At this point, all of the mixed fluid occupies the central portion of the test section, and fills the test section's entire vertical extent. Unlike at x = 16 cm, the streamwise structures from each side of the test section are no longer distinguishable. There are, however, large streamwise vortex structures on each side of the mixed region above the test section centerline (see the last three images). It is interesting that although the fluid in the center of the test section is very well mixed, the regions near the test section side walls are virtually devoid of mixed fluid.

Average Images

Images averaged over the entire sequence are presented for each spanwise case in Figures 57-58. The images are pseudocolored using the colormap at the bottom of each Figure. These images are, in fact, plots of $\overline{C_P^*}(y,z)$, thus the Figures show the downstream evolution of the mean, normalized product concentration for each forcing amplitude. Traditional line plots showing a subset of the data from Figures 57-58 are included in Appendix E.

Figure 57 shows $\overline{C_P^*}(y,z)$ for the unforced wake (left column) and the wake forced at 2% (right column). $\overline{C_P^*}(y,z)$ for the wake forced at 5% (left column) and 9% (right column) are presented in Figure 58. The general trends for each case are an increase in width and mixing as the wake moves downstream. The regions of strongest mixing, especially in the 5% and 9% forcing cases, move toward the center of the test section with increasing x.

3.2.2 Calculated Quantities

With the data from Figures 57-58, it is now possible to study the spanwise variation of several wake quantities. A subset of the column data from the images in Figures 57-58 have been used to generate the plots in Figures 59-63. These Figures show $\delta_1(z)$, $\delta_P(z)$, and $\delta_P/\delta_1(z)$ for the five x locations studied. Like the streamwise cases, only the region y = -1.8 to +1.8 cm was used for the calculations, thus the maximum possible value for δ_1 is 3.6 cm. Note: a common range has been used for δ_1 in Figures 59-63 (0-4 cm). The ranges for δ_P and δ_P/δ_1 vary between Figures to enhance the detail.

x = 4 cm

The wake 1% thickness across the test section span for each forcing condition is shown in Figure 59a. At this low x location the wake tends to have a uniform width across the central portion of the test section with marked variation near the side walls. This pattern occurs regardless of the forcing condition. The 5% and 9% forced cases exhibit nearly identical thicknesses, with the 2% case showing slightly lower δ_1 and the unforced case showing a much lower value of δ_1. The product thickness is shown in Figure 59b. The unforced wake and wake subjected to 2% forcing amplitude show nearly identical (low) δ_P. The 5% forcing case is similar in the middle portion of the test section, but exhibits a marked increase in product thickness near the side walls. The 9% forcing case also shows this increase near the side walls, but the amount of product is also significantly larger in the center of the test section compared to the other cases. Note that the regions of increased product correspond to the areas occupied by streamwise vortices (see Figures 39-40). The normalized product thickness across the span for all forcing cases is shown in Figure 59c. The unforced wake has the highest values of δ_P/δ_1 in the central portion of the test section as a result of its very low values of δ_1. Overall values of δ_P/δ_1 are very low for all forcing conditions, though.

x = 8 cm

Data from the x = 8 cm laser sheet location are presented in Figure 60. One characteristic of these data, as well as data farther downstream, is the pronounced symmetry between the two halves of the test section. Also, both the wake width δ_1 and product thickness δ_P drop to zero near the test section walls. The areas with the largest amount of mixing are always away from the side walls at this location and farther downstream.

Figure 60a shows that δ_1 is similar in the middle of the test section for the three forced cases with the unforced case showing a thickness roughly a factor of two lower. Although δ_1 is still fairly uniform in the central portion of the test section for each case, there is some evidence of the beginning of spanwise variation. Figure 60b shows the product thickness across the test section span for each case. δ_P tends to be constant in the center of the test section for all cases, however the 5% and 9% forcing cases both show well defined δ_P peaks on either side of the test section centerline. In both cases the peaks have moved away from the test section side walls, echoing the behavior of the streamwise vortices in Figures 43-44. Figure 60c shows the variation in δ_P/δ_1 across the test section for each forcing condition. Overall levels of normalized product have increased for all forced cases compared with the x = 4 cm data.

x = 12 cm

The salient characteristic in Figure 61a, δ_1 versus z at x = 12 cm, is the increased width of the wake forced at 9% compared with the 2% and 5% cases. In fact, the 2% and 5% forcing cases have a width very similar to that observed at x = 8 cm. The unforced wake is still considerably narrower, but it has doubled in width since x = 8 cm. Product thickness, Figure 61b, has increased for all the forced cases. Also, all three forced cases show clear δ_P maxima on each side of the test section centerline. The product thickness peaks for the 9% forcing case have moved about 5 mm inward from their positions at x = 8 cm and, as a consequence, there is no longer a region of nearly constant δ_P in the center part of the test section. The maximum normalized product thickness, Figure 61c, has increased to about 0.26 for the 9% forcing case, compared to 0.19 at x = 8 cm. Similar increases are also seen for the other forcing cases.

x = 16 cm

δ_1 for the 2% and 5% forcing cases at x = 16 cm, shown in Figure 62a, continue to remain at a virtually fixed level in the center of the test section. The unforced case is still growing, and by x = 16 cm it is nearly as thick as the 2% and 5% forcing cases. The wake forced at 9% amplitude has a width of just above 3.0 cm in the middle of the test section, but its width falls off quite sharply at about z = ± 1.0 cm. The product thickness, too, is concentrated near the center of the test section (see Figure 62b) for 9% forcing. At x = 16 cm, the δ_P maxima have moved to locations of z ≈ ±0.6 cm. A very narrow region of reduced product thickness is evident at the test section center, which agrees well with the images in Figure 52. The other forced conditions and the unforced condition show profiles similar to those at lower x locations, but with increased overall values. The normalized product thicknesses for all cases are plotted in Figure 62c. An increase in normalized product is evident for each case compared with locations further upstream. For example, the maximum δ_P/δ_1 for 9% forcing at x = 16 cm is about 0.32, 23% higher than at x = 12 cm.

x = 24 cm

The wake 1% thickness across the test section at a position 24 cm downstream of the splitter plate tip is shown in Figure 63a. δ_1 for the unforced wake has finally reached a value very close to the wake forced at 2% in the center portion of the test section. The width of the 2% forcing case is still about the same as it was at x = 12 cm, but there are regions of increased width at z ≈ ±3.0 cm. The 5% forcing case, on the other hand, is clearly wider than it was upstream. 9% amplitude forcing results in the wake filling the entire vertical extent of the test section over the central 2.5 cm of the test section span. The wake thickness drops sharply outside this region. However, there are shoulders with a width $\delta_1 \approx 1.1$ cm located about 2.3-3.0 cm from midspan. These shoulders show up well in the mean concentration field image (Figure 58). The 'double hump' profile of the product thickness at lower x is absent from the 9% forcing case at x = 24 cm (Figure 63b). The product thickness no longer decreases at midspan, resulting in a profile with a single peak. The maximum δ_P for the 9% forcing case is nearly 1.5 cm, which compares well with streamwise results. δ_P peaks on either side of midspan are still evident for the lower forcing amplitudes. The product thickness has increased moving downstream, though. Peak δ_P for the 5% amplitude case is 0.61 cm at x = 24 cm compared with 0.39 cm at x = 16 cm. Midspan values of δ_P/δ_1 (Figure 63c) are about 0.09, 0.15, and 0.38 for the 2%, 5%, and 9% forcing cases, respectively. These are all significantly higher than at x = 16 cm, where the values were 0.04, 0.10, and 0.17.

As noted above, the peak values of δ_P for the forced wake move away from the side walls and into the central portion of the test section for increasing x. The regions of the wake with the most product are also strongly three-dimensional. Examination of Figures 59-63 reveals that the regions of three-dimensionality move away from the side walls quickly for low x, but begin to slow moving downstream. In addition, the regions of three-dimensionality in the higher forcing amplitude cases convect away from the side walls faster than the regions in the lower amplitude cases. Appendix F discusses this phenomenon in greater detail.

Span-Averaged and Integrated data

Figures 59-63 show that δ_1 and δ_P are often strongly dependent on z. Stating a single value of δ_P at the midspan, for example, does very little to explain the overall behavior of the wake. There are several ways that the large body of data in Figures 59-63 can be pared down to elicit a much smaller body of data that quantifies the extent and amount of mixing across the entire cross-section of the wake. For example, integrating δ_P and δ_1 across the test section span results in the product area A_P and the 1% area A_1 (see Equations 2.7 and 2.8). A_P is a measure of the total amount of chemical product in the wake at a downstream distance x. A_1 is a measure of the total area occupied by mixed fluid at x. From these two quantities a normalized product area can be defined as A_P/A_1. This is a measure of the chemical product per unit area of the wake and can be interpreted as the mixing efficiency. Similarly, A_P/A represents the product area as a fraction of the total test section area.

All of the above quantities represent some type of area. Two useful quantities with units of length are the span-averaged 1% thickness $\langle\delta_1\rangle$ and the span-averaged product thickness $\langle\delta_P\rangle$, which are found by dividing A_l and A_P, by the width of the test section.†

Tables 1-4 summarize these data for each forcing amplitude and the unforced wake. These Tables represent the fulfillment of one of the primary goals of this investigation: to quantify the downstream evolution of the mixing field under different forcing conditions. Several interesting observations can be made from the data in Tables 1-4. For example, there is 10.4 times more normalized product at x = 24 cm for the wake forced at 9% amplitude than for the unforced wake. The data for the normalized product area A_P/A_l at each forcing condition is plotted in Figure 64. The efficiency of the mixing increases with downstream distance and forcing amplitude, except for the unforced flow which shows its highest A_P/A_l at x = 4 cm due to a very small value of A_l (1.53 cm^2). The maximum value of normalized product area is A_P/A_l = 0.250 for the 9% forced wake at x = 24 cm (see Table 4).

3.3 Comparison of Streamwise and Spanwise Data

A caveat was stated at the beginning of §3.2 stating streamwise imaging is thought to be slightly more accurate than spanwise imaging. At this point, data are available from both of these imaging configurations. Therefore, these data can be compared to determine the extent of any differences observed.

† The quantities δ_l and δ_P were calculated using the region y = -1.8 to +1.8 cm and z = -3.6 cm to +3.6 cm, thus all span-averaged and integrated quantities use these limits. The "width of the test section" is therefore 7.2 cm, not the physical value of 8.0 cm. Likewise, the test section area used for calculations was A = 25.92 cm^2 (3.6 cm × 7.2 cm) not the physical value of 32 cm^2 (4 cm × 8 cm).

Table 1. Spanwise data for the unforced, low speed wake.

x (cm)	A_1 (cm^2)	A_P (cm^2)	$\langle\delta_1\rangle$ (cm)	$\langle\delta_P\rangle$ (cm)	A_P/A	A_P/A_1
4	1.53	0.060	0.213	0.008	0.002	0.039
8	4.30	0.058	0.597	0.008	0.002	0.013
12	8.67	0.110	1.204	0.015	0.004	0.013
16	11.04	0.153	1.533	0.021	0.006	0.014
24	10.92	0.266	1.517	0.037	0.010	0.024

Table 2. Spanwise data for the low speed wake forced at 2%.

x (cm)	A_1 (cm^2)	A_P (cm^2)	$\langle\delta_1\rangle$ (cm)	$\langle\delta_P\rangle$ (cm)	A_P/A	A_P/A_1
4	7.77	0.058	1.079	0.008	0.002	0.007
8	11.24	0.077	1.561	0.011	0.003	0.007
12	13.29	0.485	1.846	0.067	0.019	0.036
16	13.88	0.830	1.928	0.115	0.032	0.060
24	14.50	1.817	2.014	0.252	0.070	0.125

Table 3. Spanwise data for the low speed wake forced at 5%.

x (cm)	A_1 (cm^2)	A_P (cm^2)	$\langle\delta_1\rangle$ (cm)	$\langle\delta_P\rangle$ (cm)	A_P/A	A_P/A_1
4	10.73	0.156	1.490	0.022	0.006	0.015
8	13.00	0.537	1.806	0.075	0.021	0.041
12	14.01	1.337	1.946	0.186	0.052	0.095
16	14.43	1.770	2.004	0.246	0.068	0.123
24	16.04	2.888	2.228	0.401	0.111	0.180

Table 4. Spanwise data for the low speed wake forced at 9%.

x (cm)	A_1 (cm^2)	A_P (cm^2)	$\langle\delta_1\rangle$ (cm)	$\langle\delta_P\rangle$ (cm)	A_P/A	A_P/A_1
4	10.50	0.470	1.458	0.065	0.018	0.045
8	13.78	1.341	1.914	0.186	0.052	0.097
12	15.00	2.528	2.083	0.351	0.098	0.169
16	15.99	3.283	2.221	0.456	0.127	0.205
24	16.41	4.102	2.279	0.570	0.158	0.250

Data from a representative spanwise location (z = 0.0 cm) are shown in Figure 65 for the 5% and 9% amplitude cases. The sold line marks the mean data from the streamwise imaging cases. Differences between the streamwise and spanwise data in Figure 65 are typical of other spanwise locations. Usually the spanwise data agrees well with the streamwise data. δ_1 values from the spanwise data show an approximately equal probability of being above or below the streamwise data, but stay close to the streamwise data. δ_P values for the spanwise data are also close to the streamwise mean, but are always lower than the streamwise values. The differences ranges from 5% (x = 24 cm, 9% forcing) to 22% (x = 16 cm, 9% forcing). However, the extreme discrepancy of 22% is in a region of rapid growth in δ_P.

Interestingly, the assertion that spanwise imaging may be less accurate at low x is not supported by the data. Figure 65 does not suggest any magnification in the differences between streamwise and spanwise data for low x.

3.4 Comparison with Previous Nonreacting LIF Data

MacKinnon & Koochesfahani (1993) used nonreacting LIF to measure the downstream evolution of the mixed-fluid fraction A_m for several forcing amplitudes. The present data can be compared to previous nonreacting data if the assumption is made that the wake entrains the same amount of fluid from the top and bottom streams, leading to the conclusion $A_m = 2A_P$ (see §2.4). This assumption is supported, at least in highly mixed cases, by both Roberts (1985) and MacKinnon & Koochesfahani (1993).

Figure 66 is a comparison of A_m/A based on nonreacting LIF (MacKinnon & Koochesfahani) with A_m/A calculated with reacting LIF (the present study) using the assumption $A_m = 2A_P$. The unforced and 9% forcing cases are shown in Figure 66; complete data are provided in Table 5. As expected, the nonreacting technique always overpredicts the amount of mixing. However, the difference in the two techniques is much greater at low x. For example, A_m/A at x = 24 cm and 9% forcing is 1.31 times higher for the nonreacting data compared with the reacting data. At x = 4 cm, the nonreacting data is 6.81 times higher for the same forcing conditions. This behavior makes sense. The problem with nonreacting LIF is it labels unmixed fluid as mixed due to resolution limitations (Figure 2). If there is more *actual* mixed fluid present in the wake, the nonreacting technique would be expected to mislabel less fluid. In other words, the nonreacting LIF technique is completely accurate in the limit that all fluid is actually mixed.

The order of magnitude increase in mixing for the forced flow compared with the unforced flow observed at x = 25 cm (Roberts, 1985) and x = 24 cm (MacKinnon & Koochesfahani, 1993) is also supported in the present data. At x = 24 cm, A_m/A is 15.8 times higher for the wake forced at 9% than for the unforced wake.

Table 5. Comparison of A_m/A for nonreacting and reacting LIF.

	nonreacting				reacting			
x (cm)	**none**	**1.6%**	**5.6%**	**9.1%**	**none**	**2%**	**5%**	**9%**
1.8	0.013	0.037	0.075	0.123	----	----	----	----
4	0.014	0.125	0.221	0.245	0.004	0.004	0.012	0.036
8	0.015	0.131	0.245	0.296	0.004	0.006	0.042	0.104
12	----	----	----	----	0.008	0.038	0.104	0.196
16	0.017	0.176	0.267	0.352	0.012	0.064	0.136	0.254
24	0.031	0.225	0.314	0.413	0.020	0.140	0.222	0.316

3.5 The Low Speed Wake: A Summary

Results have been presented for both streamwise and spanwise imaging of the low speed wake. These results comprise a primary goal of this study. The data show that forcing the wake at high amplitude greatly enhances the resultant mixing downstream. The wake forced at an amplitude of 9% exhibited more than an order of magnitude increase in product compared with the unforced case at x = 24 cm.

Data measured from spanwise and streamwise imaging are similar. The product thicknesses, though, measured from spanwise viewing are about 10% lower than the same cases measured from streamwise viewing. This discrepancy seems independent of streamwise location.

As expected, comparison with previous data measured from nonreacting LIF shows that the nonreacting method overpredicts the amount of mixing. The overprediction is more pronounced for low x, where there is little mixing. Overprediction can be as low as 31% for the most highly mixed flow studied.

Chapter 4

RESULTS FOR THE HIGHER SPEED WAKE

This section presents visual and quantitative results for a higher speed (U_o = 20 cm/s) wake. This flow was studied to see what differences in wake growth and structure occur at higher Reynolds number. Higher speed wake experimental data was recorded only when there was additional fluid remaining in the facility's supply reservoirs after the low speed runs were completed. However, there is a substantial data set for the unforced higher speed wake and the higher speed wake forced at 12 Hz with < 1% RMS amplitude. Note that the observed natural roll-up frequency for the higher speed wake was about 17 Hz. Thus, $f/f_o \approx 0.7$ for the higher speed wake compared with $f/f_o \approx 0.9$ for the low speed wake.

4.1 Streamwise Results

Streamwise results for the higher speed wake exist for several locations. Experimental runs were performed for the forced higher speed wake at z = 0.0 cm (high x), z = +0.8 (low, mid, and high x), z = -0.8 cm (low and mid x), and z = -2.0 cm (low, mid, and high x). Runs for the unforced higher speed wake were done at z = +0.8 cm (mid and high x), and z = -2.0 cm (mid and high x).

4.1.1 Flow Visualization

Images of the higher speed wake are presented in Figures 67-71. These figures use the same format as the images of the low speed wake (Figures 10-25), including the color mapping. Missing images represent gaps in the recorded data.

The unforced higher speed wake (see Figures 67 and 70) is characterized by a narrow, somewhat unstructured vortex street with periodic regions of more highly mixed fluid. There is considerably more activity than was observed for the low speed wake (see, for example Figure 10). Examination of the average images reveals that the unforced higher speed wake, like the low speed wake, grows slowly as it moves downstream.

The forced higher speed wake exhibits a much different structure from the unforced wake, even at the very low forcing amplitude studied (Figures 68, 69, and 70). The wake width is considerably larger for the forced wake and the structure is more periodic. The forced higher speed wake closely resembles the low speed wake forced at 2% (see Figure 11), however, like the unforced higher speed wake there are periodic regions of higher intensity mixed fluid. A good example of this can be seen in the mid x image in Figure 69. The average images in Figures 68, 69, and 71 show an increasing wake width moving downstream. The region of constant wake width seen in the low speed wake forced at 2% is not evident in the higher speed forced wake.

4.1.2 Calculated Quantities

The quantities calculated from streamwise imaging of the higher speed wake are shown for the unforced and the forced cases in Figures 72 and 73, respectively. δ_1 for the unforced higher speed wake (Figure 72a) increases gradually moving downstream. The wake is slightly wider at z = -2.0 cm than at z = +0.8 cm. The same basic pattern appears in the product thickness, Figure 68b. The product thickness of the wake half way between midspan and the sidewall (z = -2.0 cm) is about 2.6 mm at x = 24 cm. The value at the same x location for z = +0.8 cm is 1.7 mm. The normalized product thickness for the unforced higher speed wake is plotted in Figure 72c.

The 1% thickness for the forced higher speed wake is shown in Figure 73a. δ_1 is relatively uniform at all four spanwise (z) laser sheet positions and the wake width increases with increasing x. The forced wake is considerably thicker than the unforced wake. At x = 24 cm, the forced wake thickness is about 2.8 cm compared to 2.3 cm for the unforced wake (at z = -2.0 cm). The product thickness for the forced wake, Figure 73b, shows a considerable spread in the data. At x = 24 cm, the product thickness varies from 1.8 mm to 3.1 mm due to the highly three-dimensional behavior of the higher speed wake (which will be seen in the spanwise images). These values are similar to the product thicknesses for the unforced higher speed wake. The normalized product thickness for the forced higher speed wake, Figure 73c, ranges from 0.065 to 0.110 at x = 24 cm. δ_p/δ_1 values for the unforced wake at this location fall within this range, but in general the unforced higher speed wake has slightly more normalized product than the forced wake. This is because the unforced wake shows a similar amount of product, but it carries it in a narrower width.

4.2 Spanwise Results

The forced higher speed wake was imaged at five streamwise locations: $x = 4$, 8, 12, 16, and 24 cm. In addition, the unforced higher speed wake was imaged at $x = 16$ cm.

4.2.1 Flow Visualization

Chemically reacting LIF images of the forced higher speed wake are presented in Figures 74-76 and 78-79. The unforced higher speed wake at $x = 16$ cm is shown in Figure 77. Each Figure contains a total of five images corresponding to one complete forcing cycle of the wake. The images are separated in time by $\Delta t = 1/60$ s. The range covered in each image is approximately $z = -3.9$ cm to $+3.9$ cm and $y = -1.9$ cm to $+1.9$ cm. The greyscale mapping for each Figure is indicated below the images. The lowest value of C_P^* that has been mapped to white is noted in the caption of each Figure.

$x = 4$ cm

One forcing cycle of the forced higher speed wake at $x = 4$ cm is shown in Figure 74. Overall intensities are very low, but a relatively narrow structure can be seen that varies greatly across the test section span.

$x = 8$ cm

The structure of the higher speed wake is more clear in Figure 75. The fluorescent interfaces have a decided corrugated appearance, suggesting a series of streamwise vortices across the test section span. The regions of highest mixing seem to be near each side wall which is similar to the pattern observed in the low speed wake.

x = 12 cm

This development is even more evident in Figure 76, the forced higher speed wake at x = 12 cm. A series of structures, apparently streamwise vortices, distort the fluorescent mixing interface across the test section span. Higher C_P^* values associated with the streamwise structures near the side walls suggest that the structures near the walls may have originated from reorientation of the spanwise vortex structures in the side walls' boundary layer. If this is true, the streamwise vortices in the central part of the test section must have originated from some other mechanism.

x = 16 cm

The single spanwise unforced higher speed wake case is shown in Figure 77. The width of the unforced wake is lower than the forced cases. The highest intensities are near the side walls, similar to the forced wake cases.

The forced higher speed wake at x = 16 cm is shown in Figure 78. The structure of the wake here is much the same as it was further downstream. The streamwise structures have radically stretched and distorted the spanwise wake cross-section.

x = 24 cm

Further evidence of this is seen in Figure 79, the higher speed forced wake at x = 24 cm. The wake is highly three-dimensional across the entire test section. Even at this downstream location, though, the intensities near the test section side walls are higher than in the central part of the test.

The streamwise vortices often contain a significant amount of well-mixed fluid and may extend well above or below the primary extent of the wake. The presence of periodic regions of mixed fluid seen in some of the streamwise images of the higher speed wake (see, for example, Figure 69) can probably be attributed to these streamwise structures moving into the plane of the laser sheet.

Average Images

Time-averaged images ($\overline{C_P^*}(y,z)$ images) of the spanwise higher speed wake are presented in Figure 80. These images have been pseudocolored using the same colormap as the streamwise images of Figures 67-71. The average images show the development of streamwise vorticity even at low x. These images, especially at x = 16 and 24 cm, show that the streamwise structures occur at discrete spanwise positions—they are certainly not random. A total of seven streamwise structures across the test section span are seen for both the unforced and forced wake indicating a spanwise spacing of about 1.1 cm. In addition, these average images show that the streamwise vortices nearest the side walls contain the largest amount of mixed fluid, similar to what was seen in the instantaneous images. The images in Figure 80 form the basis for the calculated data below.

4.2.2 Calculated Quantities

Conventional line plots of $\overline{C_P^*}$ extracted from Figure 80 at several spanwise (z) locations and each streamwise location studied are presented in Appendix E. Plots of δ_1, δ_P, and δ_P/δ_1 measured from Figure 80 are shown in Figure 81. Figure 81a indicates that the wake width increases with increasing x. Also, the width shows more variation across the test section (due to the streamwise structures) at higher x locations. δ_1 for the unforced wake at x = 16 cm is about 65-70% of its value for the forced wake at the same x location.

The product thickness of the wake, Figure 81b, also increases moving downstream. The peak product thicknesses are near the test section side walls, which agrees with the instantaneous flow images. δ_P for the unforced wake is, again, slightly lower than the forced wake at x = 16 cm. The decrease in product thickness is offset by the reduction in wake thickness resulting in nearly identical normalized product thicknesses for the unforced and forced wake at x = 16 cm (Figure 81c). Peak values of δ_P/δ_1 greater than 0.20 are achieved by the higher speed forced wake at x = 24 cm.

Span averaged and integrated data

Span averaged and integrated data for the higher speed wake are presented in Table 6. Data for both the unforced and forced wake are shown at x = 16 cm and are indicated as "(uf)" and "(f)" in the Table. Substantial growth in both the 1% area and product area are seen with increasing downstream distance. The maximum value of A_P/A_1 is 0.127 at x = 24 cm. This is similar to the value seen for the low speed wake forced at 2% amplitude at the same location ($A_P/A_1 = 0.125$).

In summary, the higher speed wake shows a downstream evolution similar to the low speed wake. There is a clear increase in both the area occupied by the wake and the amount of mixed product in the wake. Forcing the wake at small amplitude did not noticeably increase the amount of normalized product. Regions of streamwise vorticity near the side walls, as in the low speed wake, exhibited the strongest levels of mixing in the wake. In addition, however, the higher speed wake showed pronounced three-dimensionality in the central portion of the test section even at low x. It is suggested that the three-dimensionality in the center of the test section is the result of a mechanism separate from the mechanism that produced the structures nearest the side walls.

Table 6. Spanwise data for the higher speed wake

x (cm)	**A_1 (cm^2)**	**A_P (cm^2)**	**$\langle\delta_1\rangle$ (cm)**	**$\langle\delta_P\rangle$ (cm)**	**A_P/A**	**A_P/A_1**
4	9.23	0.059	1.247	0.008	0.002	0.006
8	13.23	0.131	1.838	0.018	0.005	0.010
12	16.07	0.772	2.232	0.107	0.030	0.048
16 (uf)	11.43	0.876	1.588	0.122	0.034	0.077
16 (f)	17.57	1.307	2.440	0.182	0.050	0.074
24	19.73	2.504	2.740	0.348	0.097	0.127

Chapter 5

RESULTS FOR THE FALSE WALL AND PEG CASES

5.1 False Wall Cases

Chapters 3 and 4 both showed that the regions of the wake showing the most mixing were dominated by streamwise vortices. It is also clear that much of the streamwise vorticity is generated from the side walls of the test section. What is not known is the exact mechanism responsible for this vorticity generation. It has been postulated in this study, and also in Roberts (1985), that the streamwise vorticity is generated by the primary spanwise vortex street being stretched and reoriented—'tipped'— in the side walls' boundary layers. Another possibility, though, is that at least some of this vorticity results from corner vortices generated in the boundary layers upstream of the splitter plate tip. One way to test Roberts' vortex tipping hypothesis is to insert a false side wall into the test section at midspan. Corner vortices are not possible from the false wall, hence generation of streamwise vorticity from the false wall implies reorientation of the spanwise vortices.

Roberts (1985) discusses an experiment preformed in this fashion. A false wall was inserted into the test section such that its leading edge was at a location approximately 3 cm upstream of the splitter plate tip. His results suggest that the vortex tipping process still occurs on the false wall, thus he concluded that a no-slip boundary condition alone was sufficient to generate streamwise vorticity in the wake.

The present investigation is an extension of Roberts' work. Several experiments were conducted with a vertically oriented plate (false wall) inserted in the test section. The false wall was placed such that its leading edge was either flush with the splitter plate tip ($x = 0$ cm) or a short distance downstream ($x = 3.5$ cm). A schematic of this setup is shown in Figure 82. The false wall was thin, about 0.5 mm, and the leading edge was rounded off to minimize flow separation. The false wall was positioned at midspan across the entire transverse extent of the test section. Nonreacting LIF image sequences were acquired at five x locations: $x = 1.8$, 4, 8, 16, and 24 cm. At each of these locations the wake was forced at 5% and 9% amplitude.

Images are presented in the same format as previous spanwise data: ten images for each case corresponding to one complete forcing cycle. Each image shows only one-half of the test section (i.e., the test section span between the side wall and the false wall). During the experiments the camera was focused on the half of the test section that produced the best image quality. The images to follow have been processed so that the false wall is always at the left edge of each image and the true side wall of the test section is always at the right edge.

5.1.1 False Wall at x = 0 cm

Figures 83-87 are images of the wake with the false wall's leading edge at x = 0 cm. With the laser sheet at x = 1.8 cm, Figure 90, the wake has already begun to roll-up and shows streamwise vorticity near the side wall for both 5% and 9% forcing. There is little evidence of any streamwise vorticity near the false wall. This indicates that at least a portion of the streamwise vorticity near the side wall is generated upstream of the splitter plate tip.

Figure 84, the wake at x = 4 cm, reveals a much different structure. Streamwise vortices are well defined at both the side wall and the false wall. The vortical structures nearest the side wall are larger than those at the false wall, which gives the wake a somewhat slanted appearance. This appearance is even more pronounced in Figure 85, x = 8 cm. The upper edge slants downward toward the false wall for both the 5% and 9% forcing amplitude cases. Figures 86 and 87, images of the wake at x = 16 cm and x = 24 cm, show evolutions similar to cases without the false wall. The streamwise vorticity, and as a result mixing, move away from the side walls—both the true side wall and the false wall—into the central portion of the test section. Both the 5% and 9% forced wakes are quite well-mixed at x = 24 cm.

In conclusion, at least part of the streamwise vorticity near the side wall is generated upstream of the splitter plate tip. This is based on the earlier development and subsequent increased size of the streamwise vortex structures near the side wall. However, streamwise vorticity is generated from the false wall. This shows that Roberts' vortex tipping mechanism is at least partially responsible for streamwise vorticity production in the wake.

5.1.2 False Wall at x = 3.5 cm

Images acquired with the false wall's leading edge at x = 3.5 cm are presented in Figures 88-92. With this configuration the wake reaches the false wall at a distance equal to about two forcing wavelengths downstream of the splitter plate tip. Thus, the vortex street has some time to develop before impacting the plate.

Figure 88 shows images of this wake configuration at x = 1.8 cm. This is upstream of the false wall, therefore the structure of the wake is the same as if the plate was not there. There are clear streamwise vortex structures in the far right of each image with a relatively two-dimensional structure away from the true side wall. Several small streamwise disturbances can be discerned across the span, however. These disturbances must have originated upstream and become amplified as the wake moved downstream. At x = 4 cm (Figure 89) the streamwise structures are clearly larger in amplitude. At this laser sheet position, the wake has just reached the false wall and it is still difficult to recognize any change in the wake due to the plate. The influence of the false wall is definitely felt at x = 8 cm, Figure 90. Streamwise vortices are evident near the false wall for both 5% and 9% forcing. The slanted appearance of the wake first seen with the false wall at x = 0 cm also appears for the two cases in Figure 90.

By x = 16 cm (Figure 91) the wake has developed much more. The streamwise vortices originating from the side walls have moved farther into the test section center than those originating from the false wall resulting in a wake structure skewed toward the center of the test section (i.e., the left-hand side of the images). This is particularly obvious for 9% forcing amplitude. Another feature in Figure 91 is the apparent disappearance of the previously observed streamwise structures. Because the images in Figure 91 are from the left half of the test section and the images in Figures 88-90 are from the right half of the test section, it is probable that the streamwise structures are the result of upstream disturbances (bubbles or particles) in the right half of the test section.

Figure 92, $x = 24$ cm, is also from the left half of the test section. Both the 5% and 9% forcing cases show a considerably different structure than the same cases with the false wall beginning at $x = 0$ cm. The 9% forcing case is highly mixed over approximately the left two-thirds of the images, with very little mixing near the true side wall of the test section.

These results suggest that streamwise placement of the false wall does not affect the development of streamwise vorticity. Although the structure of the wake is different near the false wall, streamwise vorticity does develop. Based on these results, it appears that any no-slip boundary (producing a velocity gradient $\partial \mathbf{u}/\partial z$) in the test section will result in the generation of streamwise vorticity. Although no mixing measurements were evaluated, it appears that this three-dimensionality may also lead to an enhancement in mixing downstream.

5.2 Peg Cases

The results for the false wall suggest that any no-slip boundary will produce streamwise vorticity downstream by stretching and reorienting the primary spanwise vorticity. Many other forms of disturbance could be imposed on the wake both upstream or downstream of the splitter plate tip. One such disturbance is a three-dimensional body placed within the boundary layer near the splitter plate tip. This is clearly much different from the false wall. Would it, too, produce streamwise vorticity downstream?

This question was answered by performing a series of experiments with a small cylindrical peg ($d = 7$ mm, $h = 1$ mm) placed on the upper surface of the splitter plate approximately 5 cm upstream of the splitter plate tip ($x = -5.0$ cm). This configuration is illustrated in Figure 93. Note that the Reynolds number based on the peg diameter and $U_o = 10$ cm/s is about 700, thus it is possible that the peg may shed vortices. Image sequences were acquired for the unforced flow and the flow forced at 2%, 5%, and 9% RMS of the free stream speed $U_o = 10$ cm/s at streamwise locations $x = 16$ and 24 cm.

Data collected from these experiments are not analyzed quantitatively in this report. Because of this, the experimentally simpler nonreacting LIF technique was used for all the peg cases. Instantaneous flow images are presented for each forcing condition studied. The format for these images is the same as that used for the chemically reacting spanwise images: ten consecutive images separated temporally by $\Delta t = 1/60$ s.

x = 16 cm

Instantaneous flow images for the peg wake at x = 16 cm are presented in Figures 94-97. Figure 94, the unforced wake, shows a wavy interface between the two fluid streams. There is a noticeable indentation in the center of the test section apparently resulting from the peg upstream. Despite this, the unforced peg wake is not dramatically different in structure from the unforced wake without the peg (Figure 49). With 2% forcing applied, Figure 95, there is a definite change in the wake structure. The peg results in the appearance of streamwise vortices on either side of midspan both above and below the wake centerline. Similar trends can be seen in the wake forced at 5%, Figure 96. Again, there are pairs of counterrotating streamwise vortices resulting from the peg upstream. In certain cases the influence of the peg seems to nearly cut the wake in half (see, for example, the fourth image in the lefthand column). Figure 97 shows the structure of the peg wake with 9% forcing. With this forcing amplitude the peg affects the structure of the wake so radically that it is completely different from the same wake without the peg seen in Figure 52. The structure of the peg wake is also highly asymmetric with respect to the z-axis. Much of the activity appears to be constrained to the upper half of the test section, although the wake actually impacts the bottom wall of the test section at certain locations. Another interesting feature is the small counterrotating streamwise vortex pair that appears 'hanging' below the wake at midspan. Notice that the core of this structure always appears black, indicating pure fluid from the upper free stream.

x = 24 cm

The unforced peg wake at x = 24 cm is shown in Figure 98. There is significantly more activity here than at x = 16 cm, but the overall structure is still very similar to the same wake without the peg (see Figure 53). The peg wake forced at 2%, Figure 99, is also similar to the same wake without the peg, Figure 54. However, the peg clearly alters the structure near midspan. As at x = 16 cm, the wake forced at 5% (Figure 100) appears nearly severed at midspan and it is incredibly symmetric. Comparison with the same flow without the peg, Figure 55, shows that the peg has significantly altered the wake structure. With a 9% forcing amplitude applied, Figure 101, the peg wake at x = 24 cm becomes very highly mixed. As was seen with this forcing amplitude upstream, there is significant asymmetry with respect to the z-axis. The wake impacts the bottom of the test section regularly, but still does not appear to reach the test section top wall. The small counterrotating vortex pair is still evident near midspan in several images, but is generally less pronounced than it was further upstream.

5.2.1 Discussion

Figures 94-101 show that placing a small three-dimensional disturbance upstream of the splitter plate tip generates streamwise vorticity downstream. Although these data were not quantitatively anayzed, it appears that the additional streamwise vorticity generated by the peg may also lead to an enhancement of mixing.

A sample image from the peg wake is shown in Figure 102a. This image is from x = 16 cm at 5% forcing amplitude and is the same image shown in the bottom left corner of Figure 96. The dominant features in the center of the test section are the opposite signed, paired streamwise vortices both above and below the z-axis. This image is well downstream of both the splitter plate tip and the peg, so it is difficult to establish the exact origin of the structures present. It is clear, though, that the streamwise vortices near midspan are a direct result of the peg. A simplified sketch showing the relative strengths and signs of the streamwise vortices is given in Figure 102b. An explanation of the mechanism resulting in this structure is beyond the scope of this report. However, the reader is referred to Lasheras et al. (1986) for an excellent discussion on the development and mechanics of streamwise vorticity in shear flows. Although their paper deals specifically with shear layers, many of the structures are strikingly similar to those observed in the present work.

In summary, both no-slip boundaries studied (the false wall and the peg) resulted in the production of streamwise vorticity in a low Reynolds number wake flow. Since streamwise vorticity is responsible for increased mixing in the wake, inserting a false wall or peg into the flow may also increase the level of mixing achieved.

Chapter 6

CONCLUSIONS

The structure and mixing of a forced, liquid phase splitter plate wake have been studied with both streamwise and spanwise imaging using chemically reacting LIF. The low speed wake (U_o = 10 cm/s) was examined at 2%, 5%, and 9% forcing amplitude in addition to the unforced case. A higher speed wake (U_o = 20 cm/s) was studied on a more limited basis for both unforced and low amplitude forcing cases. Additional data were acquired using the nonreacting LIF technique for two different base flow situations. One of these situations used a vertically oriented thin plate (false wall) placed at the test section midspan. The second situation used a small cylindrical peg placed on the upper surface of the splitter plate. The following conclusions are supported by data from these experiments.

Forcing the low speed wake, especially at high amplitude, at a frequency near the natural wake roll-up frequency greatly increases scalar mixing downstream. Streamwise vorticity originating from the side walls of the test section is the primary mechanism resulting in this increase in mixing. At x = 24 cm there is about 40 times as much product at midspan for the wake forced at 9% amplitude as for the unforced wake. The highly mixed wake, however, is concentrated in the center of the test section with the regions near the side walls showing almost no mixing. Because of this, the total amount of product integrated across the test section span for the 9% forcing case is only about 16 times higher than the unforced case.

Although chemically reacting LIF is expected to produce accurate measurements of mixing product, several factors can contribute to uncertainty in the data. Uncertainty in forcing frequency and free stream velocity contribute to a perceived expansion or compression of the nondimensionalized streamwise coordinate x^*. Also, small errors in the forcing amplitude cause a shift in δ_P (and δ_1). These errors can be significant. For example, a 5% error in setting the forcing amplitude (i.e., forcing the flow at 9.5% instead of 9%) at midspan will result in a 17% error in the product thickness. Therefore, it is extremely important to set and monitor the flow parameters as accurately as possible.

Previous results have been reported for the same wake conditions, but using nonreacting LIF. Based on the current results, nonreacting LIF overpredicted mixing at x = 24 cm with 9% forcing by 31%. Larger discrepancies were found between the data at low x (x = 4 and 8 cm). At x = 4 cm the wake with 9% forcing exhibited 6.81 times as much mixed fluid using the nonreacting technique.

The higher speed (U_o = 20 cm/s) wake exhibited behavior different from the low speed wake. Spanwise images show that the high speed wake, both unforced and with a small amount of forcing applied, is highly three-dimensional across its entire span. Stronger streamwise vortices are observed near the side walls similar to those seen in the low speed wake. However, there are also a series of smaller streamwise vortices in the central portion of the test section. It is suggested that these smaller vortices are generated from a mechanism different from the vortices nearest the side walls. The low speed wake, conversely, showed only weak three-dimensionality in the center of the test section (except the highest forcing amplitude) even at high x. Forcing the high speed wake at low amplitude resulted in an increase in wake width of about 30%, but did not significantly alter the amount of product across the wake.

Images with the false wall mounted in the test section at $x = 0$ cm and $x = 3.5$ cm show that the reorientation and stretching of the spanwise vortices is responsible for some streamwise vorticity in the wake. Streamwise vortices are observed near the false wall even at $x = 4$ cm with the false wall mounted so that its leading edge touches the splitter plate ($x = 0$ cm). The streamwise vortices near the true wall are stronger, though, suggesting that another mechanism contributes to the generation of streamwise vorticity, as well. When the plate is mounted with its leading edge at $x = 3.5$ cm, corresponding to approximately two forcing wavelengths, the wake proceeds unaffected at midspan until it impacts the false wall. Downstream of this point streamwise vortices begin to appear near the false wall. Therefore, production of streamwise vorticity is not dependent on the location of the false wall.

Another source of three-dimensional disturbances was studied by placing a small cylindrical peg on the upper surface of the splitter plate upstream of the tip. Wake images show the peg greatly affects the structure of the wake downstream, especially for higher amplitude forcing. The peg introduces counterrotating streamwise vortices near the test section midspan. These vortices increase the overall three-dimensionality of the wake and split the wake into two symmetric halves. No quantitative measures of mixing were attempted, but it is possible the streamwise vorticity generated by the peg increases the overall level of mixing in the wake.

APPENDICES

APPENDIX A

Notes on the Chemically Reacting LIF Technique

A.1 Chemical Properties of Fluorescein Dye

A.1.1 pH Dependence

An important characteristic of fluorescein dye is its pH dependence. Fluorescein dye fluoresces efficiently when excited by an argon-ion laser, but only when it is in an environment with a pH ≥ 4. A plot of recorded fluorescence intensity versus solution pH is shown in Figure A.1. For low pH the fluorescence is effectively 'turned off,' but as the pH increases above the threshold value (pH ≈ 4) a rapid increase in fluorescence occurs. The intensity increases with increasing pH until a maximum is reached. This intensity maximum corresponds to pH ≈ 8. For pH > 8 the intensity remains virtually constant at the maximum value.

During the experimental runs the fluorescein dye was premixed with the acidic stream. The acidic stream had a pH < 4, so initially the fluorescence was turned off. Reaction with the basic stream resulted in an increase in pH and a corresponding rise in the fluorescent intensity as shown in Figure A.1. By titrating the base solution into the acid/dye solution, the intensity as a function of the base volume fraction $\xi_B = v_B / (v_A + v_B)$ was determined.

A typical plot is shown in Figure A.2. Unlike the intensity-pH behavior, which is a characteristic of the dye, the intensity-ξ_B curve depends on the relative concentrations of the acid and base solutions. The intensity is zero for low ξ_B and rises sharply near the intensity turn on threshold ξ_S. After the peak fluorescent intensity is reached addition of more base merely dilutes the solution, thus the intensity should decrease linearly to zero for ξ_B approaching unity. It is desirable to keep the value of ξ_S close to zero so that nearly all the reaction product fluoresces. For the present study ξ_S was generally in the range $\xi_B = 0.06$-0.07. This required acid and base concentrations of approximately 0.2 mM and 5.8 mM, respectively.

A.1.2 Bleaching

Excitation of fluorescein dye over time results in a loss of absorption efficiency due to a process known as photobleaching. Bleached dye molecules do not absorb the laser light resulting in a perceived reduction in dye concentration. The number of absorbing dye molecules decays exponentially in time as

$$\frac{n}{n_o} = e^{-t/\tau_b} \tag{A.1}$$

where n_0 is the number of molecules absorbing at time $t = 0$, n is the number of molecules absorbing at time t, and τ_b is the bleaching time constant. τ_b is a function of the dye used, the laser photon flux (the number of photons per unit area per unit time), and the dye absorption cross section (Koochesfahani, 1984). Koochesfahani (1984) calculated a value of $\tau_b \approx 20$ s for his experiments, meaning that only 37% of the dye molecules would still be absorbing after 20 seconds. Obviously bleaching problems can be significant.

However, the problem of bleaching is greatly reduced in flowing systems. If the dye bearing fluid passes through the laser sheet in a time much less than τ_b bleaching becomes negligible. The titration reference chamber is more sensitive to bleaching because the same fluid remains in the chamber throughout the experiment. Bleaching is reduced, though, by continuously circulating the fluid and by making the volume of fluid covered by the laser sheet much smaller than the total volume of the chamber. A plot of measured fluorescent intensity versus time for the titration reference chamber is shown in Figure A.3. A curve fit to Equation A.1 results in $\tau_b = 6329$ s for 2 W laser power and 4329 s for 3 W laser power. The maximum laser power used in any experiment was 4 W, so a worst case of $\tau_b \approx 3200$ s is expected. The laser was blocked between the experimental runs, so it is estimated that the reference chamber was exposed to laser light for 300 s at most. Even so, this represents about a 7% drop in the chamber intensity between the start and finish of the experiment. To minimize bleaching effects, the intensity of the chamber near the *start* of each experiment was used as the normalization constant $(I_f)_{max}$.

A.2 Product Concentration Measurement

Chemically reacting LIF analysis is based on a one-step, infinitely fast, reversible reaction of the type $A + B \rightarrow P$. For this reaction the product concentration C_P is dependent on the two reactant concentrations. If the reactants A and B are carried in two fluid streams at concentrations of C_{1o} and C_{2o}, respectively, the product concentration C_P is defined as

$$C_P(\xi;\xi_S) = \begin{cases} C_{1o}\xi & for\ \xi < \xi_S \\ C_{2o}(1 - \xi) & for\ \xi > \xi_S \end{cases} \tag{A.2}$$

(see Figure A.4) where ξ is the volume fraction of reactant C_{2o} and ξ_S is the stoichiometric mixing ratio (Koochesfahani, 1984). In a chemically reacting LIF experiment, with the acid/dye as one reactant and the base as the other, C_P versus ξ_B is as shown in Figure A.5. The right triangle shape of Figure A.5 is similar to Figure A.2 and the fluorescence intensity can be used to estimate the product concentration by using the relation

$$\frac{C_P}{(C_P)_{max}} = \frac{I_f}{(I_f)_{max}} \tag{A.3}$$

where $(C_P)_{max}$ is the maximum possible product concentration, I_f is the fluorescence intensity, and $(I_f)_{max}$ is the maximum fluorescence reached at the fluorescence threshold (Koochesfahani & Dimotakis, 1986). Note that $(I_f)_{max}$ is available throughout the experiment in the titration reference chamber.

APPENDIX B

Image Processing

B.1 Free Stream Intensity Elimination

Ideally, the fluorescent intensities in both free streams will be zero. In reality the upper stream, carrying the acid and dye, has nonzero intensity. Typically, values of about 5-7 counts were recorded in the upper stream compared with $(I_f)_{max} \approx 200$. Although these values are small, they cannot be neglected and measures were taken to effectively 'filter' out the upper free stream contribution to δ_P and δ_1.

From the acquired image sequences it is a simple task to identify the upper free stream intensity values present. Once the maximum value has been determined, one possible method to eliminate the free stream contribution is simply to set all intensities at or below this value to zero in each image of the sequence. The problem with this method is it may also eliminate the contribution of some real phenomena. Because of this, an improved method was used. Each column in each image was read and processed separately by the computer. If the intensity along the column fell below the free stream value *for a specified number of consecutive rows* the intensities were set to zero. This method reduces the possibility of actual product being filtered out. An example of this process is illustrated in Figure B.1. Pure fluid from each of the two streams is labeled differently in the simulated streamwise flow image in Figure B.1. Mixing occurs on the thin interface indicated by the white band connecting the two fluid streams. Along the column shown by the dashed line in the flow image, the unprocessed intensity profile will resemble that shown in the plot labeled "Raw data." There are sharp intensity spikes at the mixing interface and regions of low intensity and zero intensity corresponding to fluid from the upper and lower streams. respectively. The filtering process will identify the nonzero intensity contribution from the upper stream and set all these intensities to zero, as shown in the plot labeled "Filtered data" in Figure B.1.

The number of consecutive rows γ needed before intensities were set to zero had to be determined before processing. Setting γ too low may result in eliminating real features, while setting γ too high can allow some free stream intensity to remain unfiltered. Selecting the value of γ is made even more difficult because different flows are affected differently by it. Figure B.2 shows the effect of varying γ on an unforced wake at low x. The actual case shown is at z = 0.8 cm, x = 6 cm. The solid line marked "unprocessed data" shows the calculated δ_P without any processing. Note that this value is about an order of magnitude higher than the processed values, shown as circles. For this case there is a slight increase in δ_P moving from $\gamma = 1$ (i.e., *all* intensities less than or equal to the maximum free stream value are set to zero) to $\gamma = 2$, but further increase in γ shows very little change. This is expected for this case because the mixing interface is a single wavy line (see Figure 14).

Figure B.3, on the other hand, is very sensitive to γ. The case depicted in Figure B.3 is the wake at z = 0.8 cm, x = 14 cm forced at 5% (see Figure 16), which is a tightly rolled up vortex street. For this case the solid line indicating unprocessed data shows about a 40% increase in δ_P compared with $\gamma = 2$, much closer than the order of magnitude difference seen in Figure B.2. The reason for the gradual increase in δ_P with increased consecutive rows is coupled to the structure of this flow. Increasing γ causes the filtering algorithm to miss regions of upper free stream fluid between the tightly spaced interfaces. Unfortunately, for such cases it is difficult to know what value of γ is 'correct.' Spacing of the interfaces in the flow images suggest γ in the range 2-4 should give satisfactory results in all cases. Therefore, $\gamma = 3$ was used for each case in this report.

Figure B.4 illustrates the effects of varying γ for a highly mixed case. The case illustrated is at z = -0.8 cm, x = 21 cm and is forced at 9% amplitude (see Figure 21). For the highly mixed wake the product thickness is almost totally insensitive to changes in γ. In fact, the data in Figure B.4 suggest that filtering has very little effect whatsoever—the solid line indicating unprocessed data is at essentially the same δ_P as the filtered cases. This suggests that when the wake is highly mixed the probability of finding pure upper stream fluid is small.

B.2 Camera 'Offset' Correction

An important factor to consider in LIF is the black level offset of the camera used. Consider the data shown in Figure B.5, which is a plot of intensity versus exposure time for the Sony XC-77RR CCD camera used in the present study. Ideally, as exposure time approaches zero (i.e., no light) the recorded intensity should approach zero. Extrapolating the data in Figure B.5 shows that this camera has an intensity offset of about -5. That is, at zero exposure the true intensity would be -5 counts. In practice, this translates to the recorded intensity being zero though there is a finite amount of light exciting the CCD array. The problem this causes is illustrated in Figure B.6. If Figure B.6a is the intensity versus ξ_B behavior of a camera with zero offset, a camera with a finite negative offset would record $I_f(\xi_B)$ as shown in Figure B.6b. Of course, the negative intensities are recorded by the digitizer as zero, so the net effect is a perceived lower overall intensity level. This in itself is not a problem, but errors arise when the intensities are divided by the reference value I_{fo}. If, for example, a camera with zero offset recorded an intensity value of 50 at some location and the value of I_{fo} recorded by the same camera was 200, the normalized value at this location would be 50/200 = 0.25. A camera with an offset of -5 would record the intensity at the same location as 45 with I_{fo} = 195 producing a normalized value of 45/195 = 0.23, a 7.7% error.

To eliminate the error caused by camera offset, the offset value for the camera used in each experiment (i.e., 5 for the Sony camera) was added to all nonzero intensities in each image. The offset was also added to the intensities in the titration reference chamber to correct the values of $(I_f)_{max}$ and I_{fo}. Note that the camera offset can also be positive, that is a finite intensity is recorded even for zero light. This problem can be corrected in the same manner by subtracting the offset value from each image. In fact, a positive offset may be desirable because it does not lose any intensity data, which negative offsets do (the portion of the curve where $I_f < 0$ in Figure B.6b).

Another way to eliminate offset problems is altering the camera hardware itself. Many cameras provide a pedestal level adjustment that changes the black level offset. This approach, however, was not employed in the present study.

APPENDIX C

Effects of Free Stream Speed on Wake Development

The differences between the development of wakes with free stream speeds of $U_0 = 10$ cm/s and $U_0 = 20$ cm/s have already been discussed. Likewise, how uncertainty in free stream speed can stretch or compress the nondimensional streamwise coordinate x* has been documented. This appendix will discuss exactly how changes in free stream speed affect wake development.

A series of experiments was performed with various wake free stream speeds. All other flow parameters were fixed throughout the experiments. Six different wake speeds were used ranging from $U_0 = 7.17$ cm/s to $U_0 = 11.56$ cm/s. Each case was forced identically with a frequency of 6 Hz and an amplitude representing 9% RMS of the free stream speed for a $U_0 = 10$ cm/s wake. Instantaneous chemically reacting LIF images for each of the six cases are presented in Figure C.1. The streamwise range in each image is x = 7.5 cm to x = 13.0 cm. Free stream speed clearly has a major impact on the development of the wake. At lower speed the wake is dominated by three-dimensionality (Figure C.1a-C.1c), at higher speed the flow is much less three-dimensional and narrower (Figure C.1d-C.1f).

Data calculated for the six cases are shown in Table C.1. δ_P, δ_1, and δ_P/δ_1 are given for each wake speed in addition to data normalized by the nominal case $U_0 = 9.94$ cm/s. These values are calculated as $\delta_P^* = \delta_P/(\delta_P)_{nom}$, $\delta_1^* = \delta_1/(\delta_1)_{nom}$, and $[\delta_P/\delta_1]^* = [\delta_P/\delta_1]/[\delta_P/\delta_1]_{nom}$. The lowest speed wake studied, $U_0 = 7.17$ cm/s, had 2.33 times as much normalized product as the nominal case. In contrast, the highest speed cases, $U_0 = 11.54$ cm/s and $U_0 = 11.56$ cm/s, had only 58% and 71% as much product as the nominal case.

Table C.1. Calculated data for various wake free stream speeds.

U_0 (cm/s)	U_1/U_2	δ_P (cm)	δ_1 (cm)	δ_P^*	δ_1^*	$[\delta_P/\delta_1]^*$
7.17	1.01	0.549	3.19	2.95	1.27	2.33
8.50	0.96	0.461	2.86	2.47	1.13	2.18
8.77	0.98	0.463	2.85	2.49	1.13	2.20
9.94	1.01	0.186	2.52	-----	-----	-----
11.54	0.98	0.101	2.34	0.54	0.93	0.58
11.56	1.13	0.128	2.42	0.69	0.96	0.71

The discrepancy in the two highest speed cases is most likely due to their differences in velocity ratio U_1/U_2 as shown in the second column of Table C.1. Ideally, a wake is achieved when $U_1/U_2 = 1$. With the exception of one case, the velocity ratios are within ±4% of the ideal wake condition. The last case shown (U_0 = 11.56 cm/s) has free stream velocities of $U_1 = 12.24$ cm/s and $U_2 = 10.88$ cm/s resulting in a velocity ratio $U_1/U_2 = 1.13$. This case is better classified as a shear layer and results in a 23% increase in normalized product thickness compared to a wake with nearly identical flow speed (U_0 = 11.54 cm/s). Interestingly, although the shear layer contains significantly more product than the wake, the two flows have very similar structures (see Figures C.1e and f). Besides these two cases the effect of the velocity ratio was not systematically studied. In the experiments in this report the velocity ratio was kept in the range 0.95-1.05 and significant shear layer effects are not expected.

A plot of δ_P/δ_1 versus x for each case is shown in Figure C.2. The variation in the data between cases is reduced some by nondimensionalizing the x axis as $x^* = xf/U_o$, as illustrated in Figure C.3. Changing the free stream speed of the wake also changes the natural roll-up frequency and the forcing amplitude percentage. Thus, the data should not be expected to collapse perfectly.

In the low speed wake cases reported in the main body of this report the free stream speeds were set as accurately as possible. In each experiment these speeds were within 0.05 cm/s of the nominal value $U_o = 10$ cm/s. Therefore, variations in wake width and product due to speed differences should be negligible.

APPENDIX D

Predicting ξ_S

It is often convenient to know the approximate value of ξ_S before an experiment begins. Fortunately, ξ_S occurs very near neutralization (i.e., when the solution pH = 7). Thus, ξ_S can be predicted using basic chemistry.

D.1 Standard Method

Consider a fixed volume of acid v_A of molarity M_A being titrated with a base of molarity M_B. Initially, the number of moles of acid is given by $n_A = v_A M_A$. At neutralization n_A will be exactly balanced by the number of moles of base, that is $n_A - v_B M_B = 0$. Therefore, the volume of base v_B that must be titrated to neutralize the acid is given by $v_B = n_A / M_B$ and ξ_S can be found as $\xi_S = v_B / (v_A + v_B)$.

D.2 Additional Concerns

This method works if the acid has only one hydrogen ion (e.g., HCl). In the present investigation, H_2SO_4 was used. The second hydrogen ion in sulfuric acid also partially dissociates in the reaction $HSO_4^- \rightleftharpoons H^+ + SO_4^{2-}$.

The general expression for the dissociation constant for this reaction is

$$K_a = \frac{[H^+][SO_4^{2-}]}{[HSO_4^-]} = 0.012 \tag{D.1}$$

The dissociation equation can be rewritten in terms of the acid molarity M_A as

$$K_a = \frac{(M_A + \zeta)\zeta}{M_A - \zeta} = 0.012 \tag{D.2}$$

where ζ indicates the change in molarity due to the reaction.

Now, let $M^* = K_a / M_A$. Equation D.2 can be rewritten as

$$(\zeta + M_A) = M_A\left[\frac{1 + \sqrt{(1 + M^*)^2 + 4M^*} - (1 + M^*)}{2}\right] \tag{D.3}$$

The partial dissociation of the second hydrogen ion can now be accounted for by replacing M_A with the expression above for $(\zeta + M_A)$ in §D.1.

APPENDIX E

Line Plots of $\overline{C_P^*}(y)$

Conventional line plots containing a subset of the data in Figures 57-58, the time-averaged spanwise images, are presented in Figures E.1-E.4. These plots show the transverse (y) $\overline{C_P^*}$ profiles of the wake at each streamwise (x) position studied for five spanwise positions on the positive z side of the test section. Profiles from the negative z side are expected to be similar due to symmetry.

Similar line plots for the higher speed wake are provided in Figure E.5. Data in these plots are a subset of the data in Figure 80. $\overline{C_P^*}$ Profiles at each streamwise position are given for a total of five spanwise positions. At x = 16 cm, the unforced profiles are shown as dashed lines.

APPENDIX F

Effects of Three-Dimensionality

The 'tipping' of spanwise vortices in the side walls' boundary layers was first noted by Roberts (1985). He observed regions of three-dimensionality in a forced wake that resulted in strong mixing. Photographs of the wake in plan view showed that this three-dimensionality was the result of the spanwise vortices being stretched and reoriented in the sheared regions near the test section side walls. A single spanwise image confirmed that the regions of three-dimensionality were, in fact, pairs of counterrotating streamwise vortices. Later, Koochesfahani & MacKinnon (1993) studied the effects of this three-dimensionality more extensively. Like Roberts, they found that the streamwise vortices tend to convect away from the side walls as the wake moves downstream. In addition, their images show the three-dimensionality is more pronounced at high amplitude forcing. This causes the streamwise structures to convect toward the middle of the test section more quickly.

Similar results were found in the present work. For high amplitude forcing, the regions of three-dimensionality move away from the side walls very quickly. This can be seen in both spanwise flow images (Figures 37-56) and in the plots of measured product thickness (Figures 59b-63b). The peak values of δ_P are at the regions of strongest mixing and, hence, within the regions of streamwise vorticity. Because of this, the streamwise evolution of the three-dimensionality can be tracked by plotting the spanwise (z) location of the δ_p maxima z_{peak} as a function of x. This has been done for the wake forced at 5% and 9% amplitude in Figure F.1. Notice that z_{peak}, hence three-dimensionality, convects away from the side walls more quickly for the 9% amplitude case. The three-dimensionality propagation velocity V_{peak} can be found using

$$V_{peak} = \frac{d}{dx}(z_{peak})\,U_o \tag{F.1}$$

Figure F.2 is a plot of V_{peak} versus x. The streamwise vortices move away from the side walls fairly quickly at first, but begin to slow as they move downstream.

This behavior seen in Figures F.1 and F.2 is exactly what is expected. The three-dimensionality initially moves away from the side walls due to the velocity induced by the streamwise vortices, shown in Figure F.3a. As the three-dimensionality moves toward the center of the test section, though, V_{peak} decreases due to the opposite-signed vortices associated with the other side wall, as illustrated in Figure F.3b. The model shown in Figure F.3 was originally proposed by Roberts (1985). Thus, the data in Figures F.1 and F.2 quantitatively support Roberts' hypothesis.

LIST OF REFERENCES

LIST OF REFERENCES

Bernal, L. P. (1981), "The coherent structure of turbulent mixing layers," Ph.D. Thesis, California Institute of Technology.

Bernal, L. P. and Roshko, A. (1986), "Streamwise vortex structure in plane mixing layers," *Journal of Fluid Mechanics,* Vol. 170, pp. 499-525.

Bradshaw, P. (1966), "The effect of initial conditions on the development of a free shear layer," *Journal of Fluid Mechanics,* Vol. 26, pp. 225-236.

Breidenthal, R. E. (1978), "A chemically reacting turbulent shear layer," Ph.D. Thesis, California Institute of Technology.

Breidenthal, R. (1981), "Structure in turbulent mixing layers and wakes using a chemical reaction," *Journal of Fluid Mechanics,* Vol. 109, pp. 1-24.

Browand, F. K. and Troutt, T. R. (1980), "A note on the spanwise structure in the two-dimensional mixing layer," *Journal of Fluid Mechanics,* Vol. 97, pp. 771-781.

Browand, F. K. and Troutt, T. R. (1985), "The turbulent mixing layer: geometry of large vortices," *Journal of Fluid Mechanics,* Vol. 158, pp. 489-509.

Brown, G. L. and Roshko, A. (1971), "The effect of density difference on the turbulent mixing layer," *Turbulent Shear Flows; AGARD-CP-93,* pp. 1-12.

Brown, G. L. and Roshko, A. (1974), "On density effects and large structure in turbulent mixing layers," *Journal of Fluid Mechanics,* Vol. 64, pp. 775-816.

Cimbala, J. M., Nagib, H. M., and Roshko, A. (1988), "Large structure in the far wakes of two-dimensional bluff bodies," *Journal of Fluid Mechanics,* Vol. 190, pp. 265-298.

Dimotakis, P. E. and Brown, G. L. (1976), "The mixing layer at high Reynolds number; large-structure dynamics and entrainment," *Journal of Fluid Mechanics,* Vol. 78, pp. 535-560.

Grant, M. L. (1958), "The large eddies of turbulent motion," *Journal of Fluid Mechanics,* Vol. 4, pp. 149-190.

Hayakawa, M. and Hussain, F. (1989), "Three-dimensionality of organized structures in a plane turbulent wake," *Journal of Fluid Mechanics*, Vol. 206, pp. 375-404.

Ho, C-M. and Huang, L-S. (1982), "Subharmonics and vortex merging in mixing layers," *Journal of Fluid Mechanics*, Vol. 119, pp. 443-473.

Katch, G. J. (1994), "Mixing of species in a two-stream shear layer forced by an oscillating airfoil," MS Thesis, Michigan State University.

Konrad, J. H. (1976), "An experimental investigation of mixing in two-dimensional turbulent shear flows with applications to diffusion-limited chemical reactions," Ph.D. Thesis, California Institute of Technology.

Koochesfahani, M. M. (1984), "Experiments on turbulent mixing and chemical reactions in a liquid mixing layer," Ph.D. Thesis, California Institute of Technology.

Koochesfahani, M. M. and Dimotakis, P. E. (1985), "Laser-induced fluorescence measurements of mixed fluid concentration in a liquid plane shear layer," *AIAA Journal*, Vol. 23, pp. 1700-1707.

Koochesfahani, M. M. and Dimotakis, P. E. (1986), "Mixing and chemical reactions in a turbulent liquid mixing layer," *Journal of Fluid Mechanics*, Vol. 170, pp. 83-112.

Koochesfahani, M. M. and MacKinnon, C. G. (1991), "Influence of forcing on the composition of mixed fluid in a two-stream shear layer," *Physics of Fluids A*, Vol. 3, pp. 1135-1142.

Koop, C. G. and Browand, F. K. (1979), "Instability and turbulence in a stratified fluid with shear," *Journal of Fluid Mechanics*, Vol. 93, pp. 135-159.

Lasheras, J. C., Cho, J. S., and Maxworthy, T. (1986), "On the origin and evolution of streamwise vortical structures in a plane, free shear layer," *Journal of Fluid Mechanics*, Vol. 172, pp. 231-258.

Lasheras, J. C. and Choi, H. (1988), "Three-dimensional instability of a plane free shear layer: an experimental study of the formation and evolution of streamwise vortices," *Journal of Fluid Mechanics*, Vol. 189, pp. 53-86.

MacKinnon, C. G. and Koochesfahani, M. M. (1993), "Three-dimensional structure and mixing of a forced wake inside a confined channel," *AIAA 93-0658*.

Meiburg, E. and Lasheras, J. C. (1988), "Experimental and numerical investigation of the three-dimensional transition in plane-wakes," *Journal of Fluid Mechanics*, Vol. 190, pp. 1-37.

Miksad, R. W. (1972), "Experiments on the nonlinear stages of free-shear-layer transition," *Journal of Fluid Mechanics,* Vol. 56, pp. 695-719.

Morkovin, M. V. (1964), "Flow around circular cylinders—a kaleidoscope of challenging fluid phenomena," *ASME Symposium on Fully Separated Flows,* pp. 102-118.

Nygaard, K. J. and Glezer, A. (1991), "Evolution of streamwise vortices and generation of small-scale motion in a plane mixing layer," *Journal of Fluid Mechanics,* Vol. 231, pp. 257-301.

Oster, D. and Wygnanski, I. (1982), "The forced mixing layer between parallel streams," *Journal of Fluid Mechanics,* Vol. 123, pp. 91-130.

Roberts, F. A. (1985), "Effects of a periodic disturbance on structure and mixing in turbulent shear layers and wakes," Ph.D. Thesis, California Institute of Technology.

Roberts, F. A. and Roshko, A. (1985), "Effects of periodic forcing on mixing in turbulent shear layers and wakes," *AIAA-85-0570.*

Roshko, A. (1954), "On the development of turbulent wakes from vortex streets," *NACA Report 1191.*

Taneda, S. (1959), "Downstream development of the wakes behind cylinders," *Journal of the Physical Society of Japan*, Vol. 14, pp. 843-848.

Townsend, A. A. (1956), *Structure of Turbulent Shear Flow,* Cambridge University Press.

Weygandt, J. H. and Mehta, R. D. (1995), "Effects of streamwise vorticity injection on a plane turbulent wake," *AIAA Journal,* Vol. 33, pp. 86-93.

Williamson, C. H. K. (1992), "The natural and forced formation of spot-like 'vortex dislocations' in the transition of a wake," *Journal of Fluid Mechanics,* Vol. 243, pp. 393-441.

Winant, C. D. and Browand, F. K. (1974), "Vortex pairing: the mechanism of turbulent mixing layer growth at moderate Reynolds number," *Journal of Fluid Mechanics,* Vol. 63, pp. 237-255.

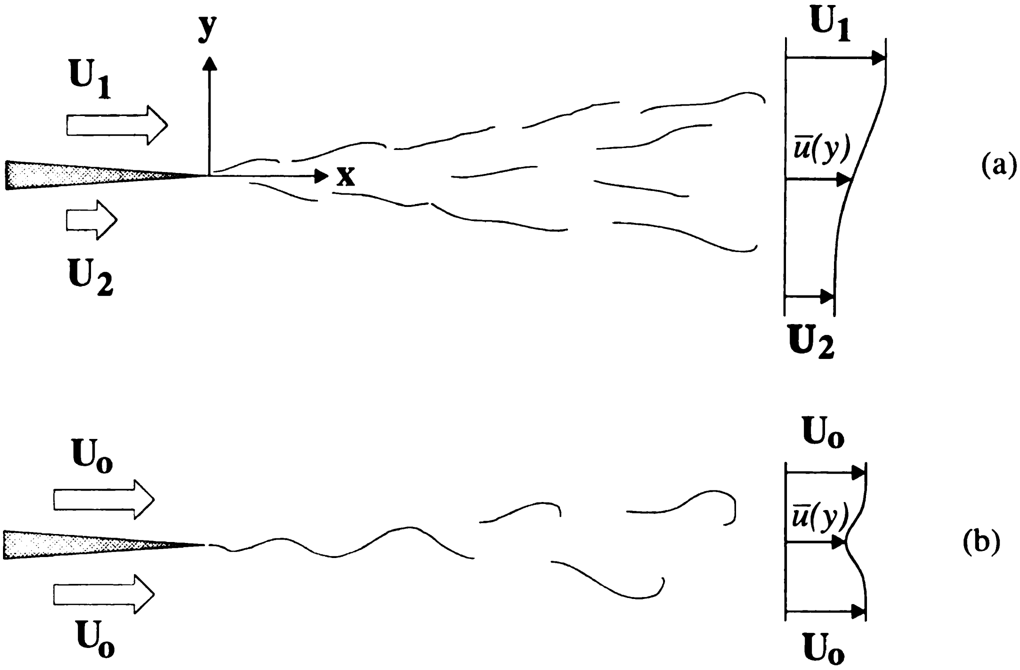

Figure 1. (a) Geometry of a shear layer. (b) Geometry of a wake.

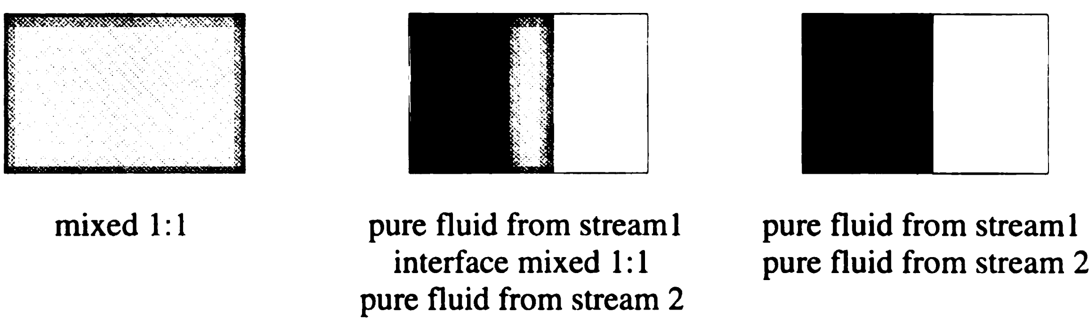

Figure 2. Examples illustrating the resolution problem of nonreacting LIF. All three cases would be considered uniformly mixed at 1:1.

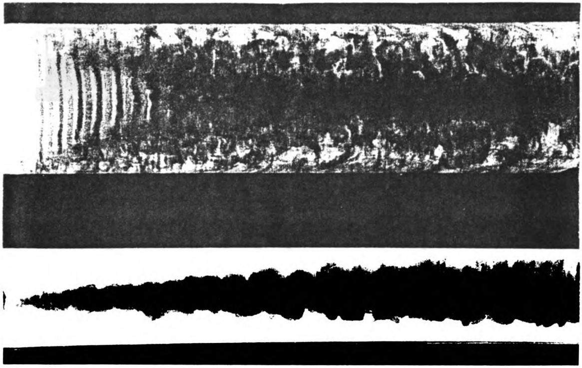

Figure 3. Simultaneous plan and side views of the highly mixed wake (Roberts, 1985).

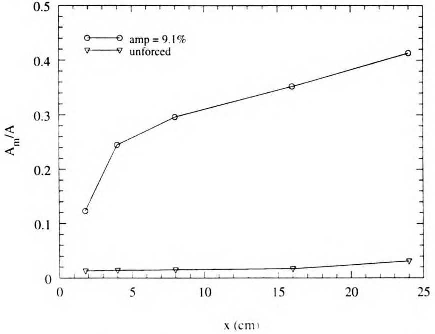

Figure 4. Downstream evolution of the mixed-fluid fraction (MacKinnon & Koochesfahani, 1993).

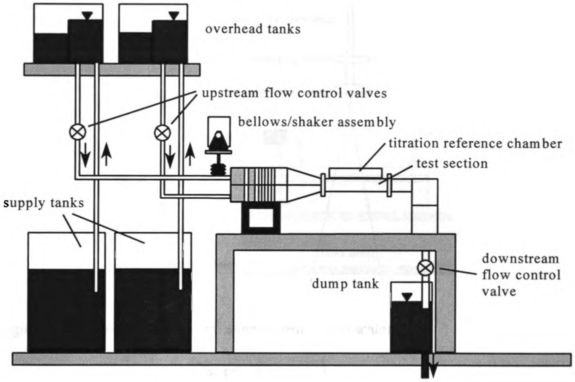

Figure 5. Schematic of the shear layer facility.

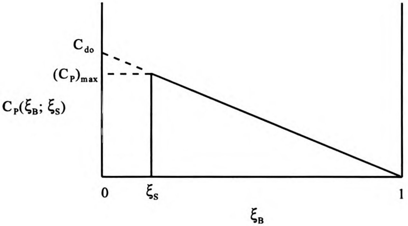

Figure 6. C_P versus ξ_B for a chemically reacting LIF experiment.

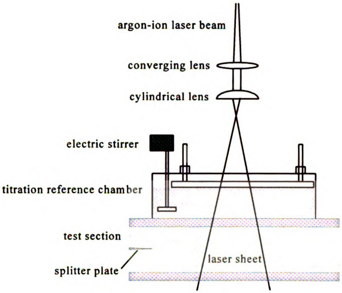

Figure 7. Schematic of the optical arrangement (not to scale).

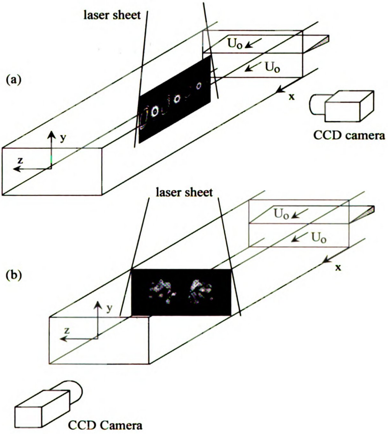

Figure 8. Setup for (a) streamwise and (b) spanwise imaging.

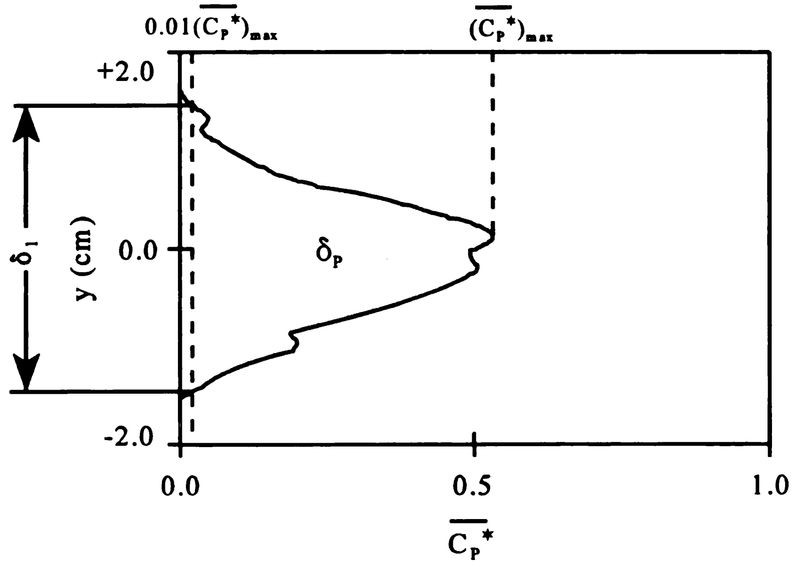

Figure 9. Graphical explanation of δ_P and δ_1.

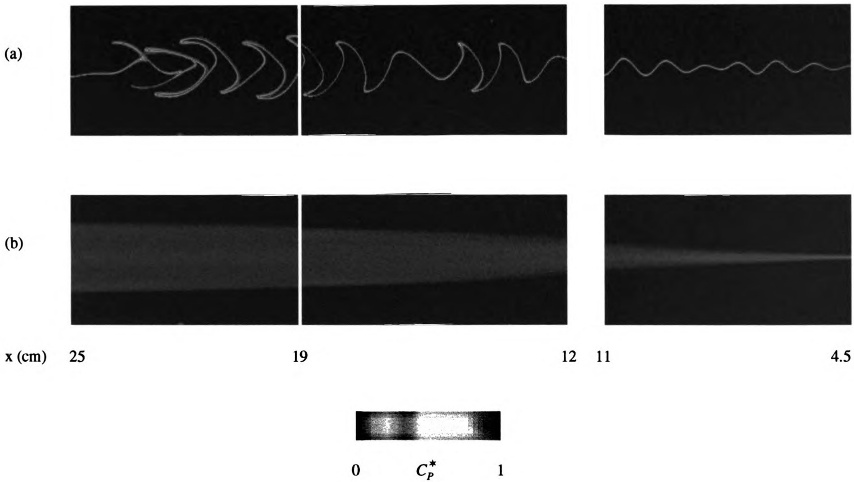

Figure 10. (a) Sample instantaneous and (b) average chemically reacting LIF images for the low speed unforced wake at z = 0.0 cm.

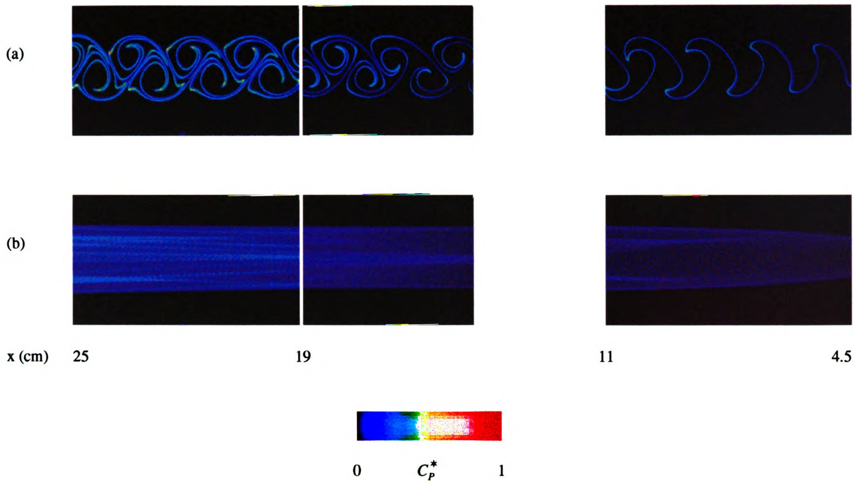

Figure 11. (a) Sample instantaneous and (b) average chemically reacting LIF images for the low speed wake forced at 2%. z = 0.0 cm.

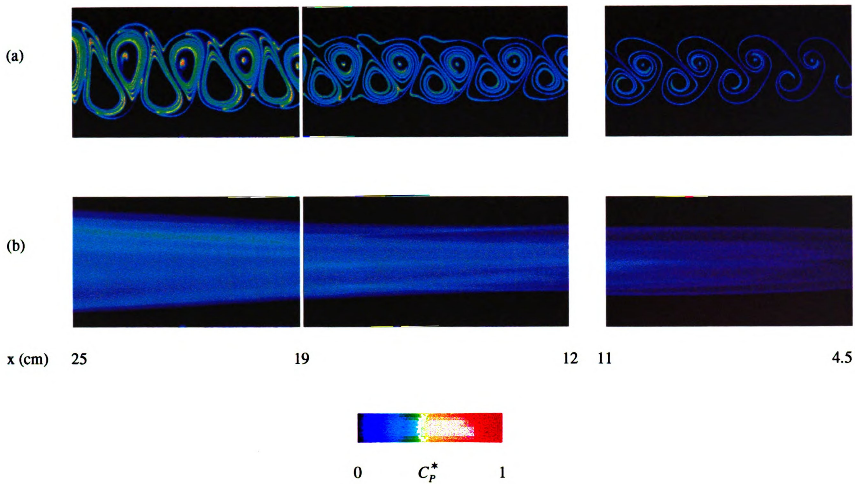

Figure 12. (a) Sample instantaneous and (b) average chemically reacting LIF images for the low speed wake forced at 5%. z = 0.0 cm.

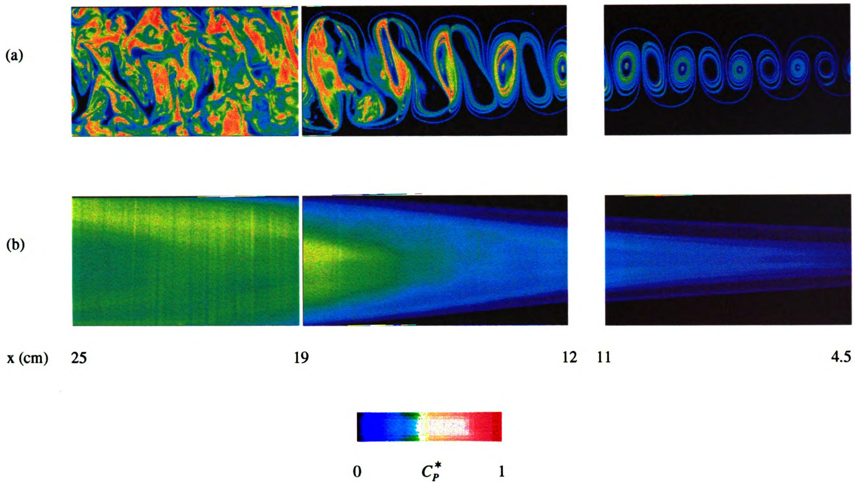

Figure 13. (a) Sample instantaneous and (b) average chemically reacting LIF images for the low speed wake forced at 9%. z = 0.0 cm.

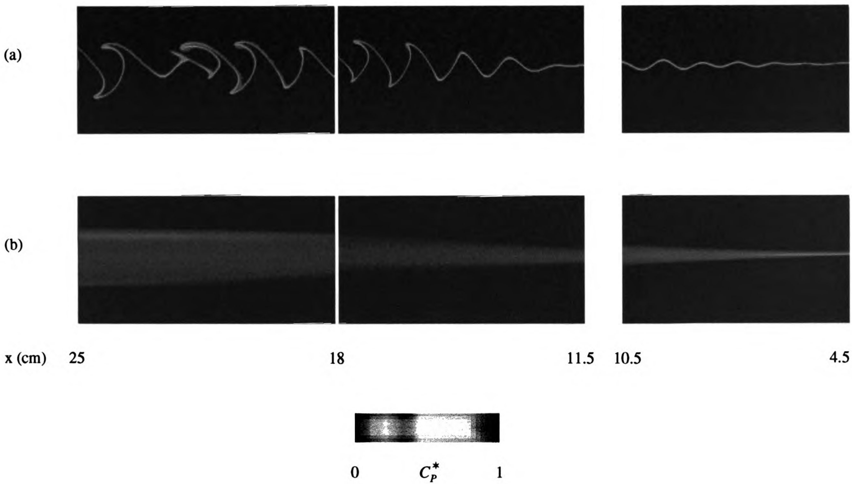

Figure 14. (a) Sample instantaneous and (b) average chemically reacting LIF images for the low speed unforced wake at z = +0.8 cm.

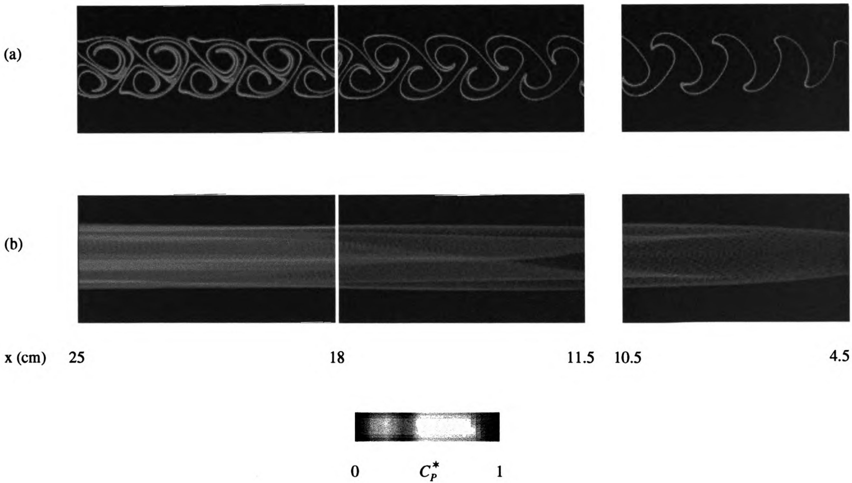

Figure 15. (a) Sample instantaneous and (b) average chemically reacting LIF images for the low speed wake forced at 2%. z = +0.8 cm.

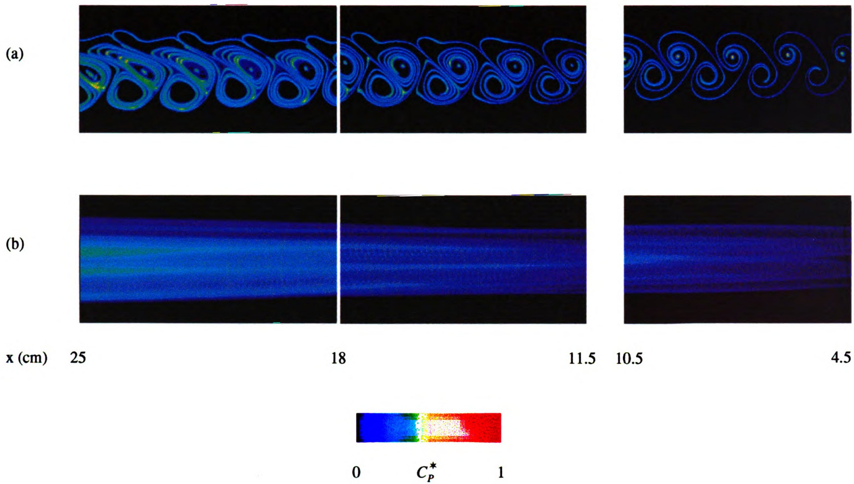

Figure 16. (a) Sample instantaneous and (b) average chemically reacting LIF images for the low speed wake forced at 5%. z = +0.8 cm.

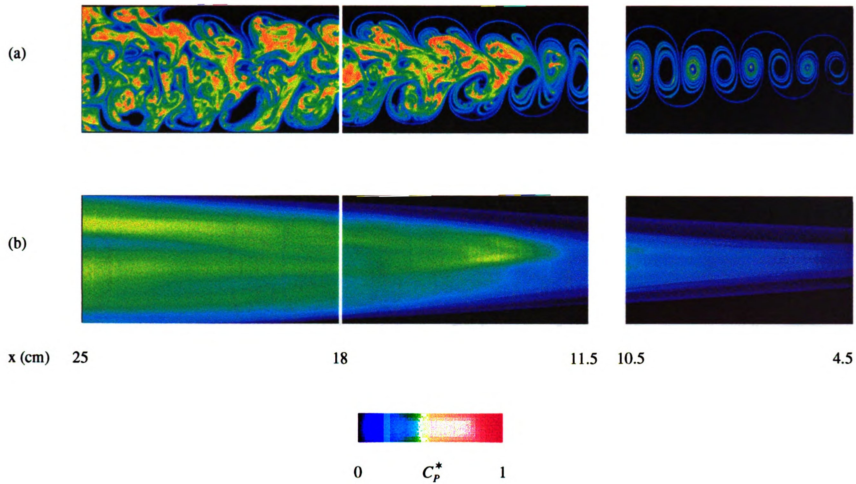

Figure 17. (a) Sample instantaneous and (b) average chemically reacting LIF images for the low speed wake forced at 9%. z = +0.8 cm.

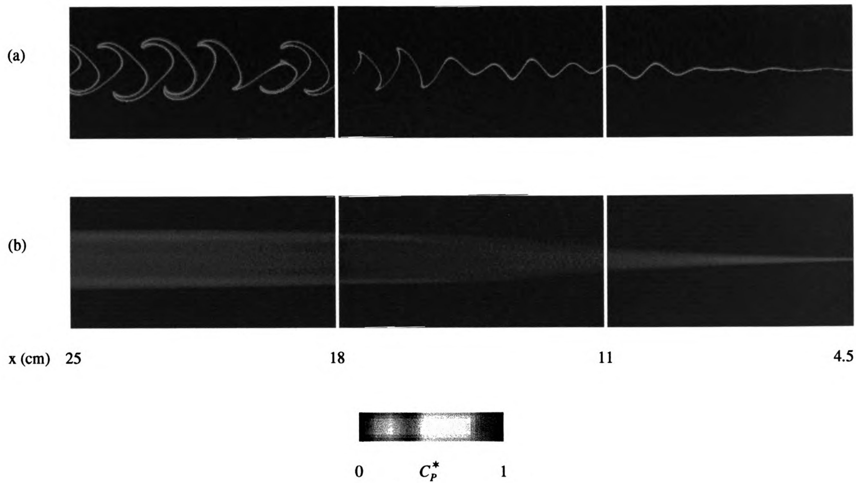

Figure 18. (a) Sample instantaneous and (b) average chemically reacting LIF images for the low speed unforced wake at z = -0.8 cm.

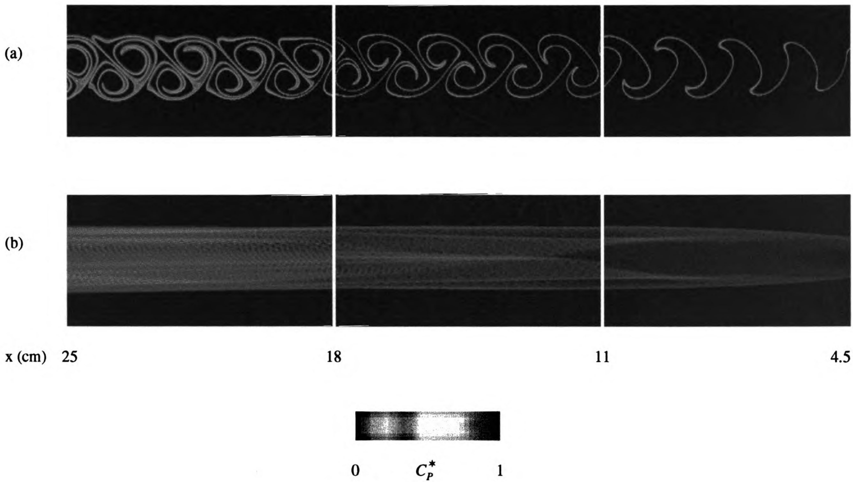

Figure 19. (a) Sample instantaneous and (b) average chemically reacting LIF images for the low speed wake forced at 2%. z = -0.8 cm.

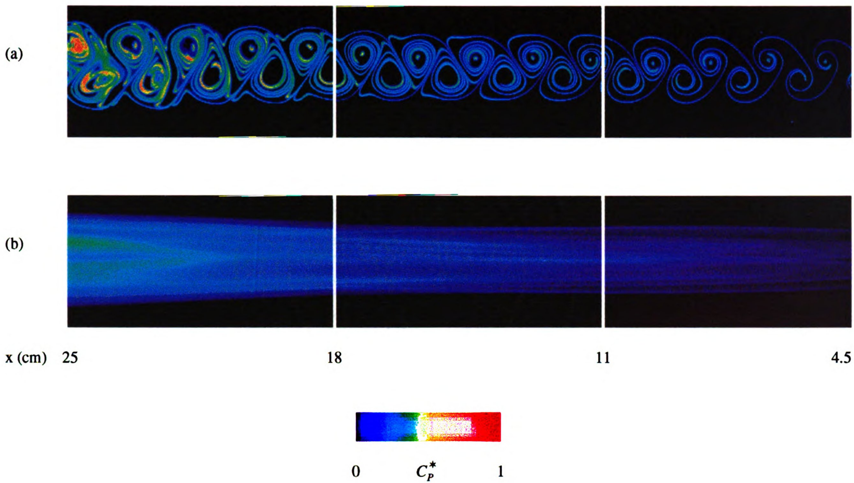

Figure 20. (a) Sample instantaneous and (b) average chemically reacting LIF images for the low speed wake forced at 5%. z = -0.8 cm.

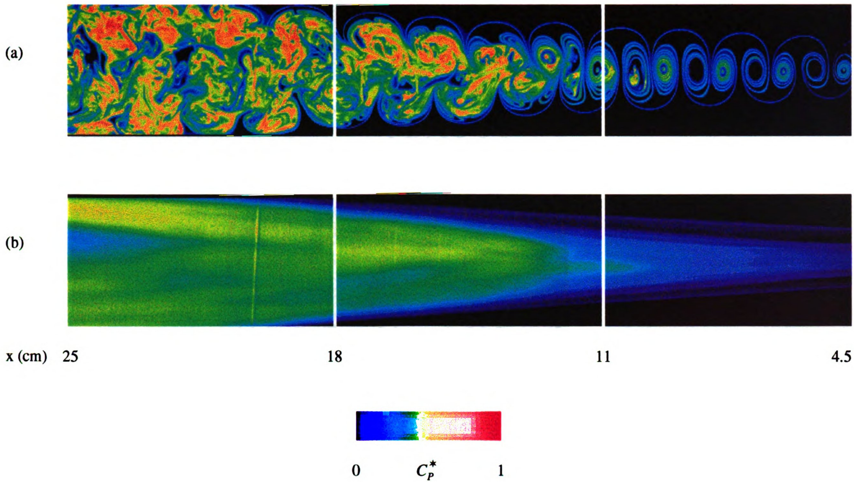

Figure 21. (a) Sample instantaneous and (b) average chemically reacting LIF images for the low speed wake forced at 9%. z = -0.8 cm.

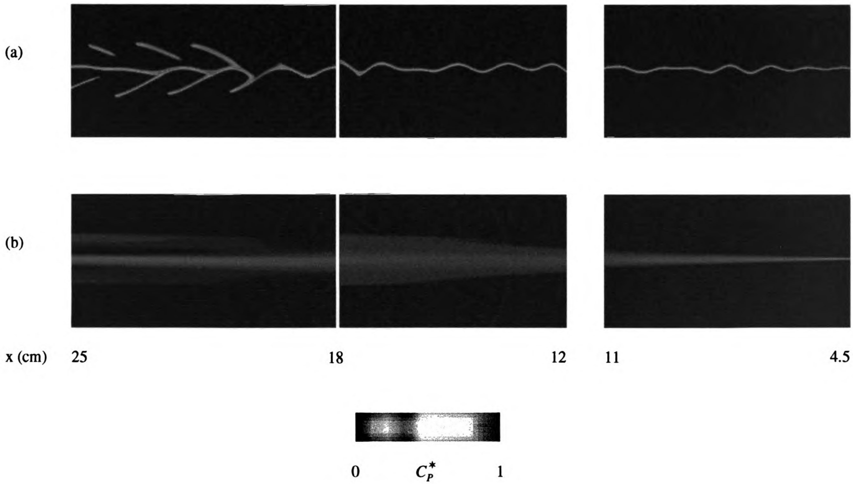

Figure 22. (a) Sample instantaneous and (b) average chemically reacting LIF images for the low speed unforced wake at $z = -2.0$ cm.

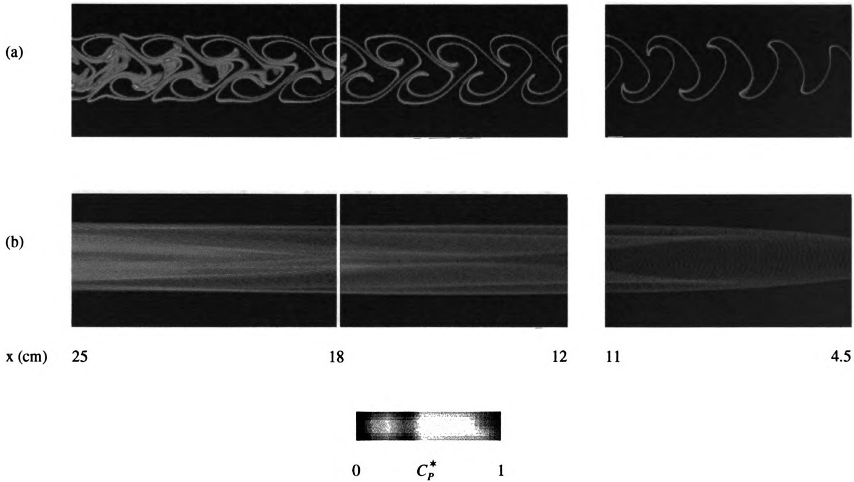

Figure 23. (a) Sample instantaneous and (b) average chemically reacting LIF images for the low speed wake forced at 2%. z = -2.0 cm.

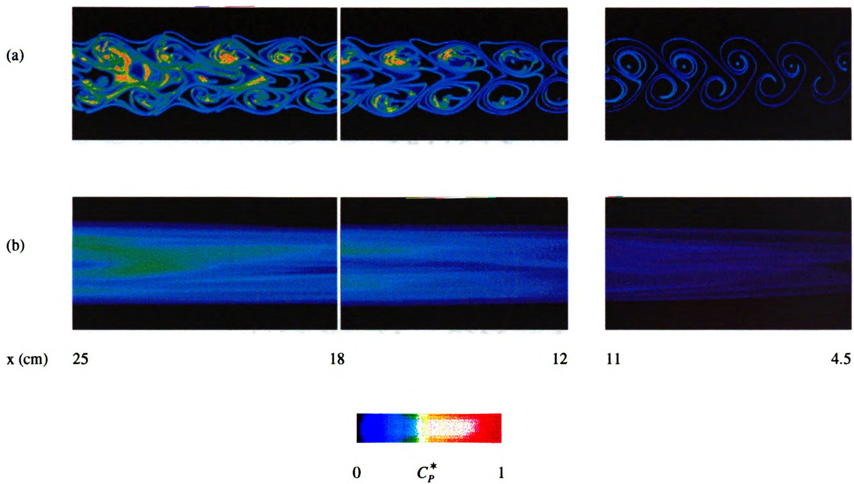

Figure 24. (a) Sample instantaneous and (b) average chemically reacting LIF images for the low speed wake forced at 5%. z = -2.0 cm.

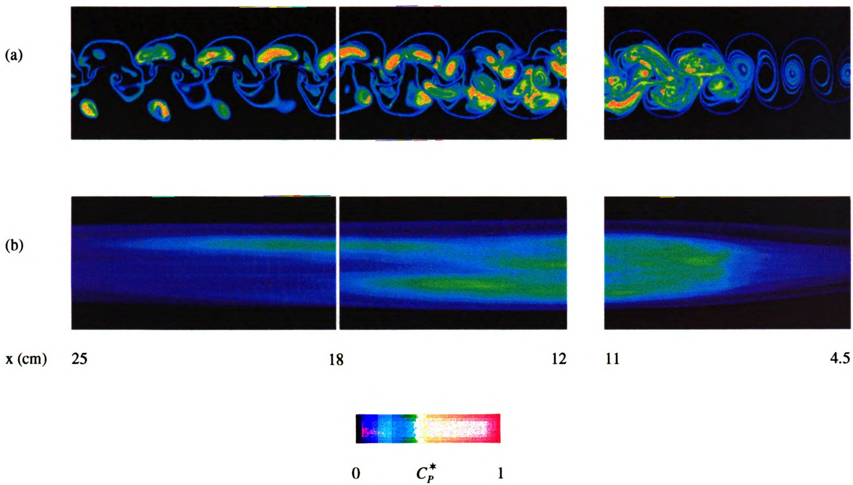

Figure 25. (a) Sample instantaneous and (b) average chemically reacting LIF images for the low speed wake forced at 9%. z = -2.0 cm.

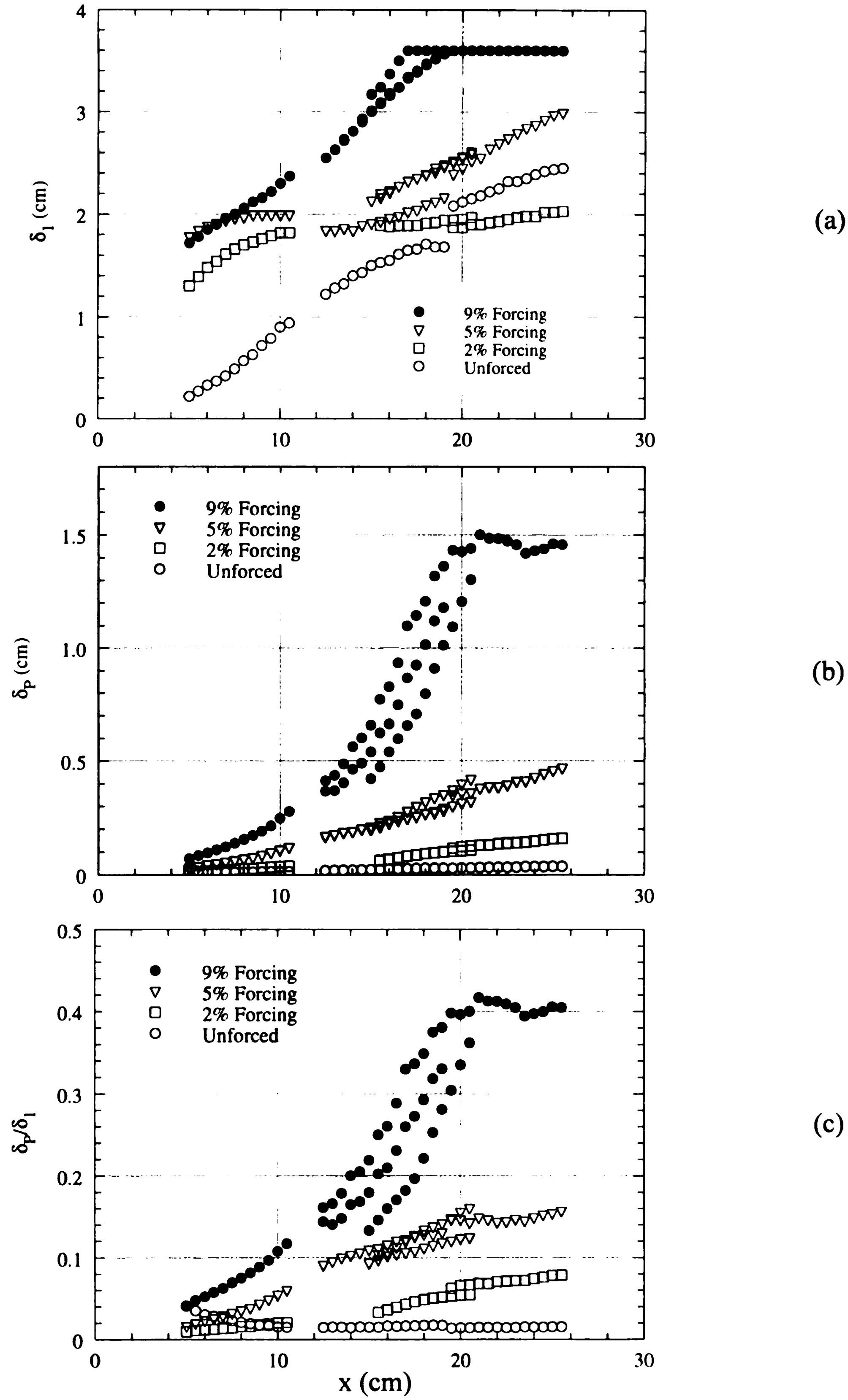

Figure 26. Calculated quantities versus x at z = 0.0 cm. (a) δ_1, (b) δ_P, (c) δ_P/δ_1.

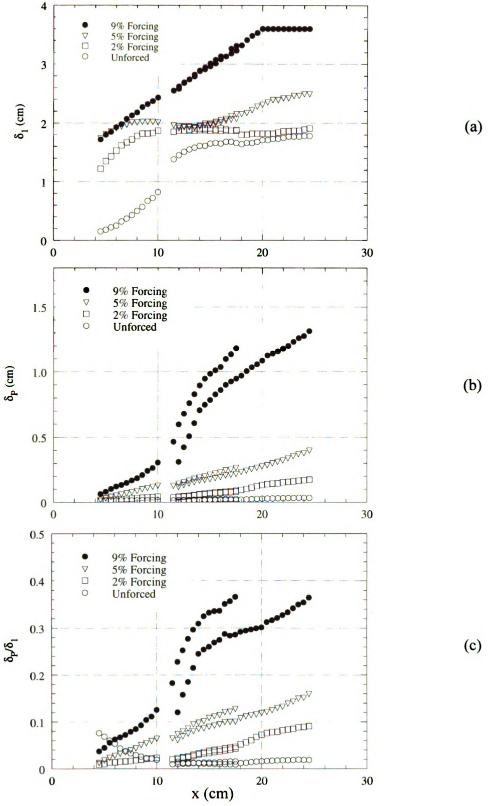

Figure 27. Calculated quantities versus x at z = +0.8 cm. (a) δ_1, (b) δ_P, (c) δ_P/δ_1.

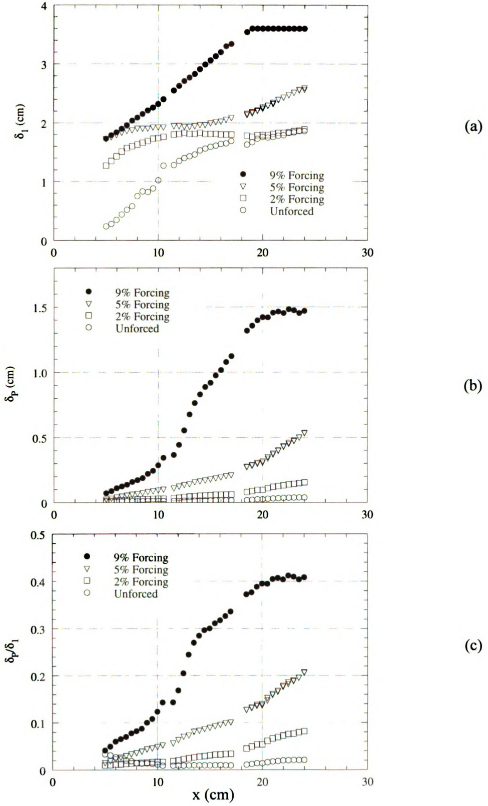

Figure 28. Calculated quantities versus x at z = -0.8 cm. (a) δ_1, (b) δ_P, (c) δ_P/δ_1.

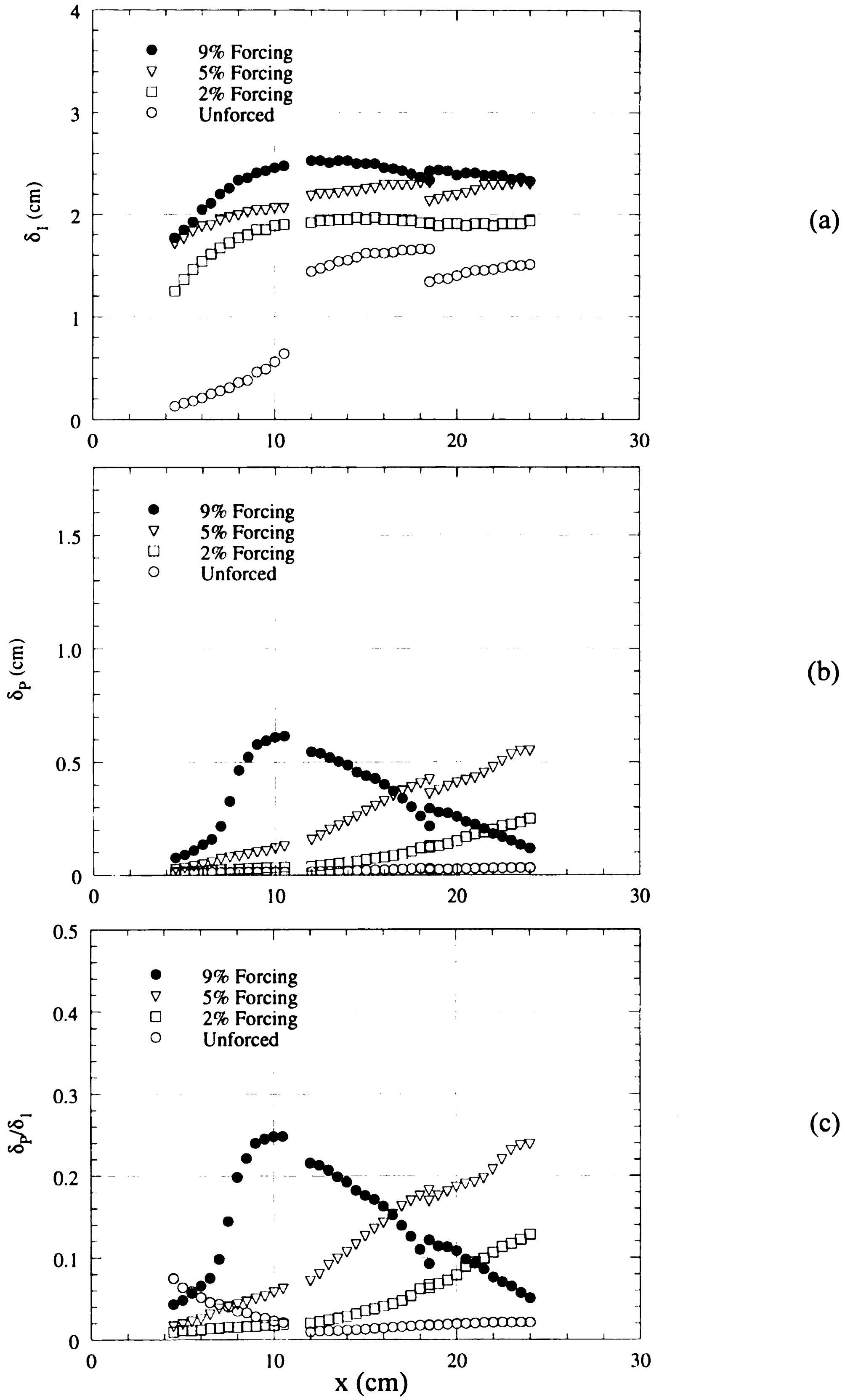

Figure 29. Calculated quantities versus x at z = -2.0 cm. (a) δ_1, (b) δ_P, (c) δ_P/δ_1.

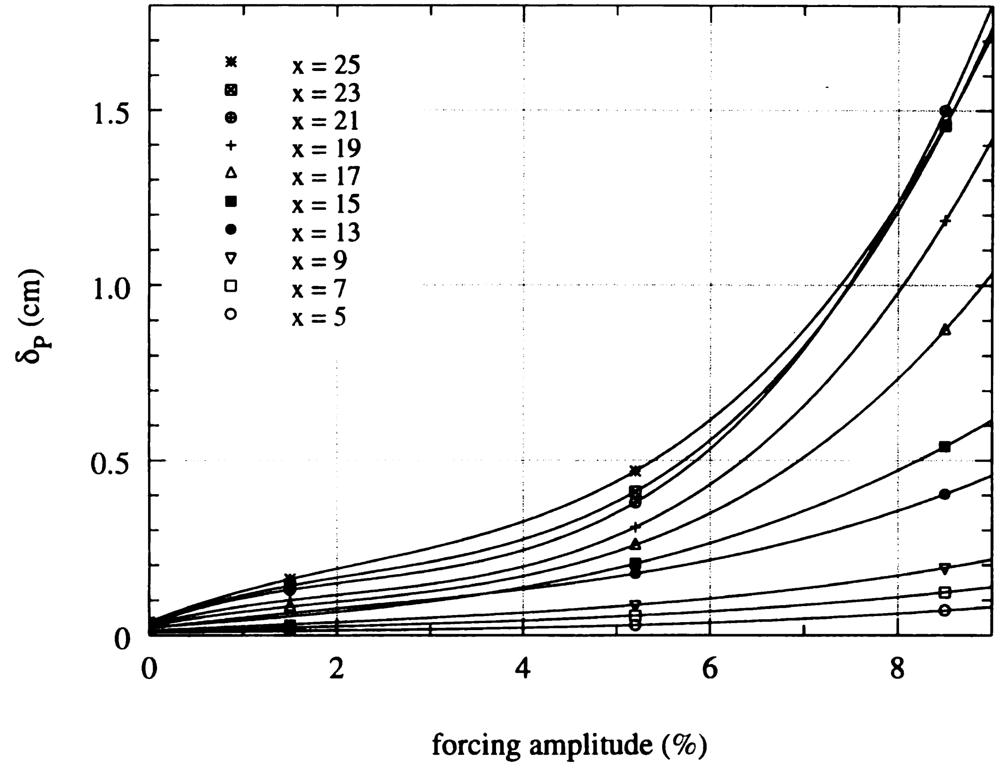

Figure 30. δ_P versus forcing amplitude for various x at midspan (z = 0.0 cm).

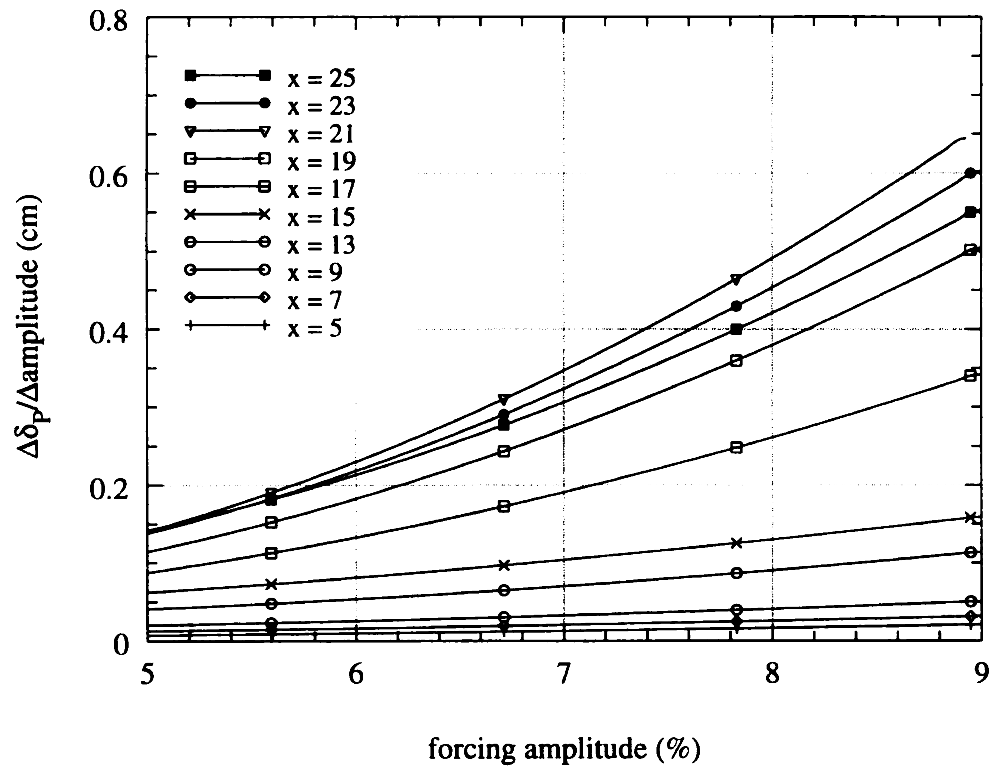

Figure 31. $\Delta\delta_P/\Delta$amplitude versus forcing amplitude for various x at midspan (z = 0.0 cm).

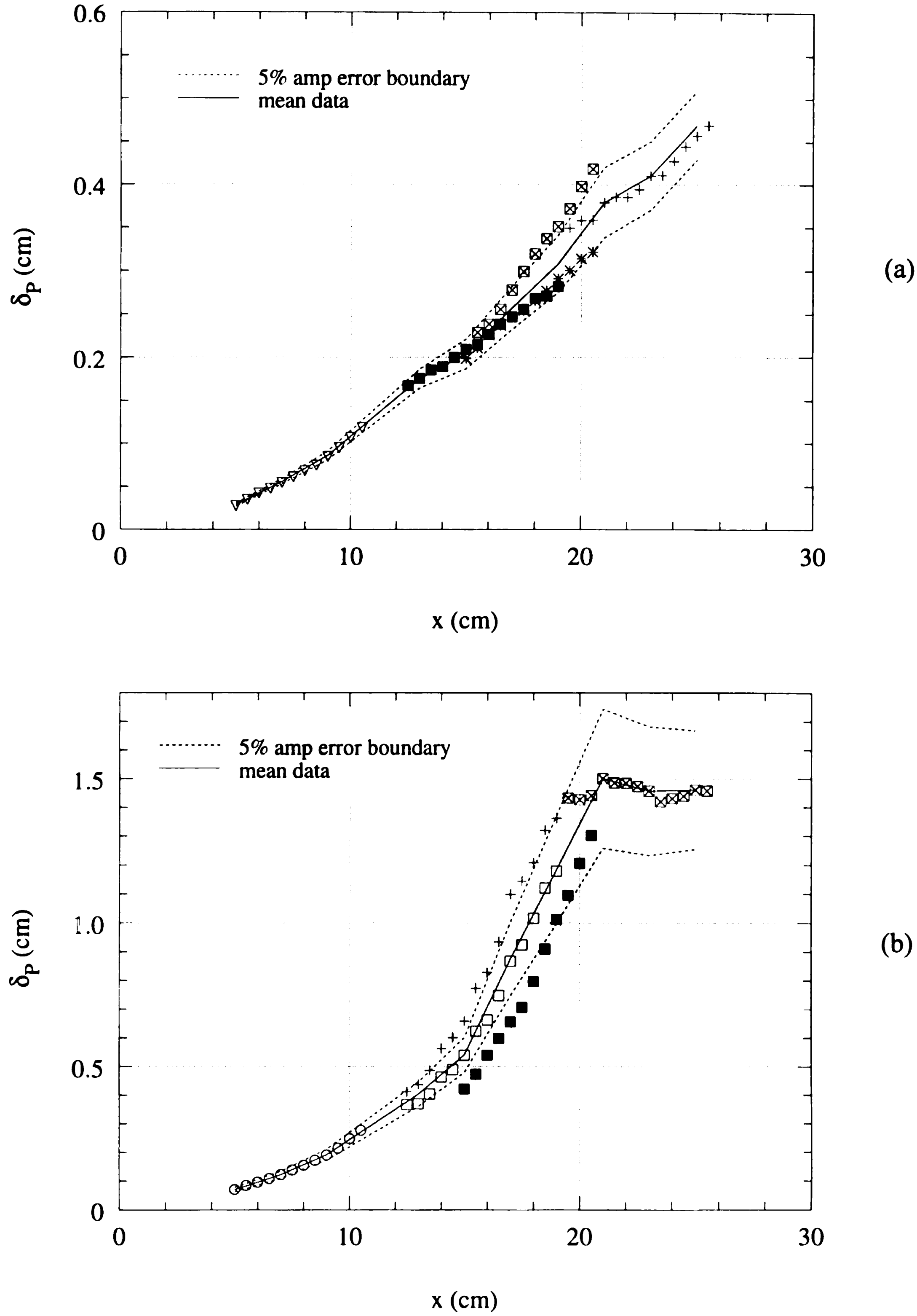

Figure 32. Mean δ_P versus x and 5% amplitude error boundaries at z = 0.0 cm for (a) 5% and (b) 9% forcing amplitude. Symbols indicate experimental data points.

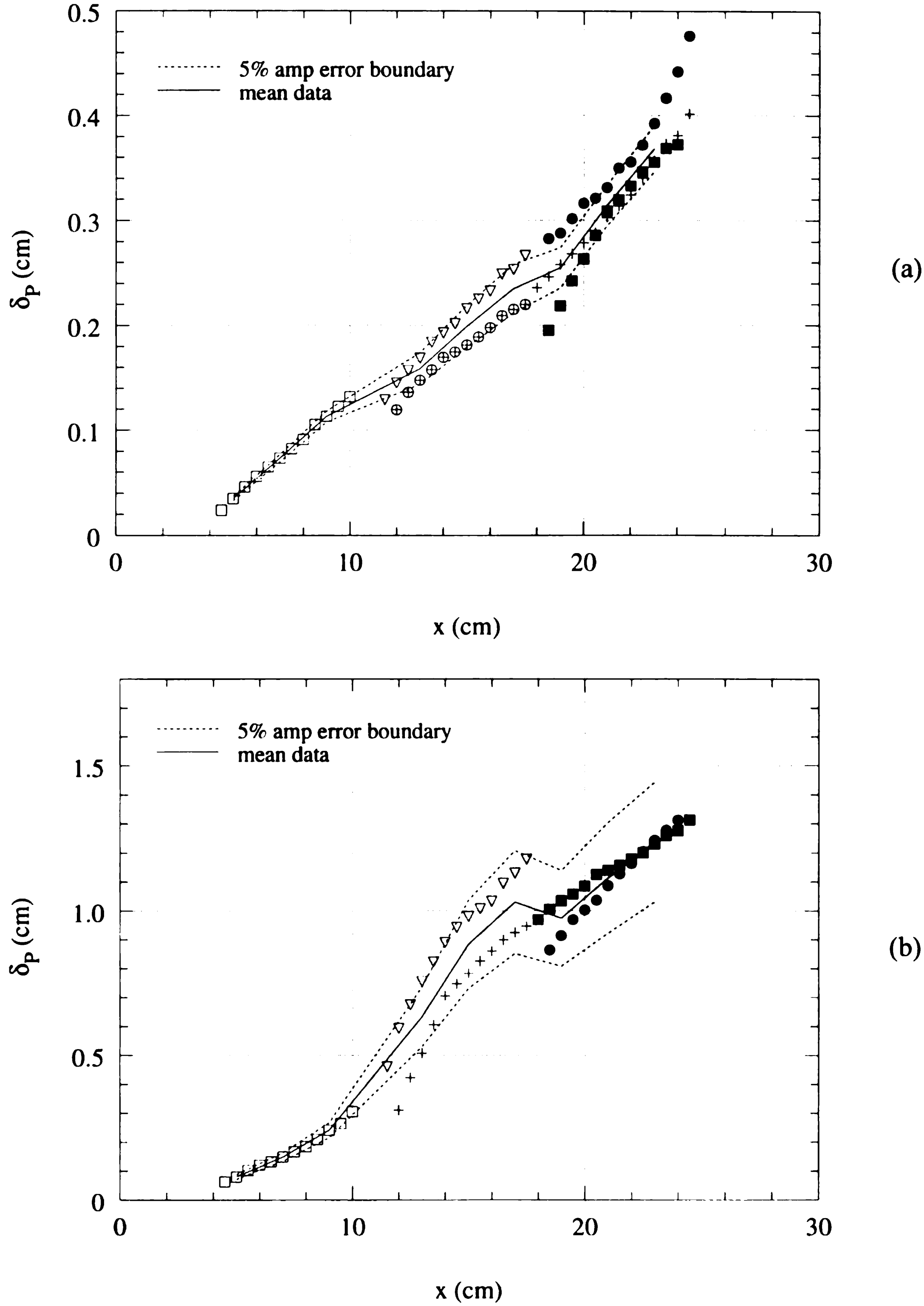

Figure 33. Mean δ_P versus x and 5% amplitude error boundaries at z = +0.8 cm for (a) 5% and (b) 9% forcing amplitude. Symbols indicate experimental data points.

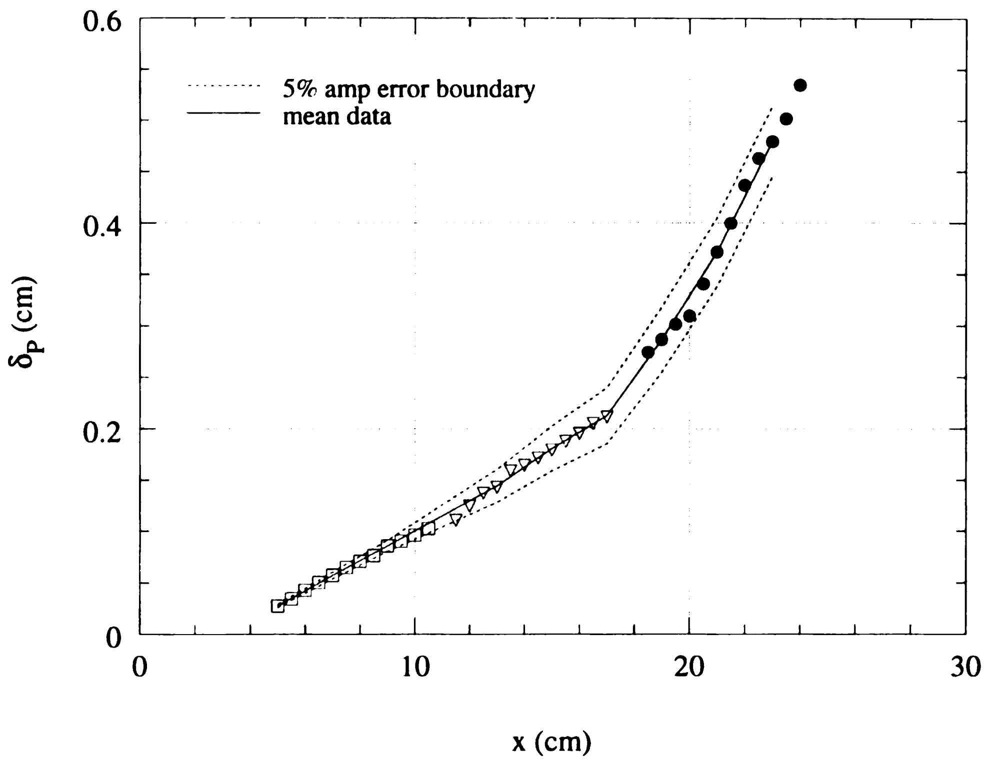

(a)

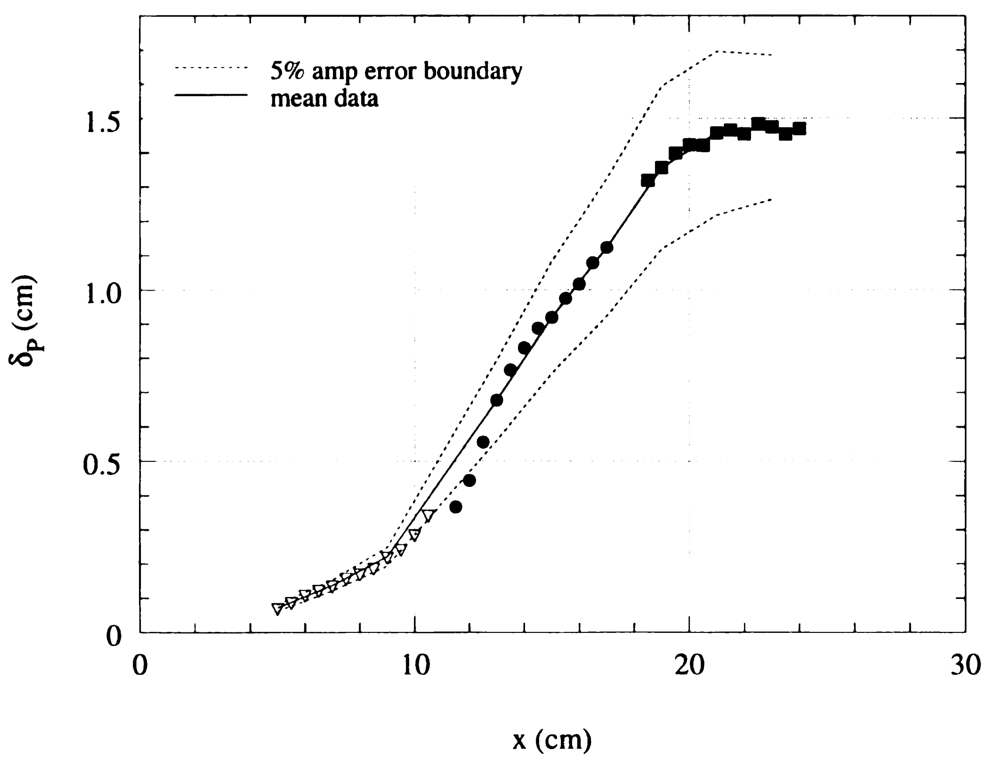

(b)

Figure 34. Mean δ_P versus x and 5% amplitude error boundaries at z = -0.8 cm for (a) 5% and (b) 9% forcing amplitude. Symbols indicate experimental data points.

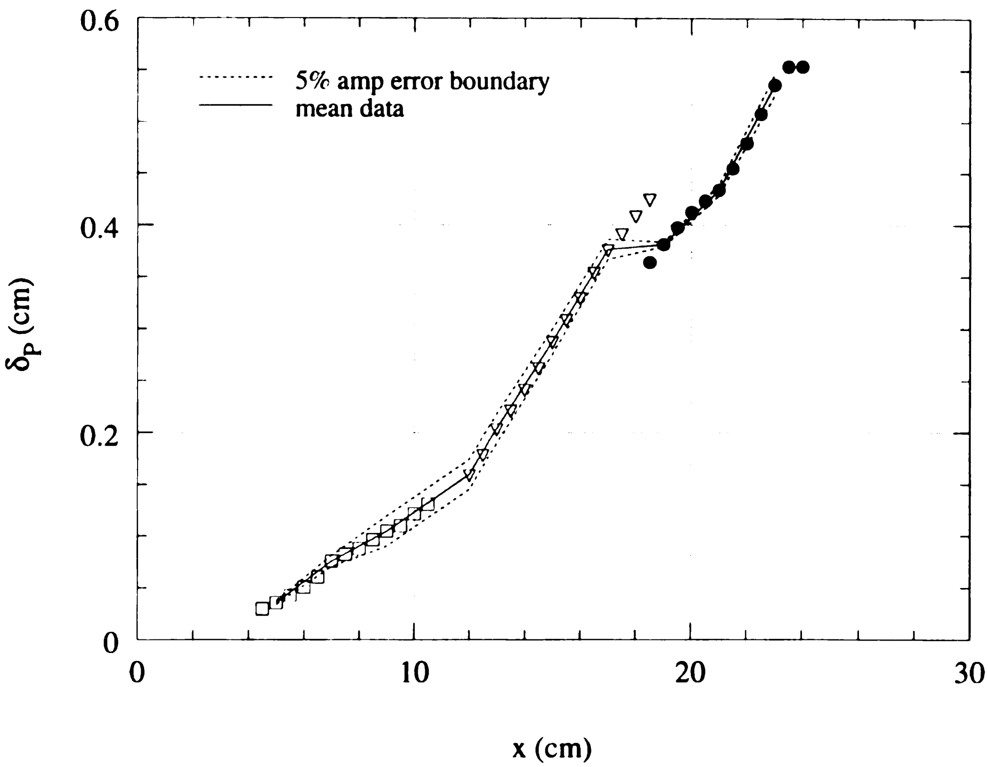

(a)

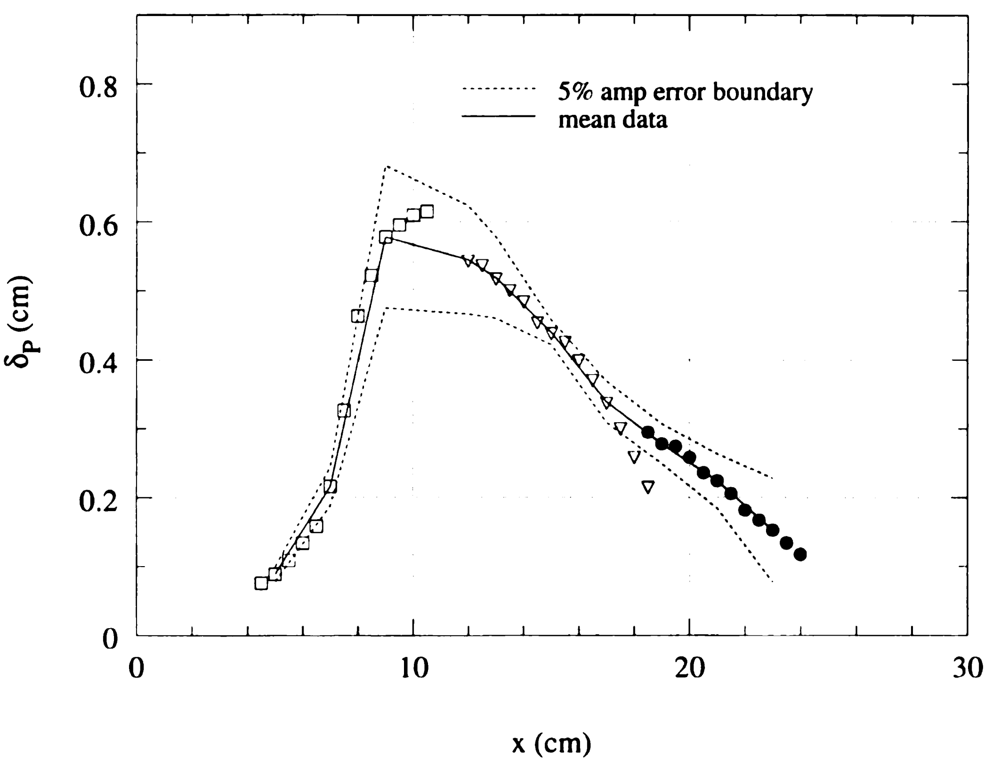

(b)

Figure 35. Mean δ_P versus x and 5% amplitude error boundaries at z = -2.0 cm for (a) 5% and (b) 9% forcing amplitude. Symbols indicate experimental data points.

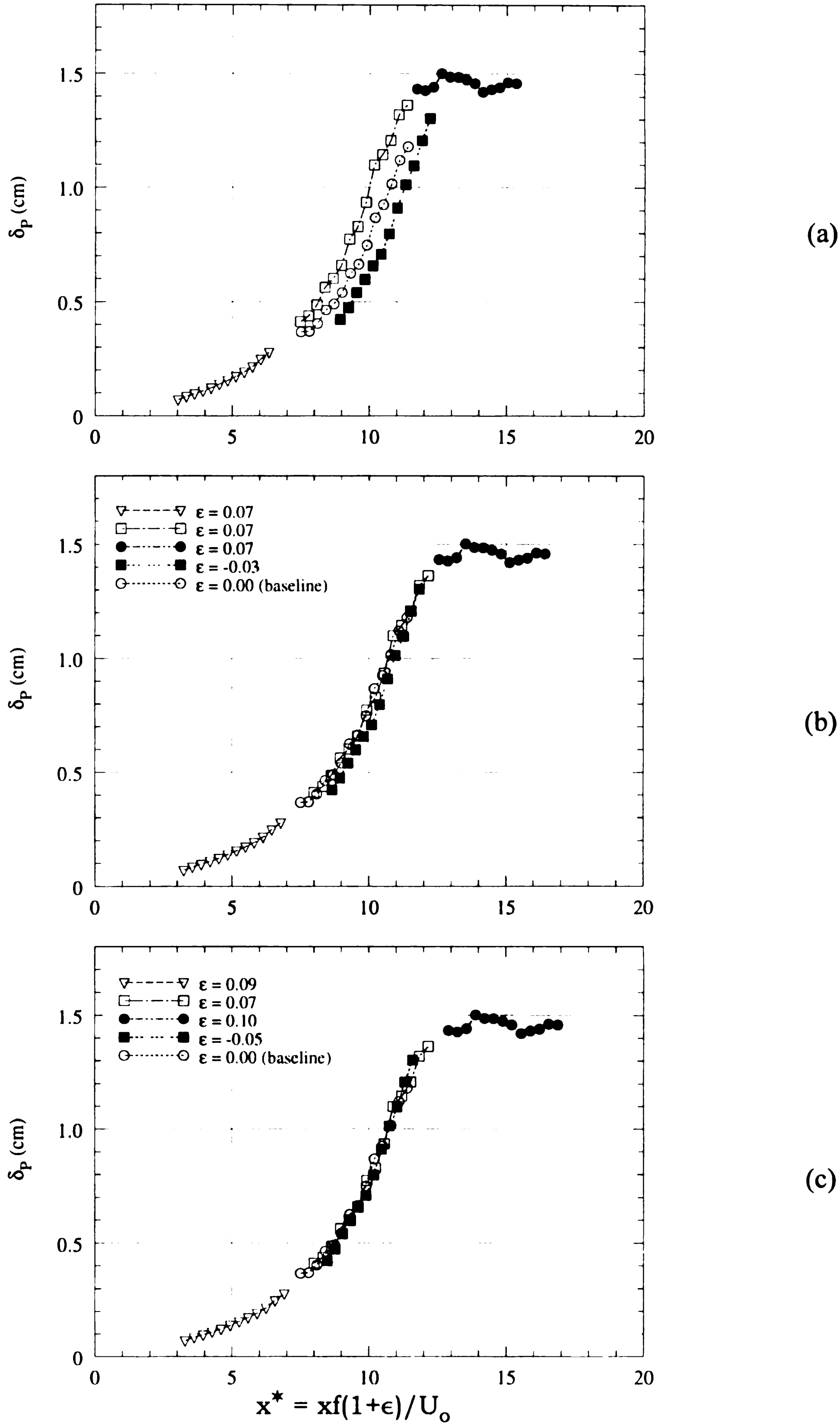

Figure 36. Effect of ϵ scaling on midspan data. (a) unscaled, (b) $\Delta\epsilon \leq 0.10$, (c) best ϵ.

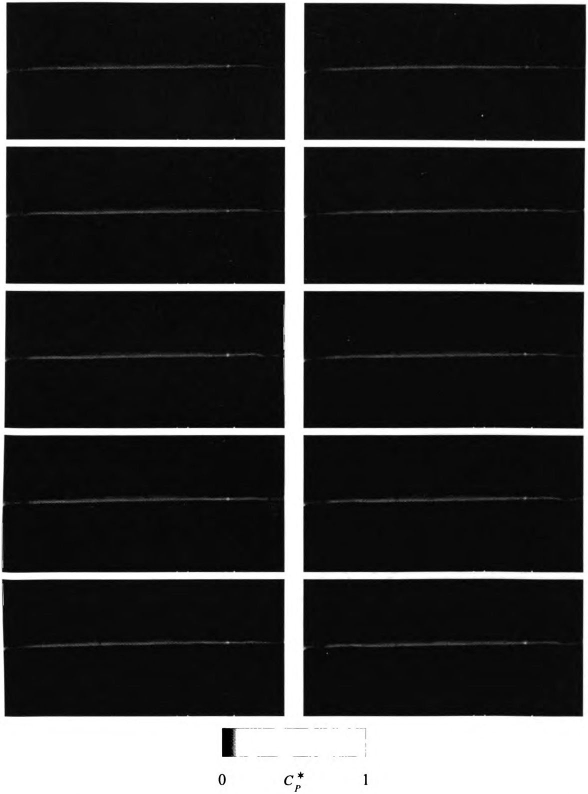

Figure 37. Instantaneous spanwise chemically reacting LIF images of the unforced low speed wake at x = 4 cm. $C_P^* > 0.10$ mapped to white.

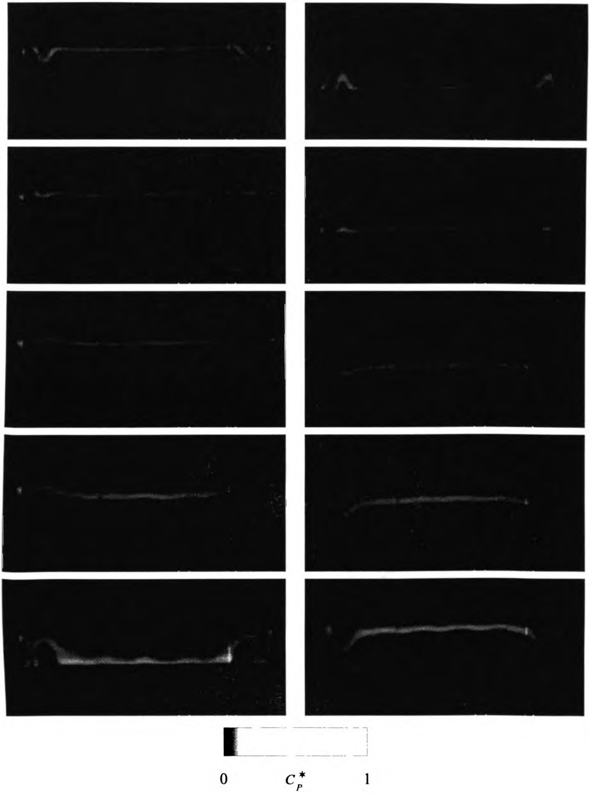

Figure 38. Instantaneous spanwise chemically reacting LIF images of the low speed wake forced at 2%; x = 4 cm. $C_P^* > 0.10$ mapped to white.

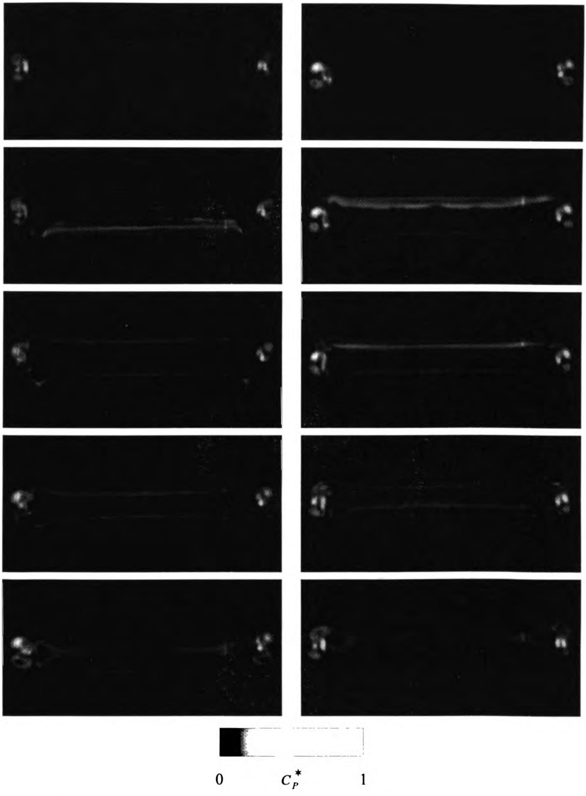

Figure 39. Instantaneous spanwise chemically reacting LIF images of the low speed wake forced at 5%; x = 4 cm. $C_P^* > 0.25$ mapped to white.

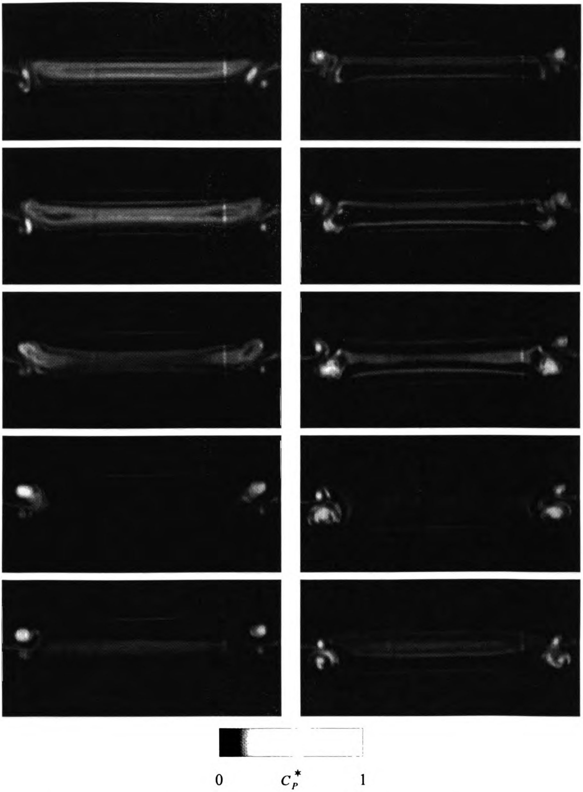

Figure 40. Instantaneous spanwise chemically reacting LIF images of the low speed wake forced at 9%; x = 4 cm. $C_P^\star > 0.25$ mapped to white.

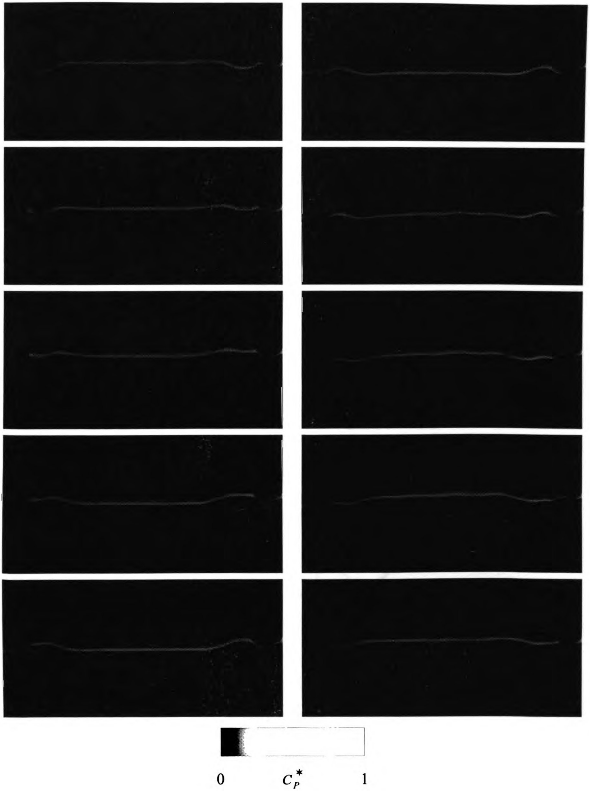

Figure 41. Instantaneous spanwise chemically reacting LIF images of the unforced low speed wake at x = 8 cm. $C_P^* > 0.20$ mapped to white.

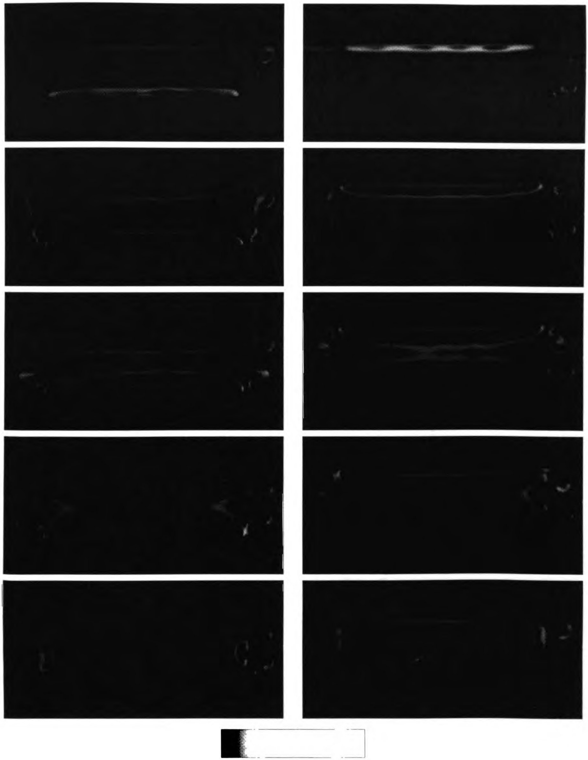

Figure 42. Instantaneous spanwise chemically reacting LIF images of the low speed wake forced at 2%; x = 8 cm. $C_P^* > 0.20$ mapped to white.

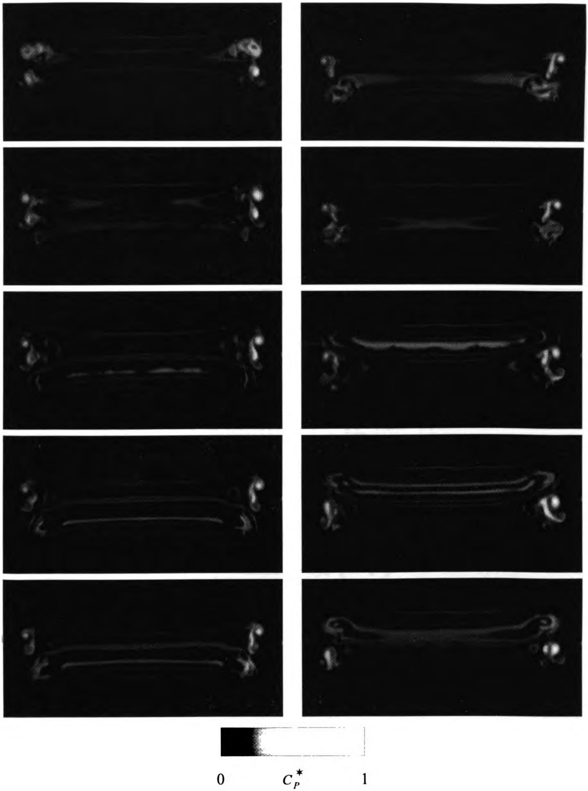

Figure 43. Instantaneous spanwise chemically reacting LIF images of the low speed wake forced at 5%; x = 8 cm. $C_P^* > 0.40$ mapped to white.

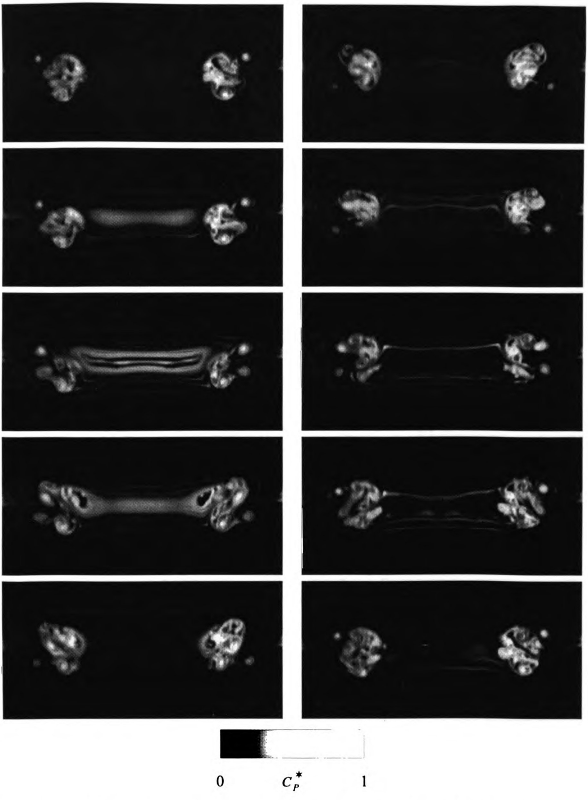

Figure 44. Instantaneous spanwise chemically reacting LIF images of the low speed wake forced at 9%; x = 8 cm. $C_P^* > 0.40$ mapped to white.

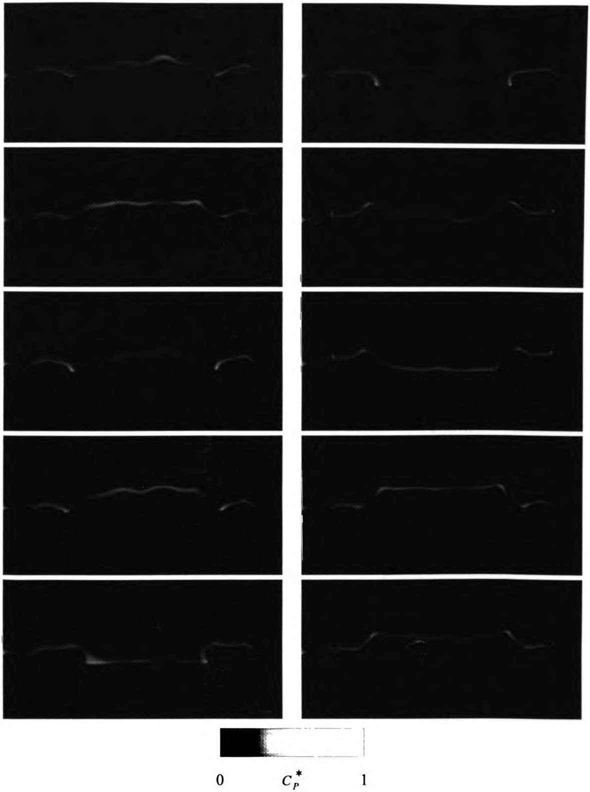

Figure 45. Instantaneous spanwise chemically reacting LIF images of the unforced low speed wake at x = 12 cm. $C_P^* > 0.50$ mapped to white.

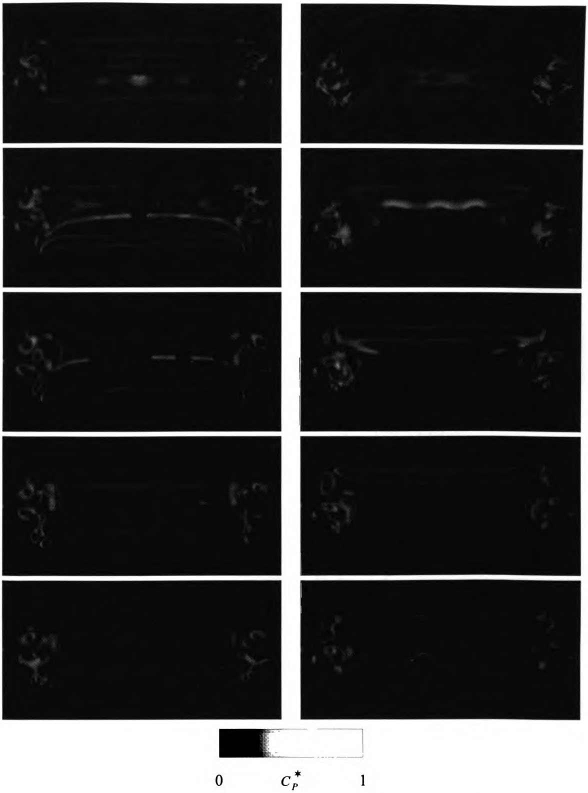

Figure 46. Instantaneous spanwise chemically reacting LIF images of the low speed wake forced at 2%; x = 12 cm. $C_P^* > 0.50$ mapped to white.

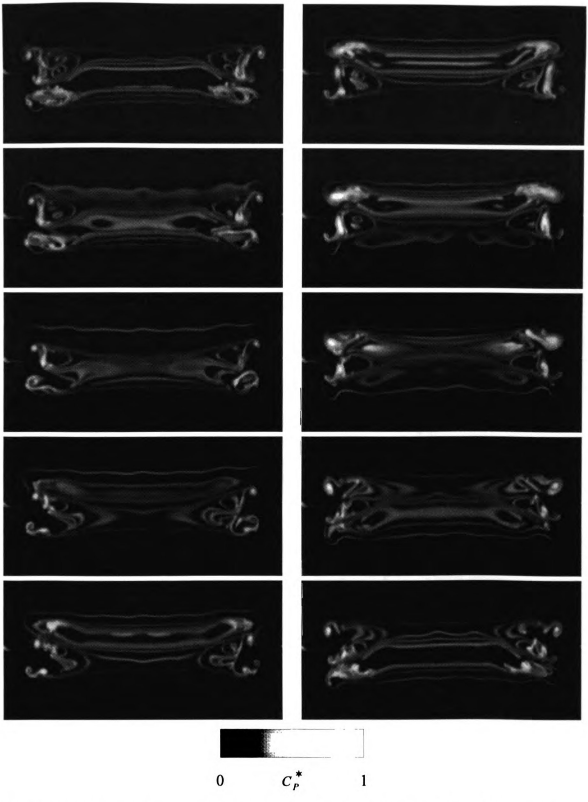

Figure 47. Instantaneous spanwise chemically reacting LIF images of the low speed wake forced at 5%; x = 12 cm. $C_P^* > 0.50$ mapped to white.

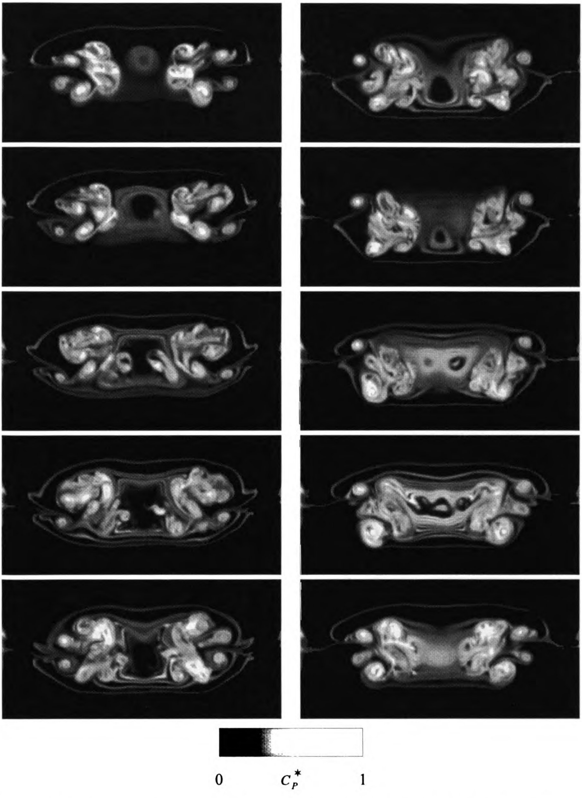

Figure 48. Instantaneous spanwise chemically reacting LIF images of the low speed wake forced at 9%; x = 12 cm. $C_P^* > 0.50$ mapped to white.

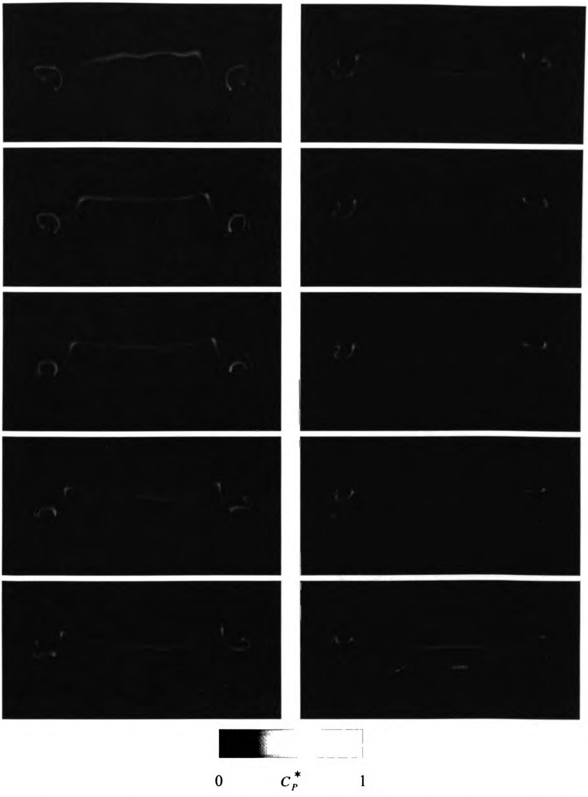

Figure 49. Instantaneous spanwise chemically reacting LIF images of the unforced low speed wake at x = 16 cm. $C_P^* > 0.50$ mapped to white.

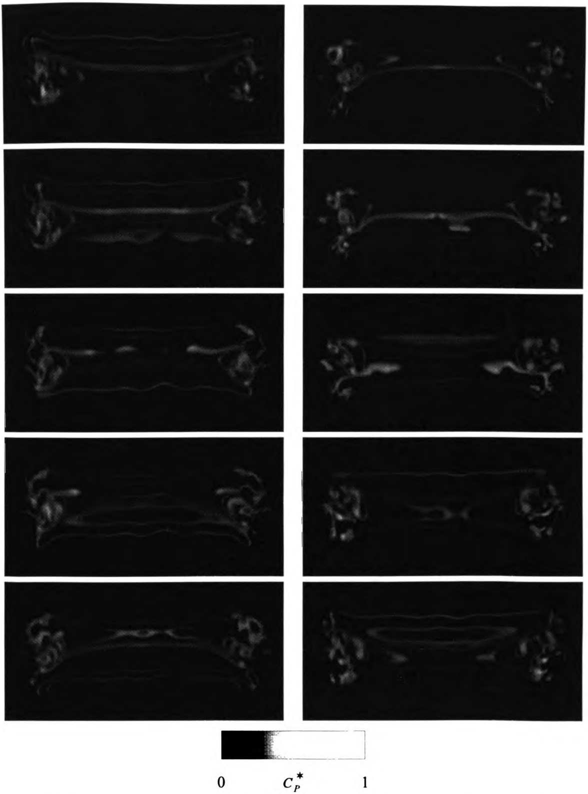

Figure 50. Instantaneous spanwise chemically reacting LIF images of the low speed wake forced at 2%; x = 16 cm. $c_P^* > 0.50$ mapped to white.

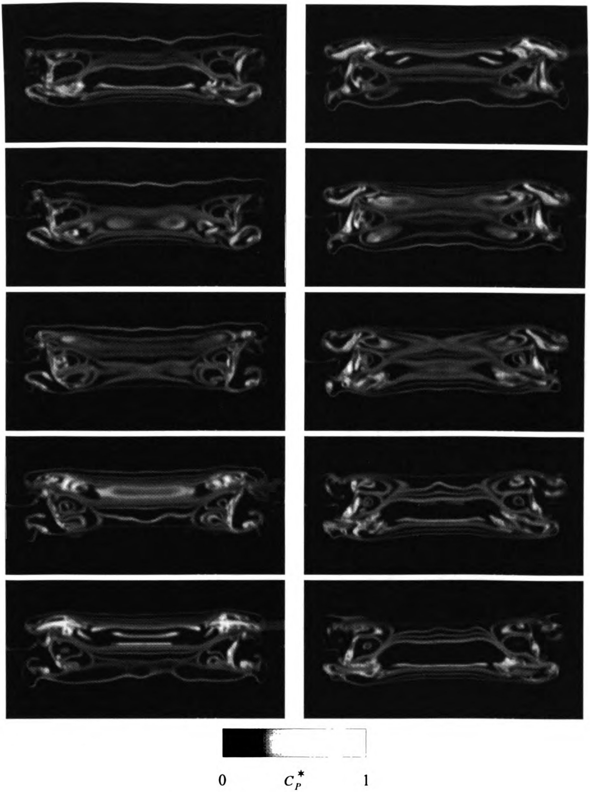

Figure 51. Instantaneous spanwise chemically reacting LIF images of the low speed wake forced at 5%; x = 16 cm. $C_P^* > 0.50$ mapped to white.

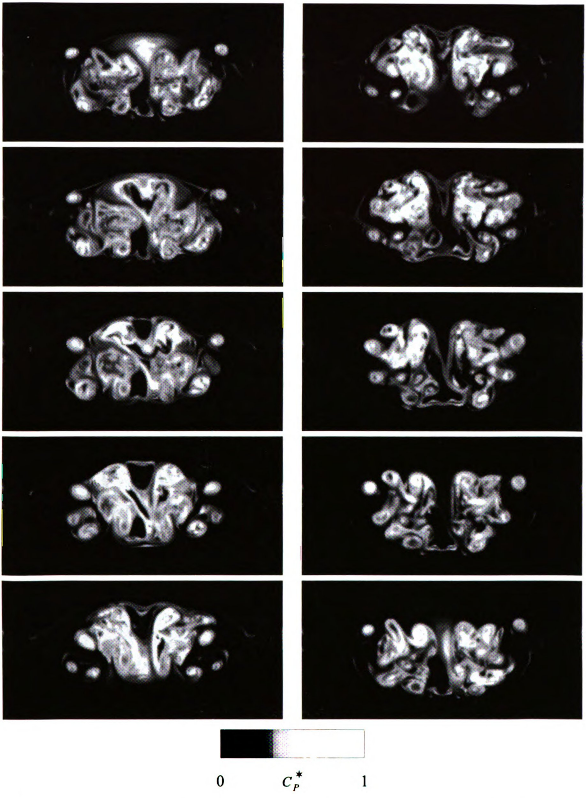

Figure 52. Instantaneous spanwise chemically reacting LIF images of the low speed wake forced at 9%; x = 16 cm. $C_P^* > 0.50$ mapped to white.

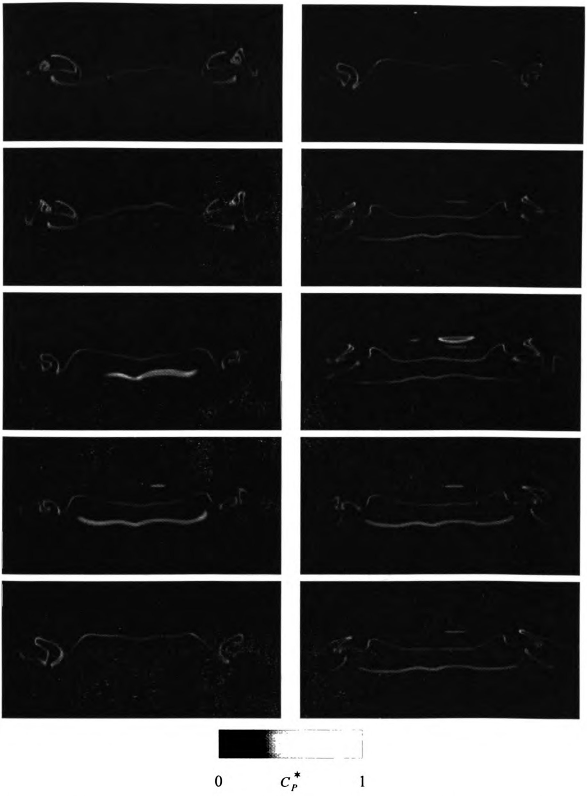

Figure 53. Instantaneous spanwise chemically reacting LIF images of the unforced low speed wake at x = 24 cm. $C_P^* > 0.60$ mapped to white.

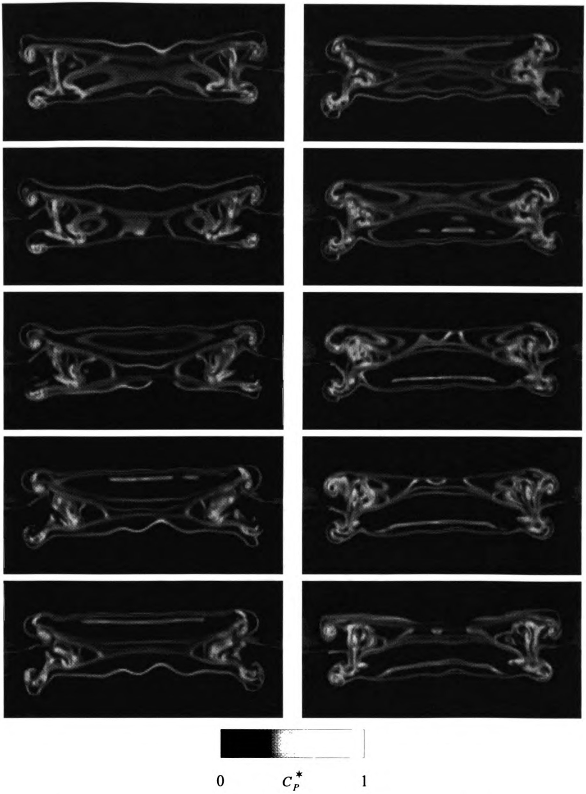

Figure 54. Instantaneous spanwise chemically reacting LIF images of the low speed wake forced at 2%; x = 24 cm. C_P^* > 0.60 mapped to white.

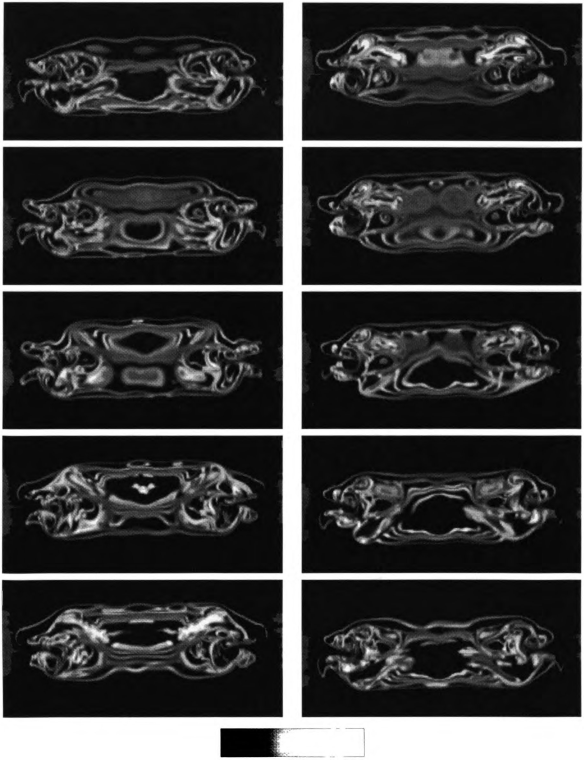

Figure 55. Instantaneous spanwise chemically reacting LIF images of the low speed wake forced at 5%; x = 24 cm. $C_P^* > 0.60$ mapped to white.

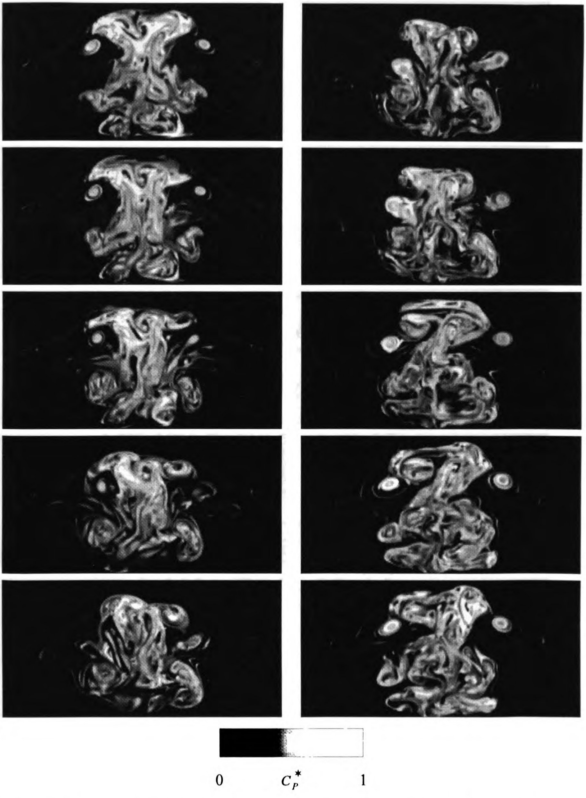

Figure 56. Instantaneous spanwise chemically reacting LIF images of the low speed wake forced at 9%; x = 24 cm. C_P^* > 0.60 mapped to white.

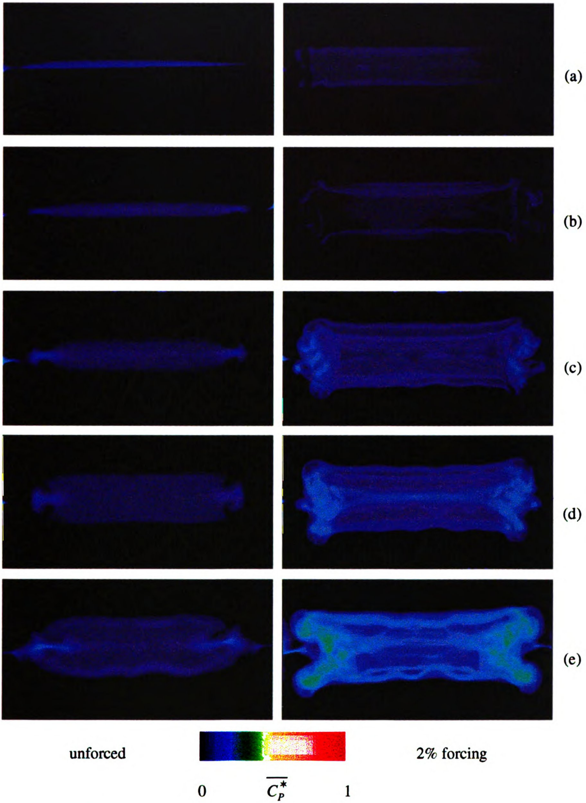

Figure 57. $\overline{C_P^*}$ distribution of the low speed wake at (a) x = 4 cm, (b) x = 8 cm, (c) x = 12 cm, (d) x = 16 cm, (e) x = 24 cm.

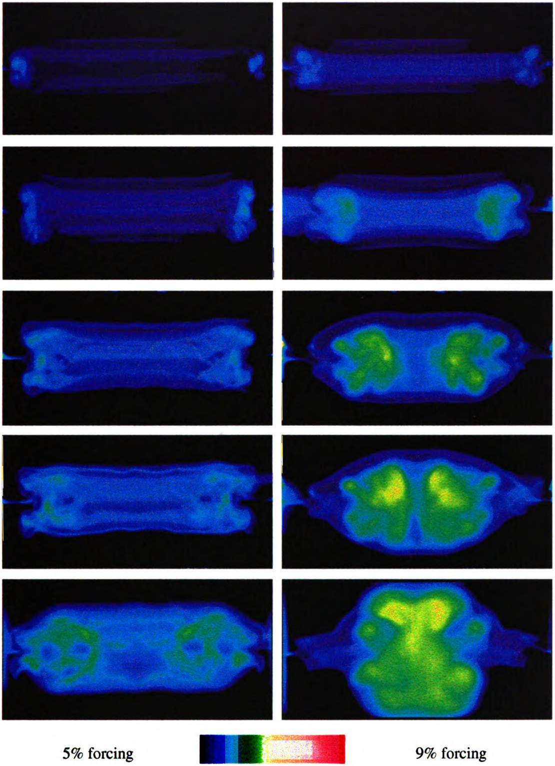

Figure 58. $\overline{C_P^*}$ distribution of the low speed wake at (a) x = 4 cm, (b) x = 8 cm, (c) x = 12 cm, (d) x = 16 cm, (e) x = 24 cm.

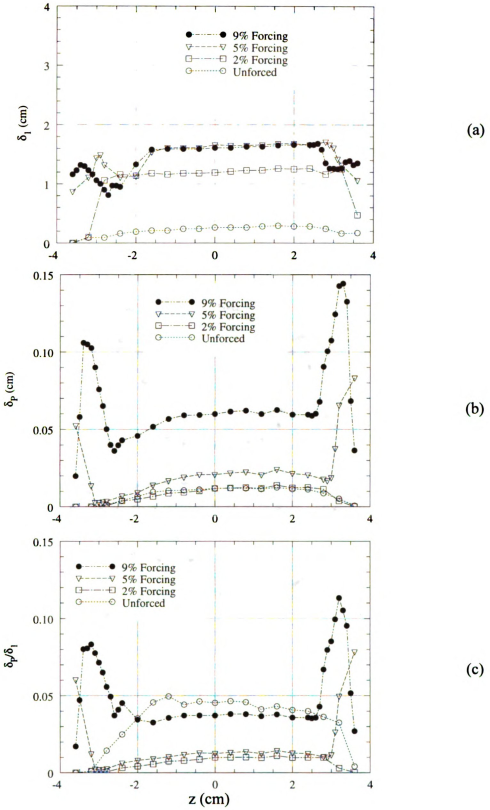

Figure 59. Calculated quantities versus z at x = 4 cm. (a) δ_1, (b) δ_P, (c) δ_P/δ_1.

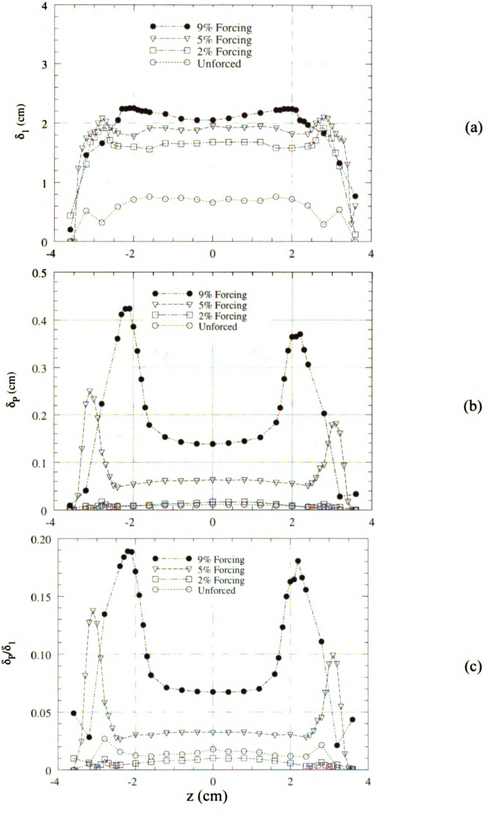

Figure 60. Calculated quantities versus z at x = 8 cm. (a) δ_1, (b) δ_P, (c) δ_P/δ_1.

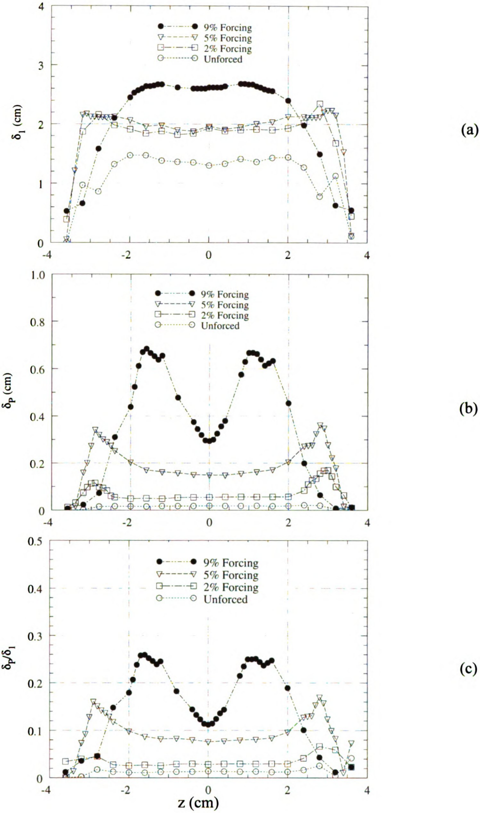

Figure 61. Calculated quantities versus z at x = 12 cm. (a) δ_1, (b) δ_P, (c) δ_P/δ_1.

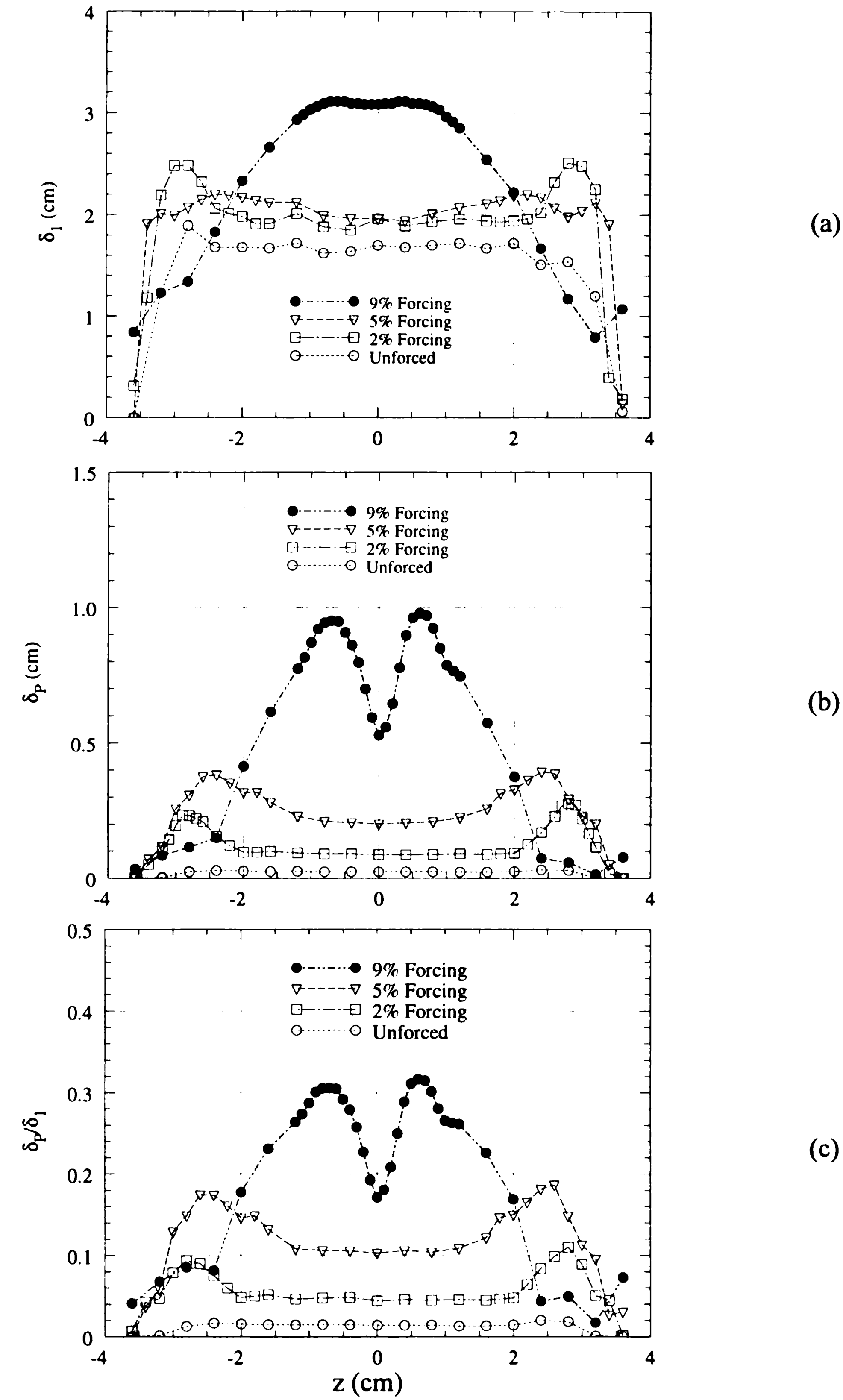

Figure 62. Calculated quantities versus z at x = 16 cm. (a) δ_1, (b) δ_P, (c) δ_P/δ_1.

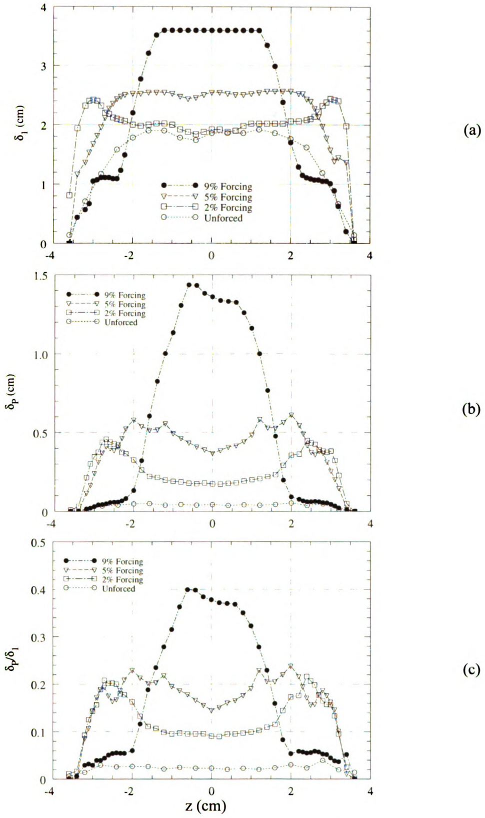

Figure 63. Calculated quantities versus z at x = 24 cm. (a) δ_1, (b) δ_P, (c) δ_P/δ_1.

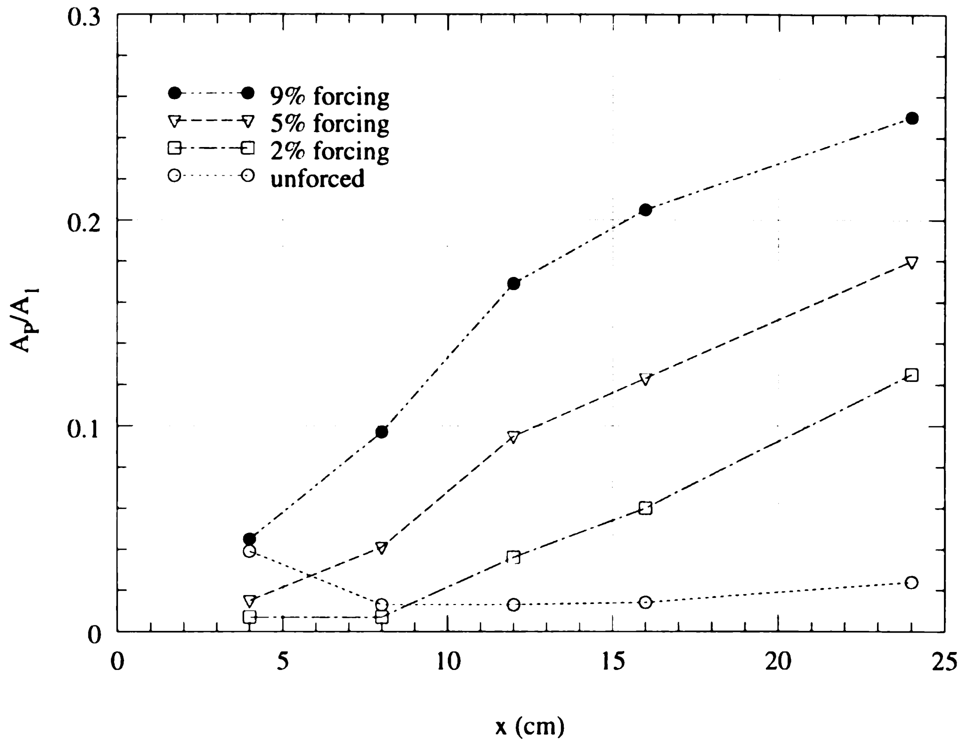

Figure 64. Normalized product area A_P/A_1 versus x from spanwise data for all forcing conditions.

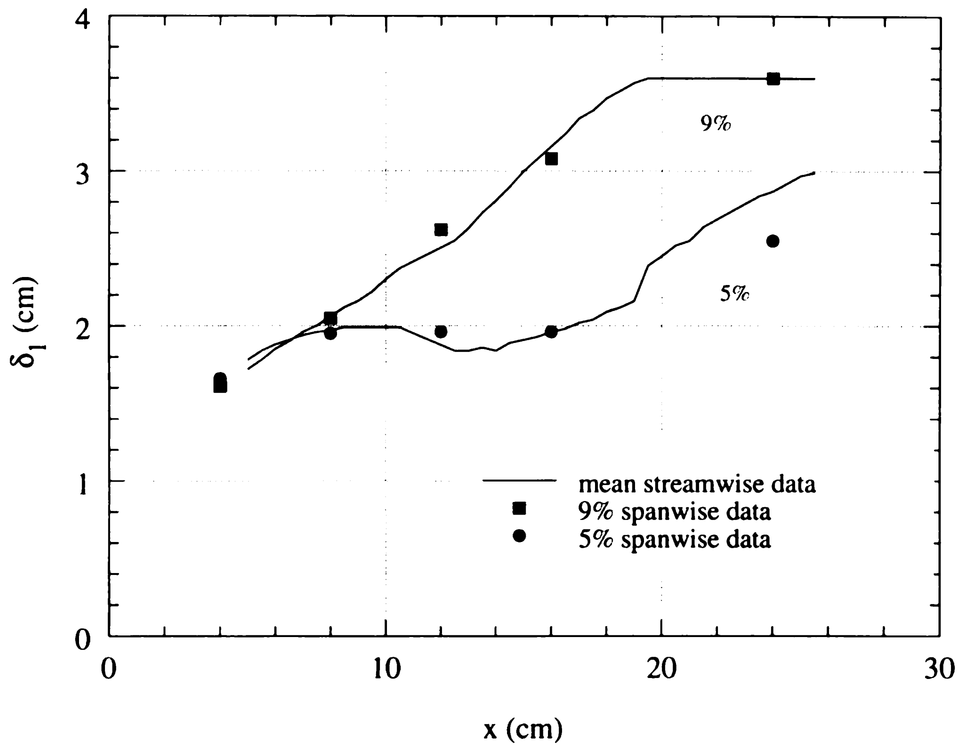

(a)

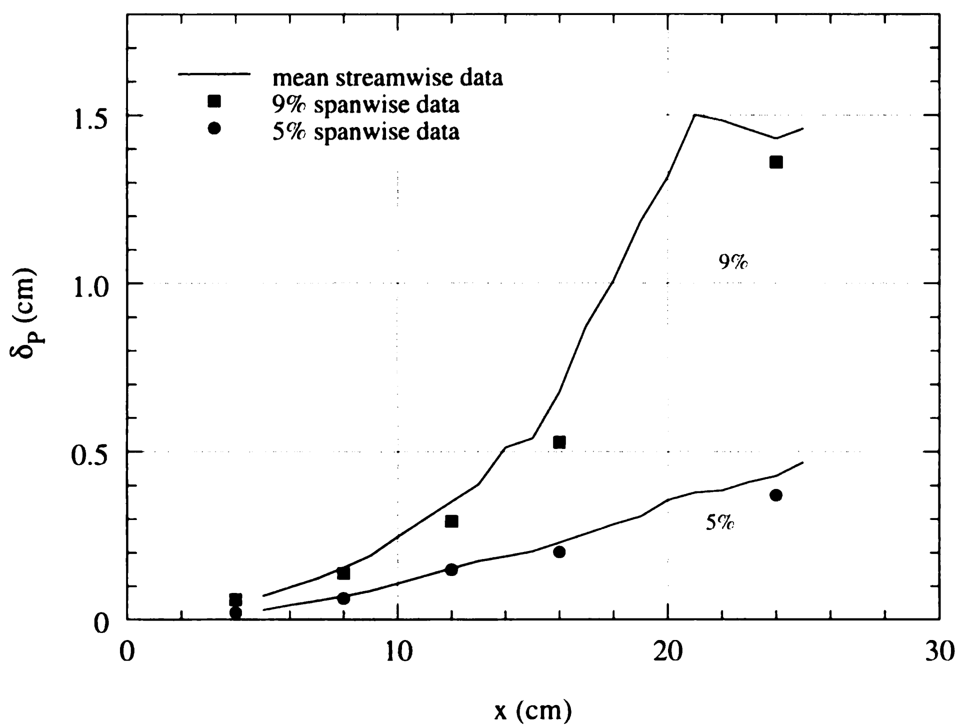

(b)

Figure 65. Comparison of mean streamwise data with spanwise data at z = 0.0 cm; (a) δ_1, (b) δ_P.

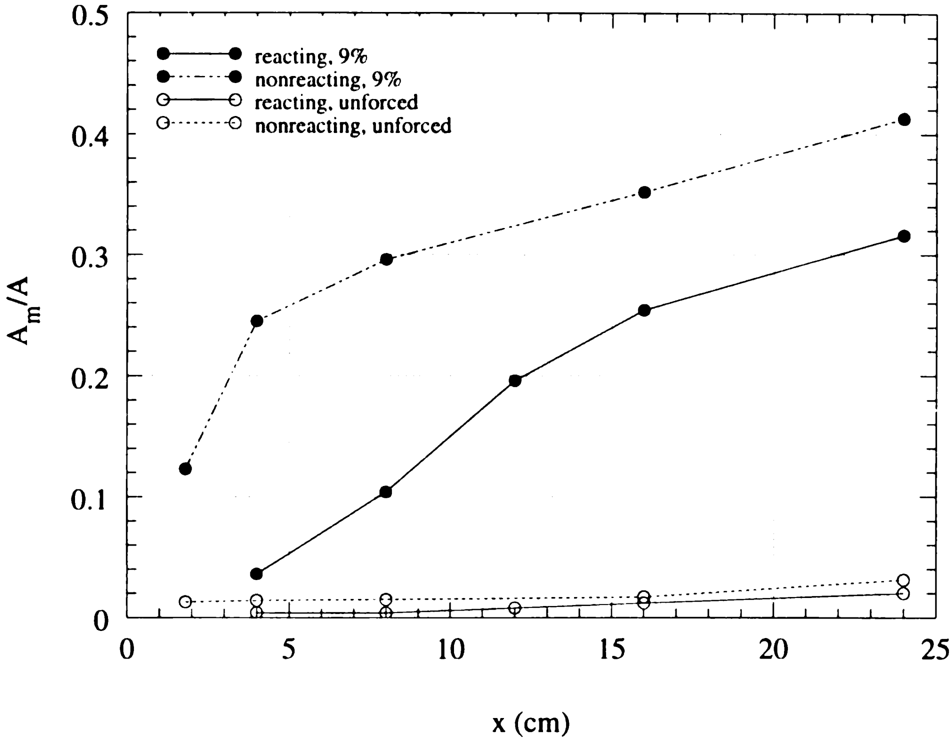

Figure 66. Comparison of the mixed fluid fraction from reacting and nonreacting LIF.

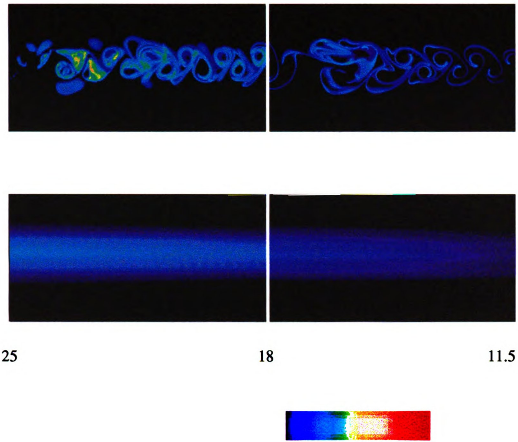

Figure 67. (a) Sample instantaneous and (b) average chemically reacting LIF images for the high speed unforced wake at z = +0.8 cm.

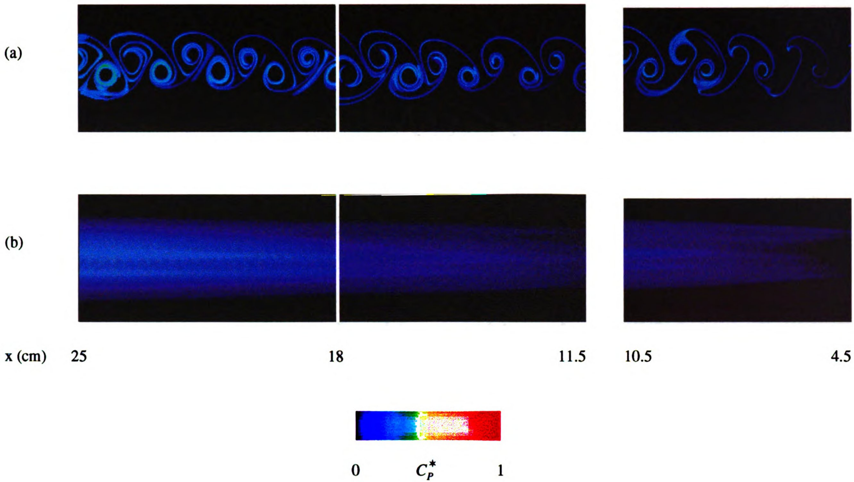

Figure 68. (a) Sample instantaneous and (b) average chemically reacting LIF images for the forced high speed wake at z = +0.8 cm.

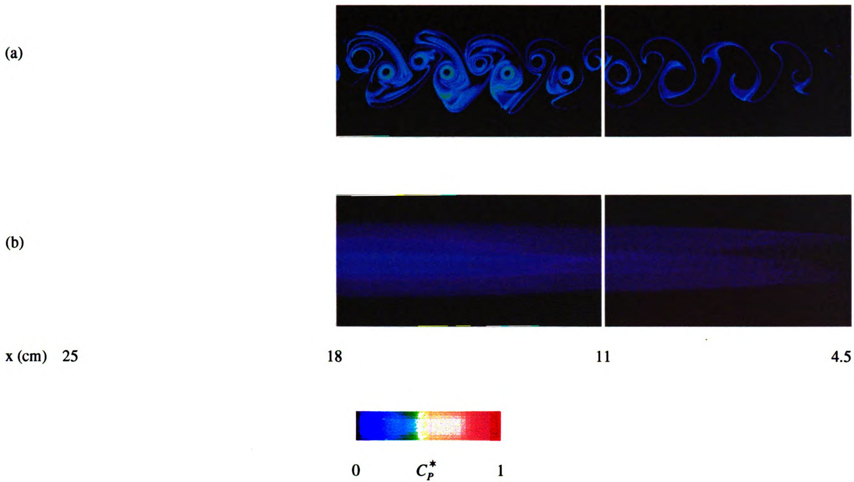

Figure 69. (a) Sample instantaneous and (b) average chemically reacting LIF images for the high speed forced wake at z = -0.8 cm.

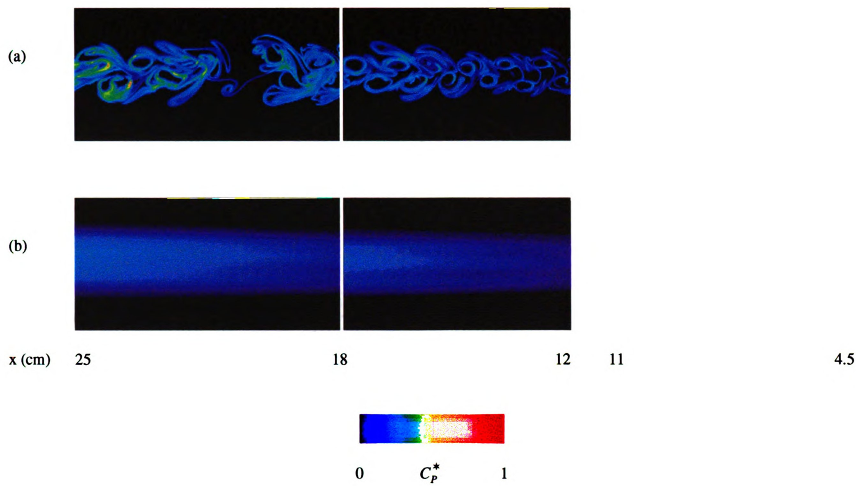

Figure 70. (a) Sample instantaneous and (b) average chemically reacting LIF images for the high speed unforced wake at z = -2.0 cm.

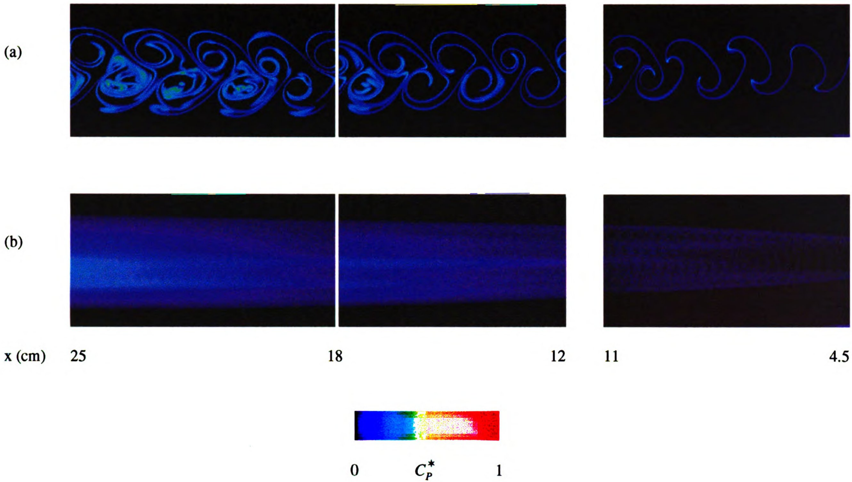

Figure 71. (a) Sample instantaneous and (b) average chemically reacting LIF images for the high speed forced wake at z = -2.0 cm.

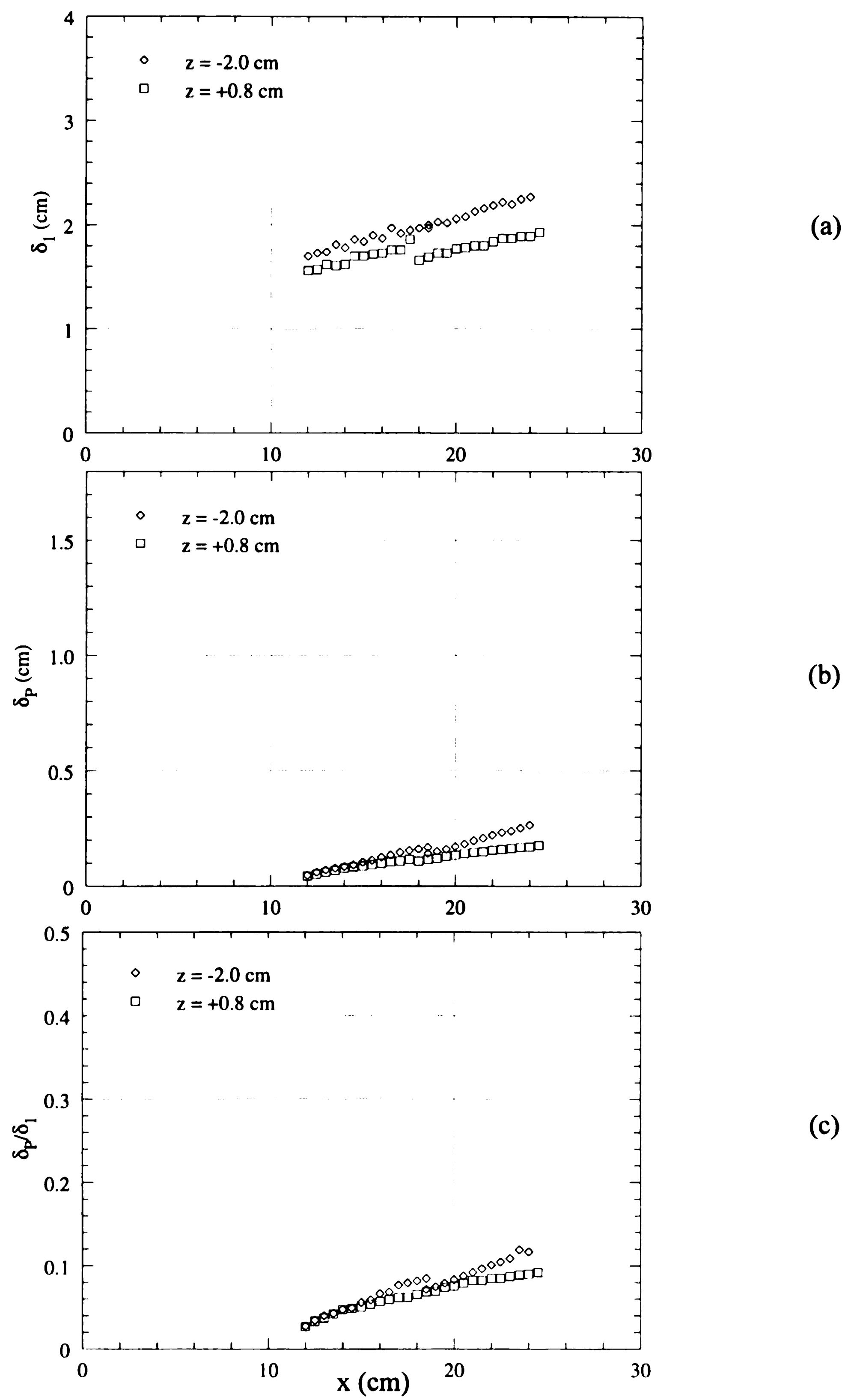

Figure 72. Calculated quantities versus x for the unforced higher speed wake. (a) δ_1, (b) δ_P, (c) δ_P/δ_1.

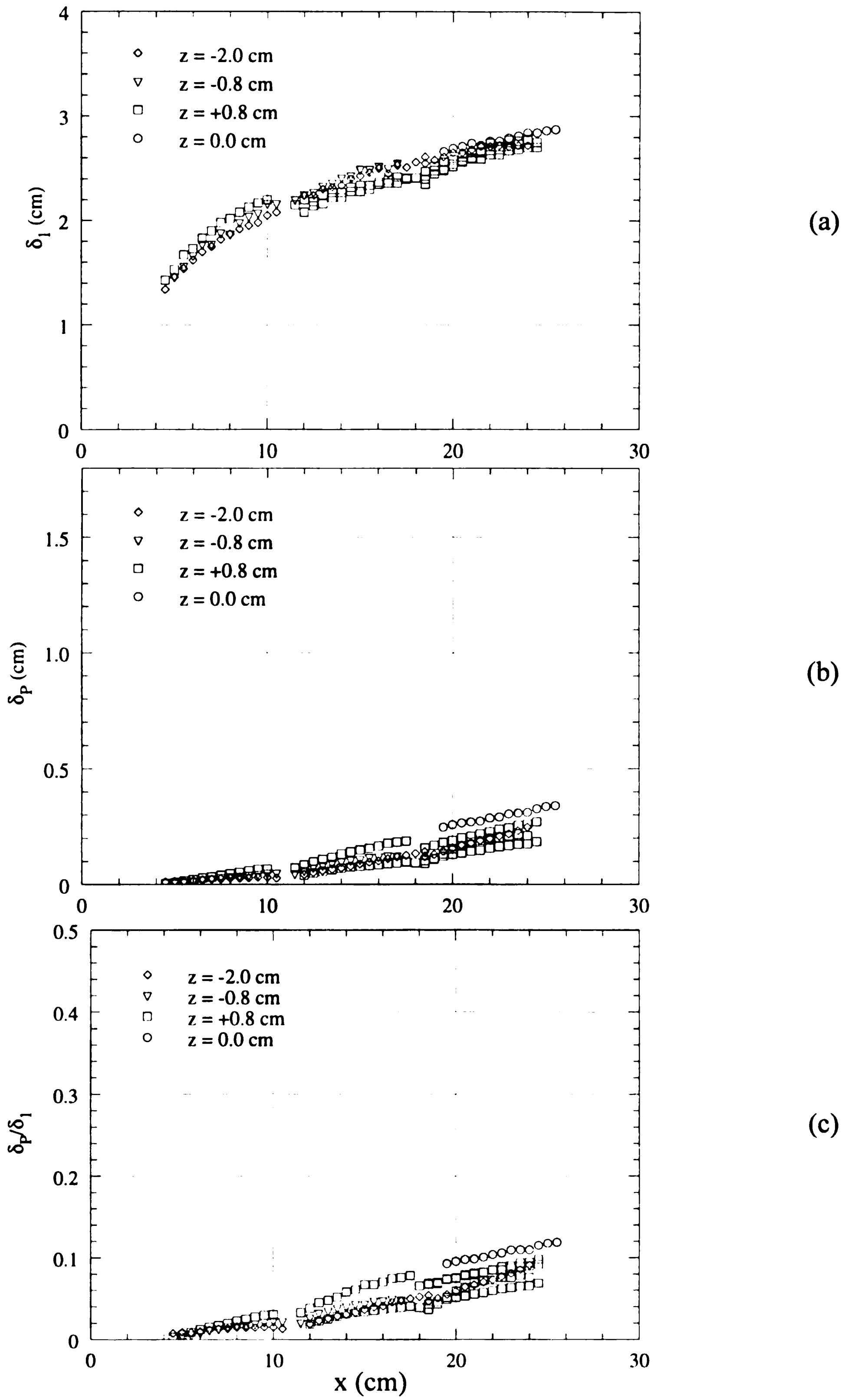

Figure 73. Calculated quantities versus x for the forced higher speed wake. (a) δ_1, (b) δ_P, (c) δ_P/δ_1.

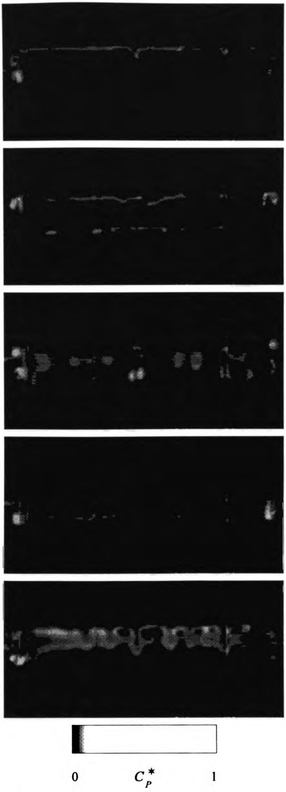

Figure 74. Instantaneous spanwise images of the forced higher speed wake at x = 4 cm. $C_P^* > 0.10$ mapped to white.

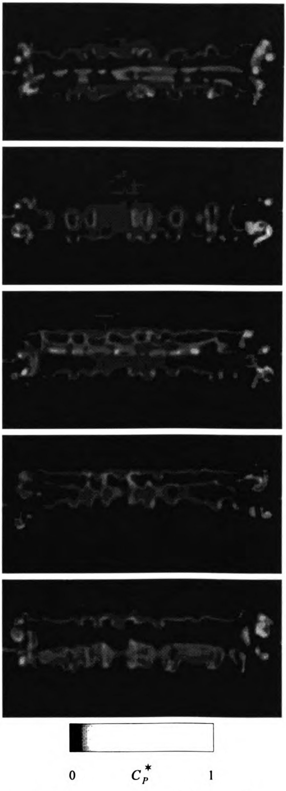

Figure 75. Instantaneous spanwise images of the forced higher speed wake at x = 8 cm. $C_P^* > 0.20$ mapped to white.

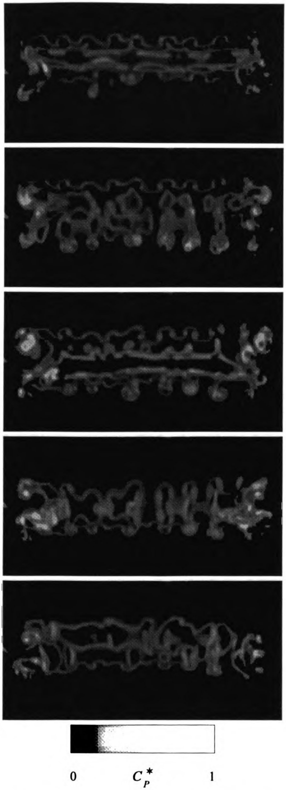

Figure 76. Instantaneous spanwise images of the forced higher speed wake at x = 12 cm. $C_P^* > 0.50$ mapped to white.

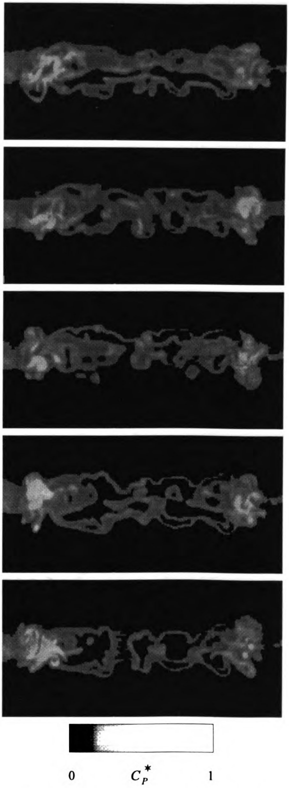

Figure 77. Instantaneous spanwise images of the unforced higher speed wake at x = 16 cm. $C_P^* > 0.50$ mapped to white.

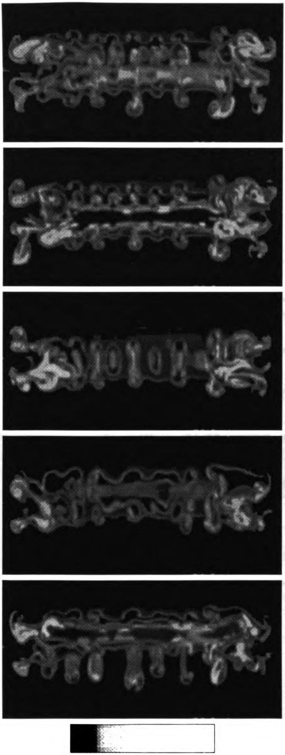

0 C_P^* 1

Figure 78. Instantaneous spanwise images of the forced higher speed wake at x = 16 cm. C_P^* > 0.50 mapped to white.

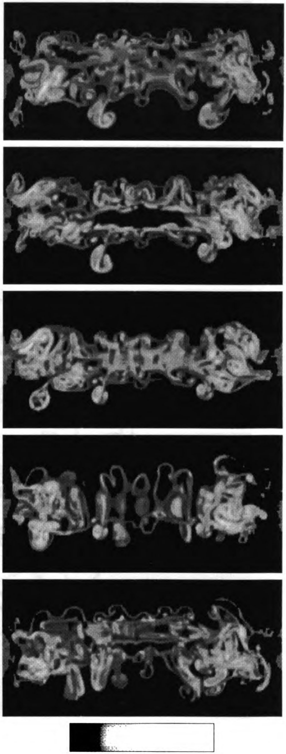

0 C_P^* 1

Figure 79. Instantaneous spanwise images of the forced higher speed wake at x = 24 cm. C_P^* > 0.60 mapped to white.

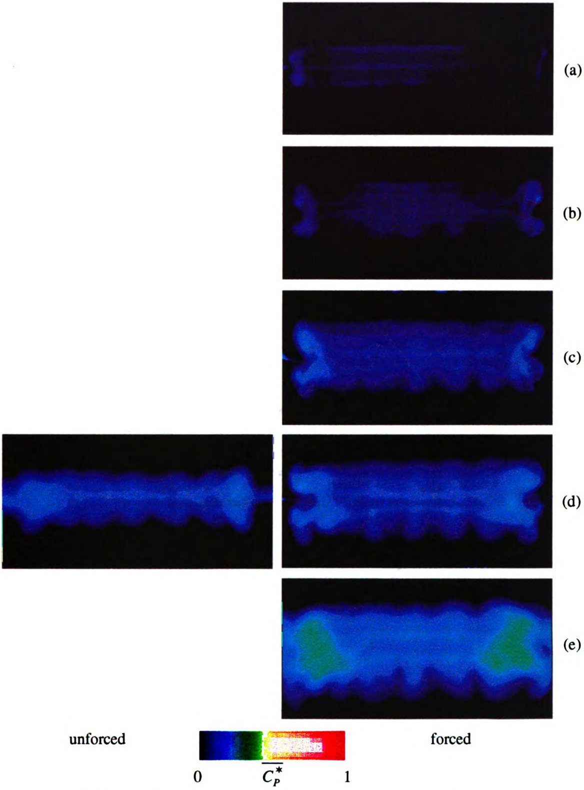

Figure 80. $\overline{C_P^*}$ distribution of the higher speed wake at (a) x = 4 cm, (b) x = 8 cm, (c) x = 12 cm, (d) x = 16 cm, (e) x = 24 cm.

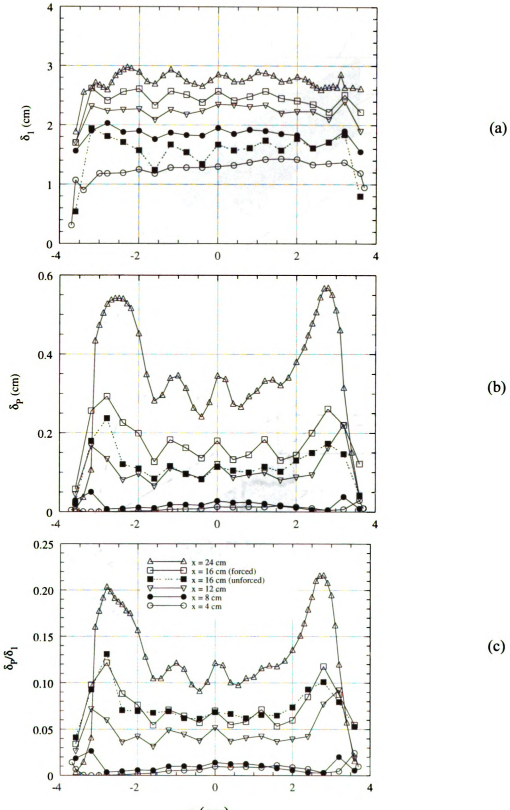

Figure 81. Calculated quantities for the higher speed wake. (a) δ_1, (b) δ_P, (c) δ_P/δ_1.

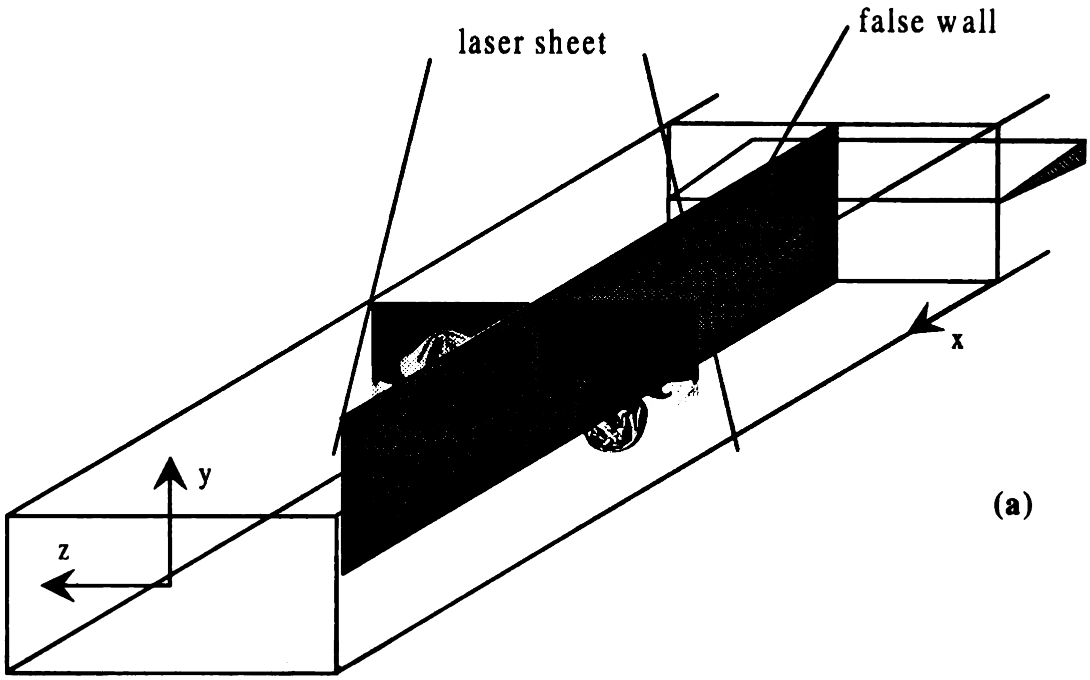

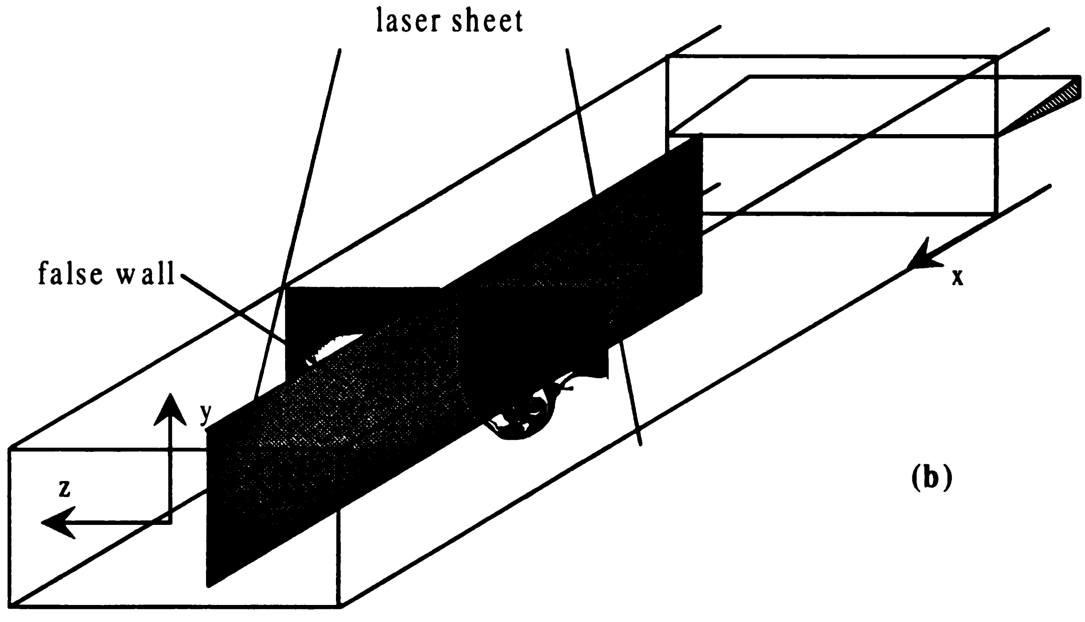

Figure 82. Schematic of the test section with the false wall mounted at (a) x = 0 cm, and (b) x = 3.5 cm.

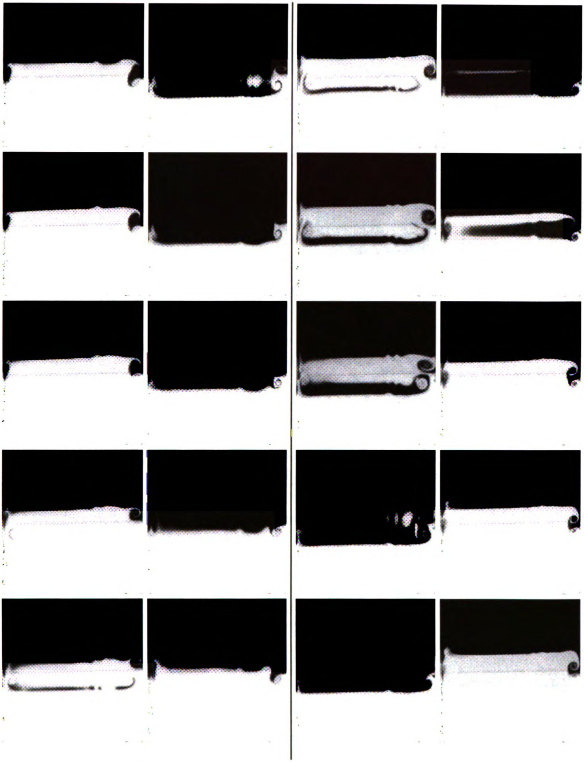

(a) (b)

Figure 83. LIF images at x = 1.8 cm of the wake with the false wall mounted at x = 0 cm; (a) 5% forcing, (b) 9% forcing.

(a) (b)

Figure 84. LIF images at x = 4 cm of the wake with the false wall mounted at x = 0 cm; (a) 5% forcing, (b) 9% forcing.

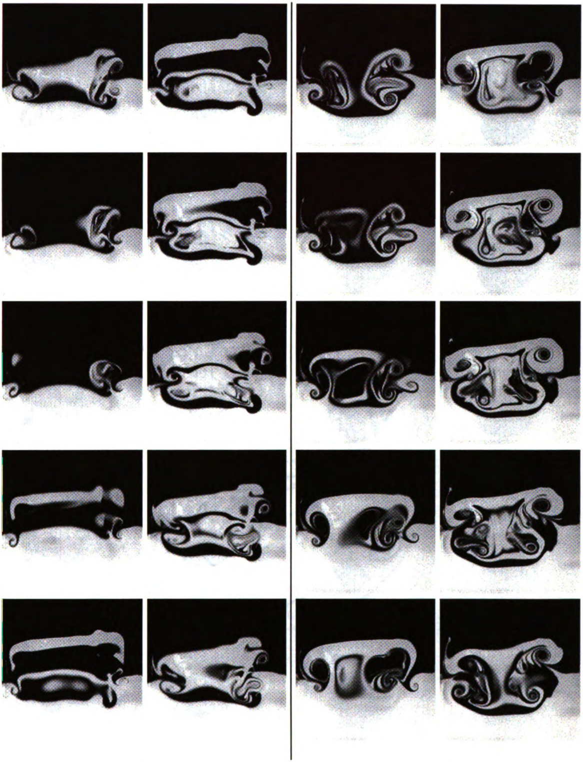

(a) (b)

Figure 85. LIF images at x = 8 cm of the wake with the false wall mounted at x = 0 cm; (a) 5% forcing, (b) 9% forcing.

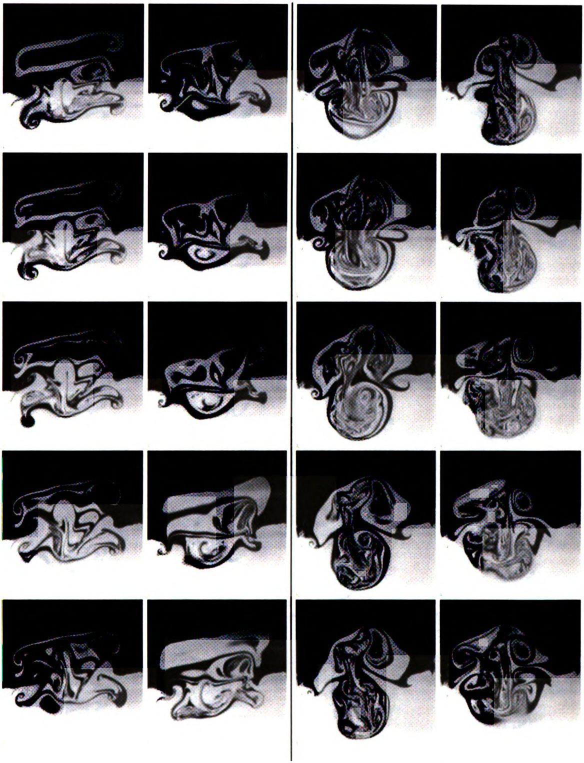

(a) (b)

Figure 86. LIF images at x = 16 cm of the wake with the false wall mounted at x = 0 cm; (a) 5% forcing, (b) 9% forcing.

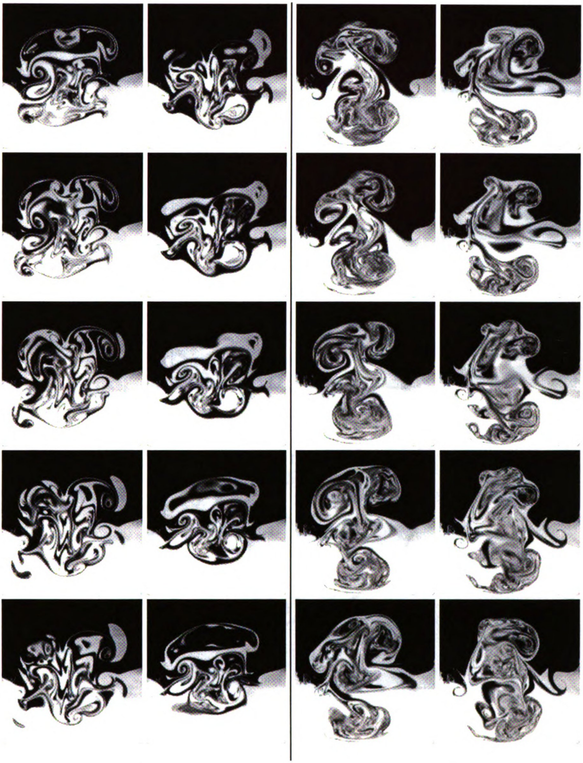

(a) (b)

Figure 87. LIF images at x = 24 cm of the wake with the false wall mounted at x = 0 cm; (a) 5% forcing, (b) 9% forcing.

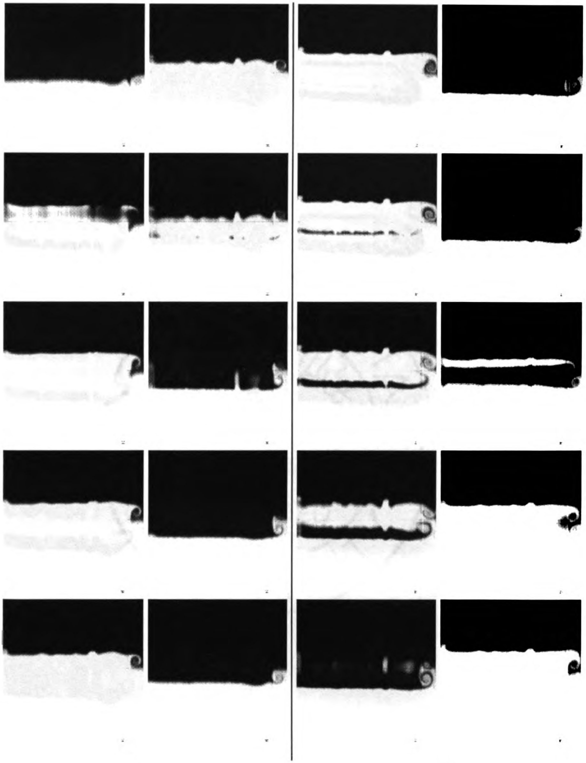

(a) (b)

Figure 88. LIF images at x = 1.8 cm of the wake with the false wall mounted at x = 3.5 cm; (a) 5% forcing, (b) 9% forcing.

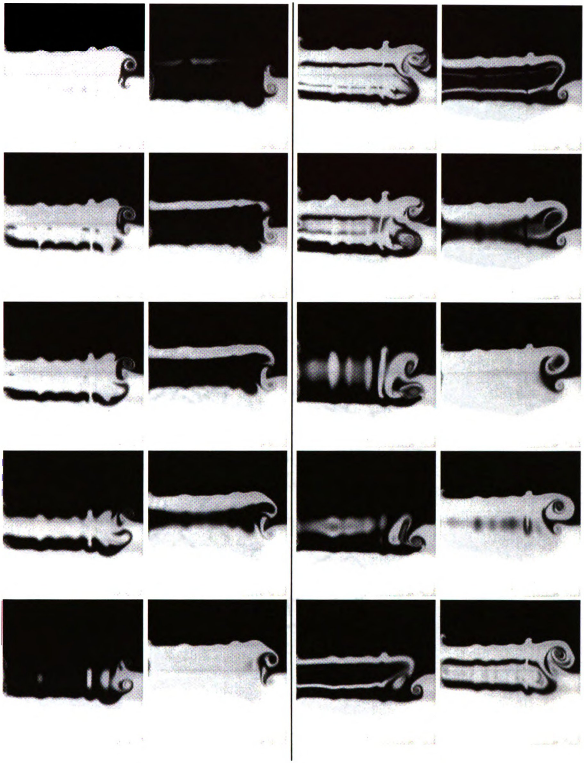

(a) (b)

Figure 89. LIF images at x = 4 cm of the wake with the false wall mounted at x = 3.5 cm; (a) 5% forcing, (b) 9% forcing.

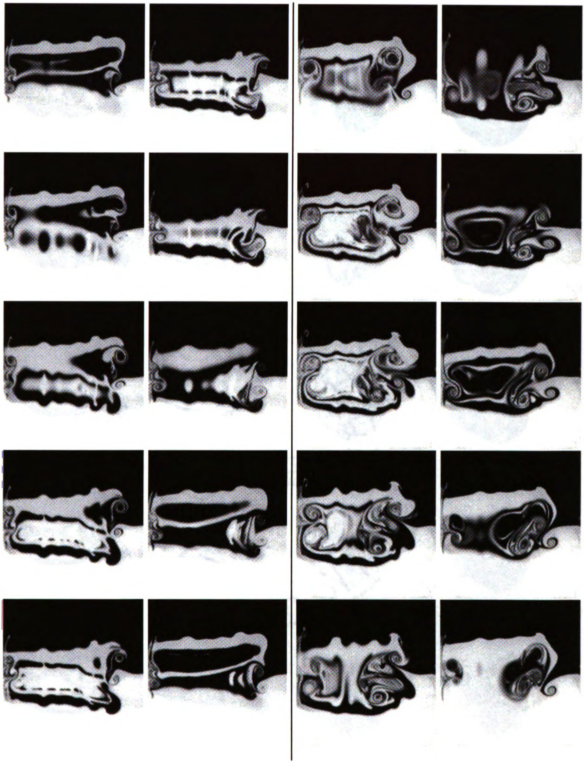

(a) (b)

Figure 90. LIF images at x = 8 cm of the wake with the false wall mounted at x = 3.5 cm; (a) 5% forcing, (b) 9% forcing.

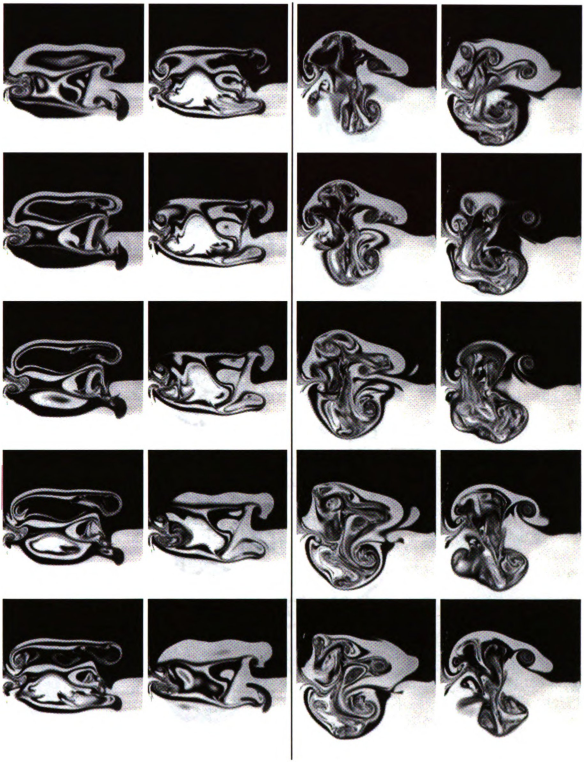

(a) (b)

Figure 91. LIF images at x = 16 cm of the wake with the false wall mounted at x = 3.5cm; (a) 5% forcing, (b) 9% forcing.

(a) (b)

Figure 92. LIF images at x = 24 cm of the wake with the false wall mounted at x = 3.5 cm; (a) 5% forcing, (b) 9% forcing.

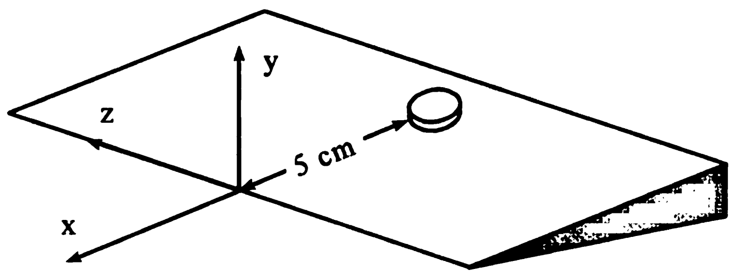

Figure 93. Illustration of the splitter plate tip with the peg mounted on the upper surface (not to scale).

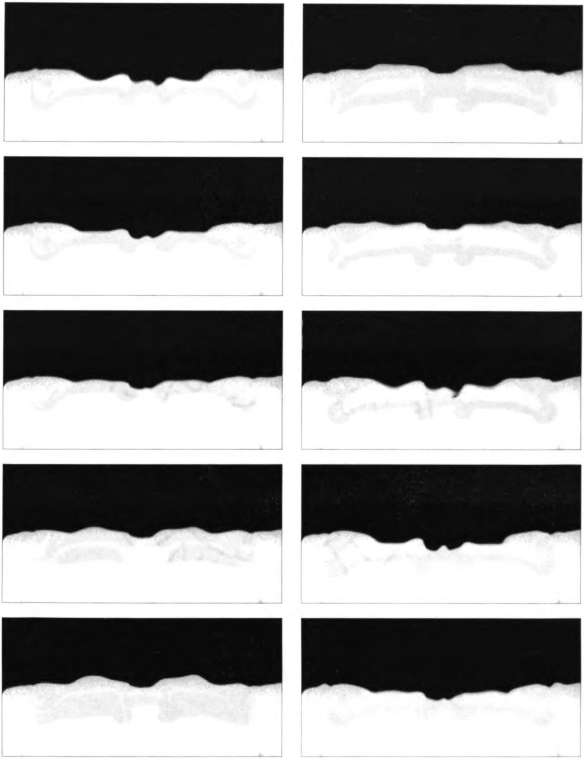

Figure 94. Instantaneous spanwise images of the unforced peg wake at x = 16 cm.

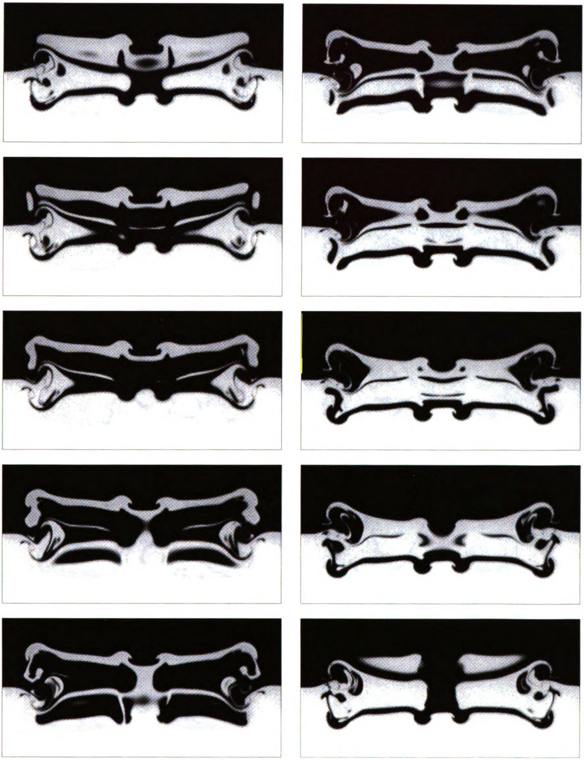

Figure 95. Instantaneous spanwise images of the peg wake forced at 2%; x = 16 cm.

Figure 96. Instantaneous spanwise images of the peg wake forced at 5%; x = 16 cm.

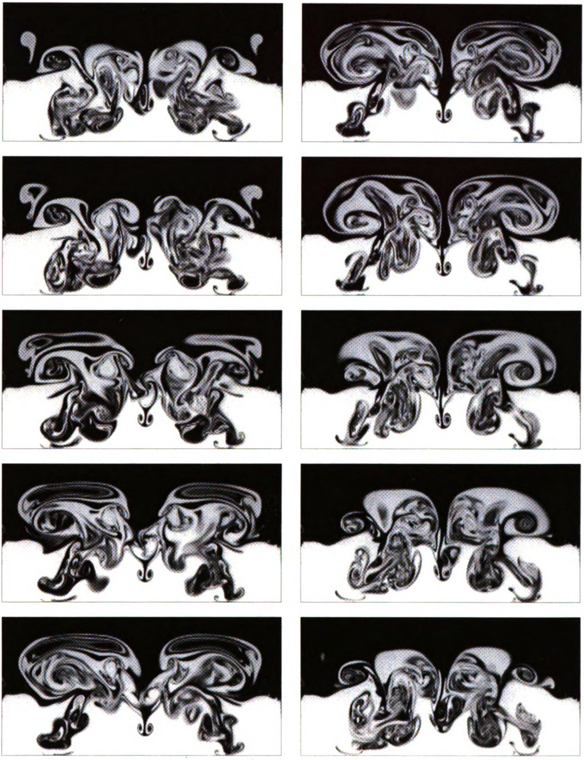

Figure 97. Instantaneous spanwise images of the peg wake forced at 9%; x = 16 cm.

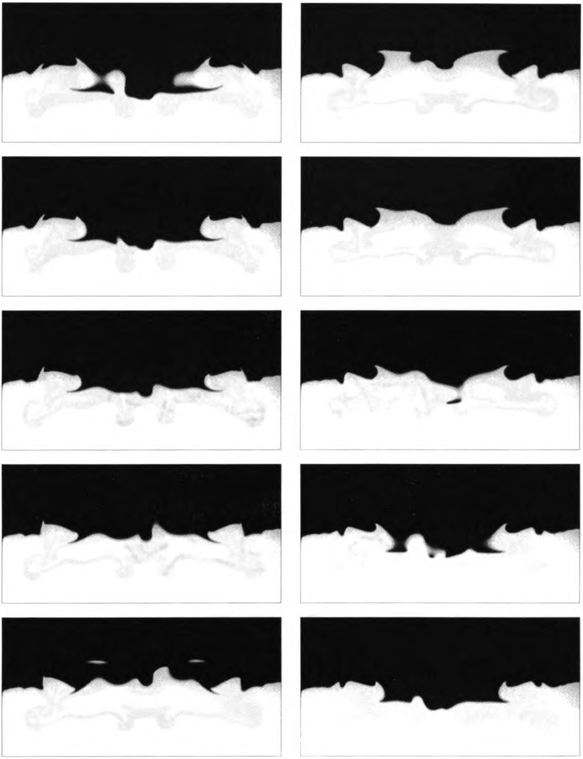

Figure 98. Instantaneous spanwise images of the unforced peg wake at x = 24 cm.

Figure 99. Instantaneous spanwise images of the peg wake forced at 2%; x = 24 cm.

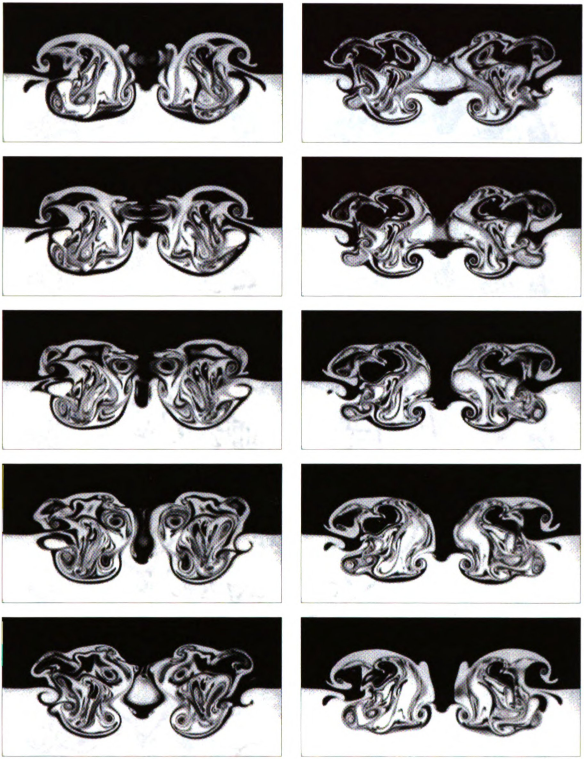

Figure 100. Instantaneous spanwise images of the peg wake forced at 5%; x = 24 cm.

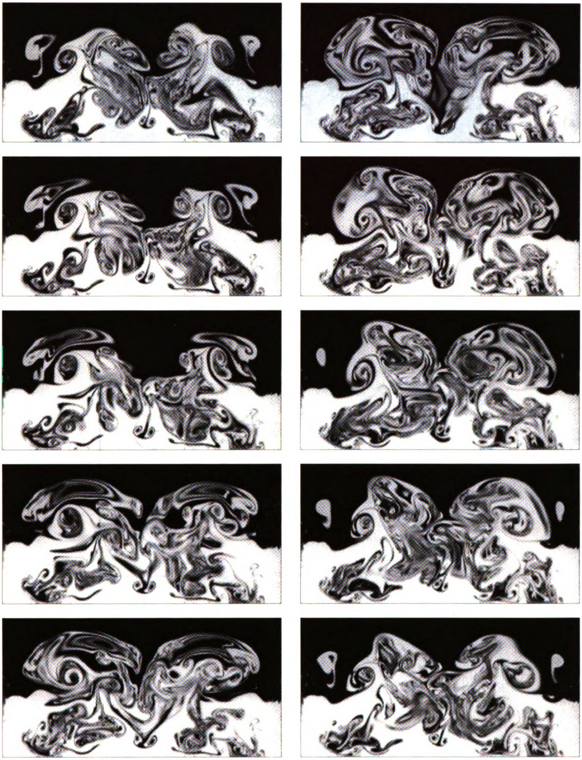

Figure 101. Instantaneous spanwise images of the peg wake forced at 9%; x = 24 cm.

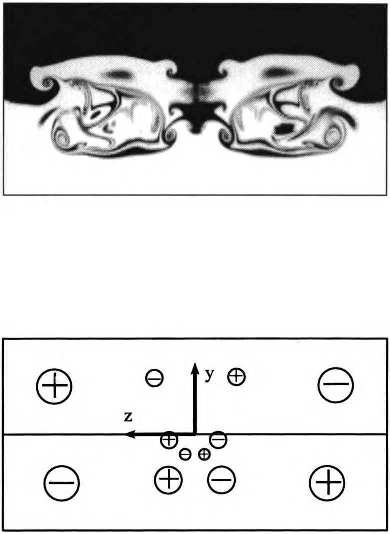

(a)

(b)

Figure 102. Effect of the peg on wake structure. (a) Sample experimental image, (b) illustration of streamwise vorticity sign and approximate strength.

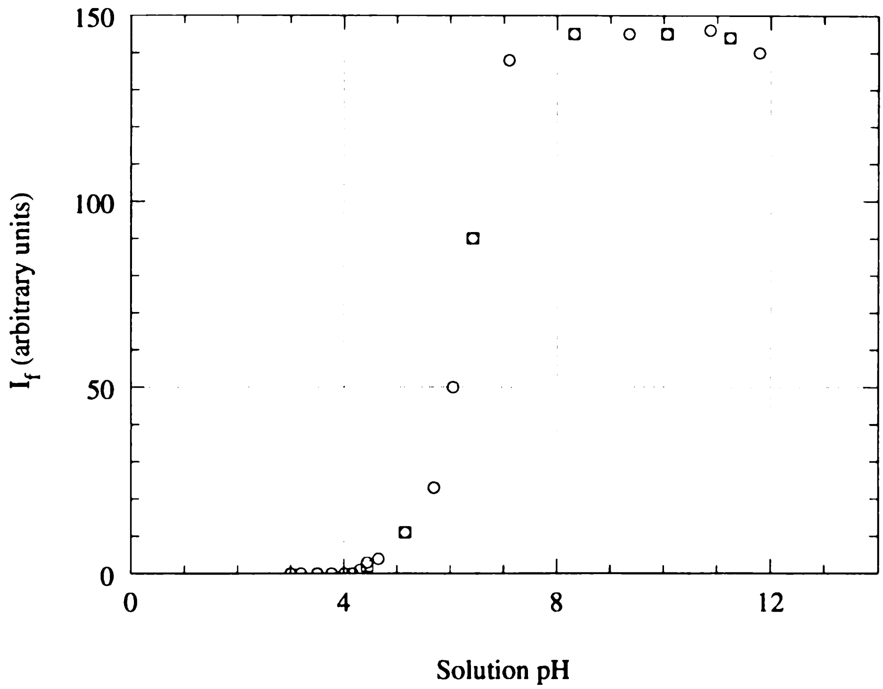

Figure A.1. Fluorescence intensity versus pH behavior of fluorescein dye.

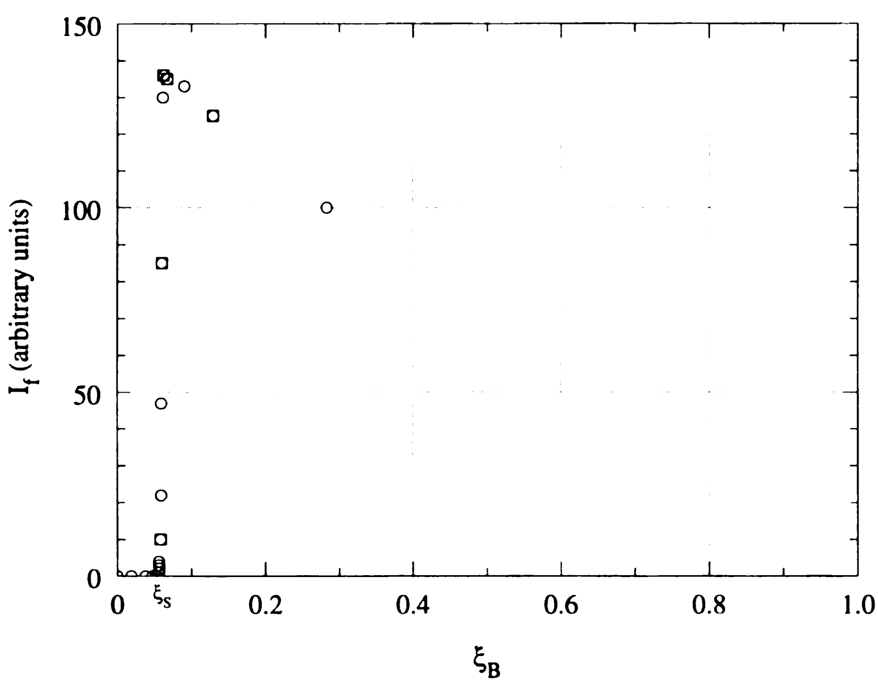

Figure A.2. Representative curve of fluorescence intensity versus base volume fraction.

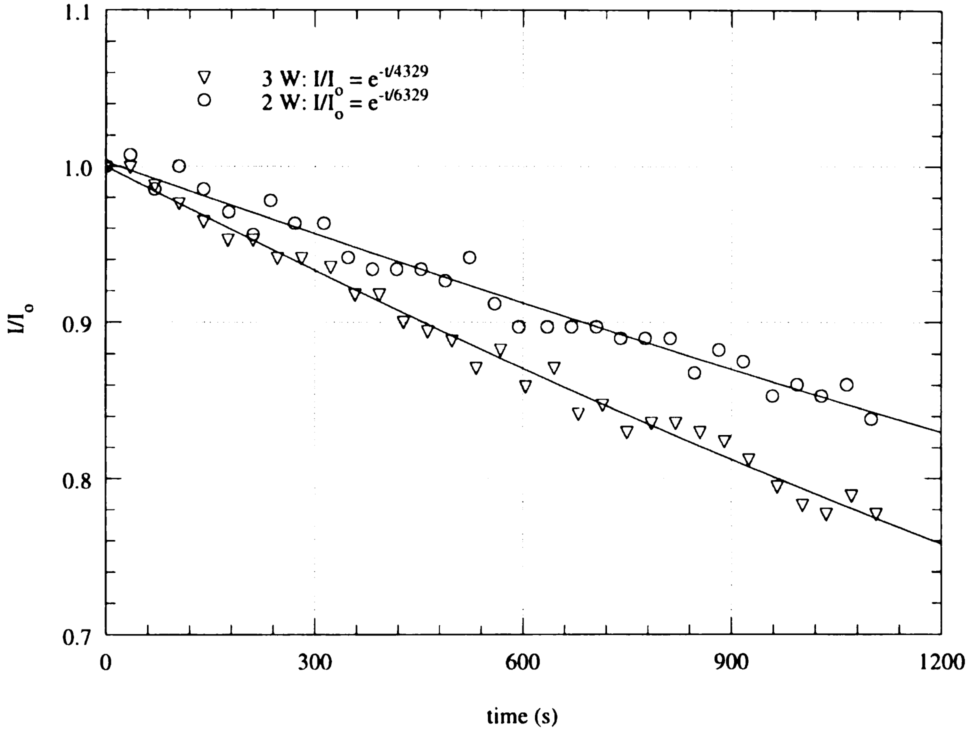

Figure A.3. Effects of dye bleaching in the titration reference chamber for 2 W and 3 W laser power.

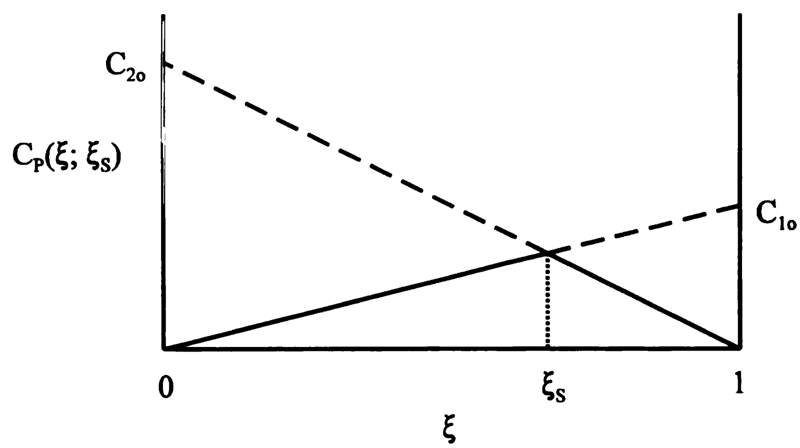

Figure A.4. $C_P(\xi; \xi_S)$ for a fast, irreversible reaction.

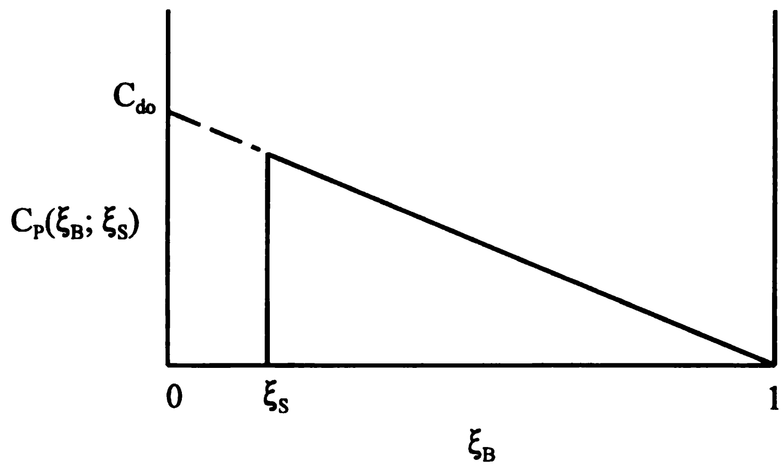

Figure A.5. $C_P(\xi_B; \xi_S)$ for a chemically reacting LIF experiment.

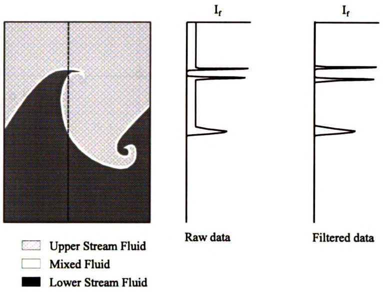

Figure B.1. Schematic of a wake flow and intensity profiles along the dashed line for raw data and data that had been filtered.

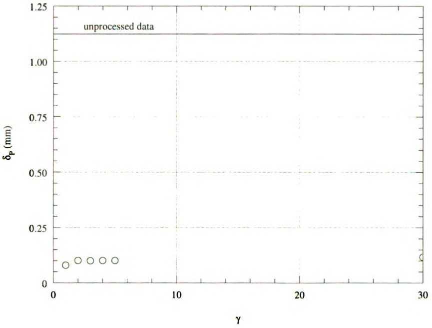

Figure B.2. $\delta_P(\gamma)$, z = 0.8 cm, x = 6.0 cm, unforced.

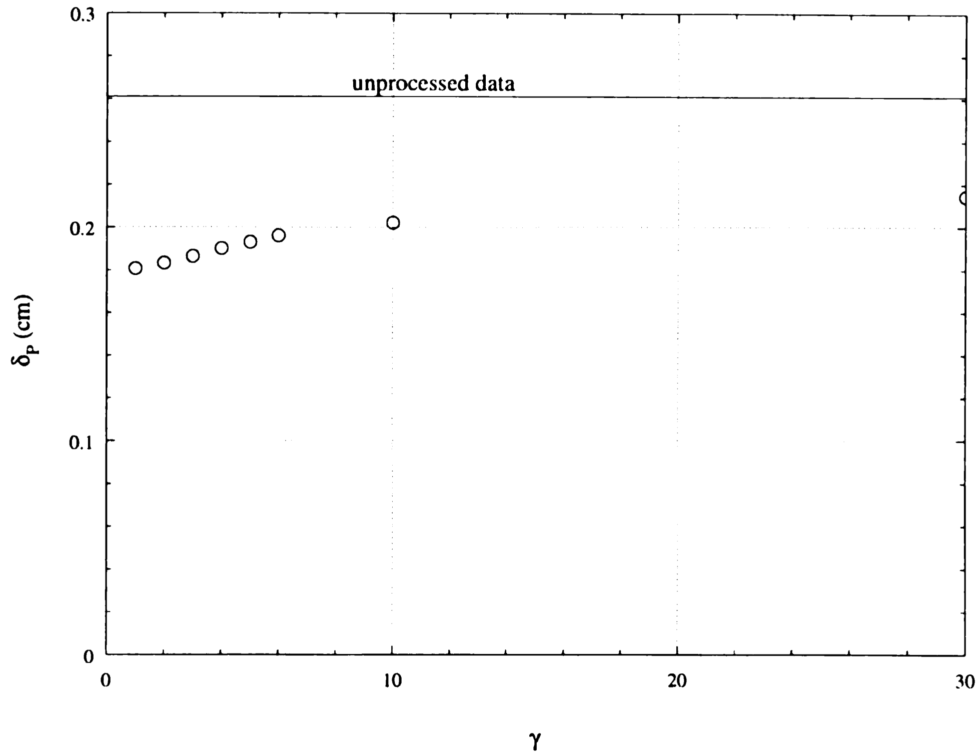

Figure B.3. $\delta_P(\gamma)$, z = 0.8 cm, x = 14 cm, 5% forcing.

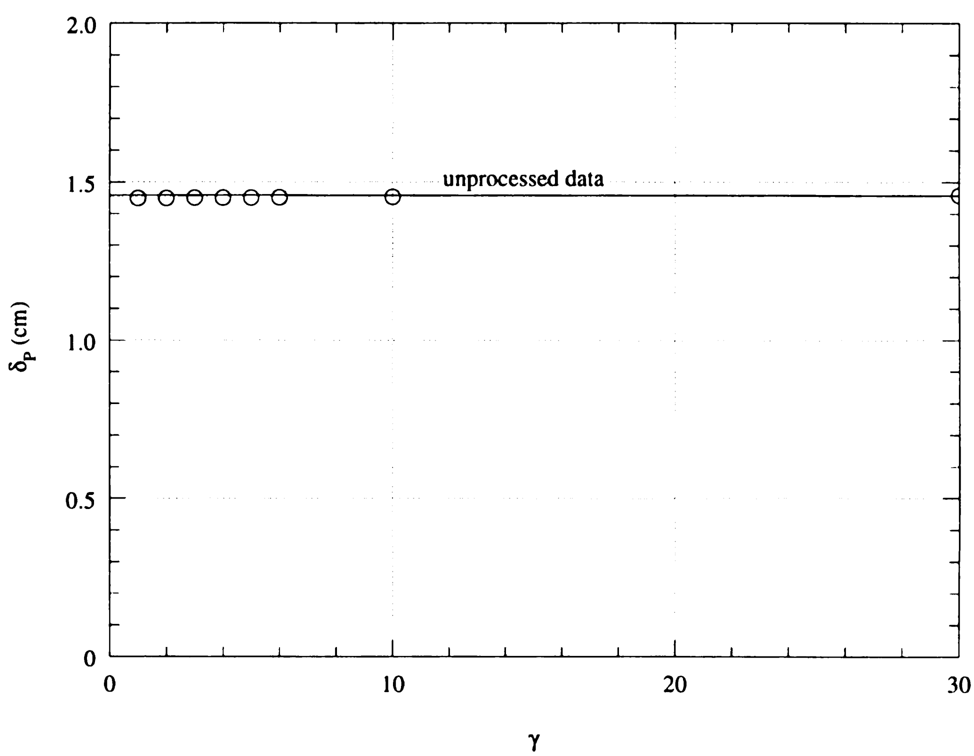

Figure B.4. $\delta_P(\gamma)$, z = -0.8 cm, x = 21 cm, 9% forcing.

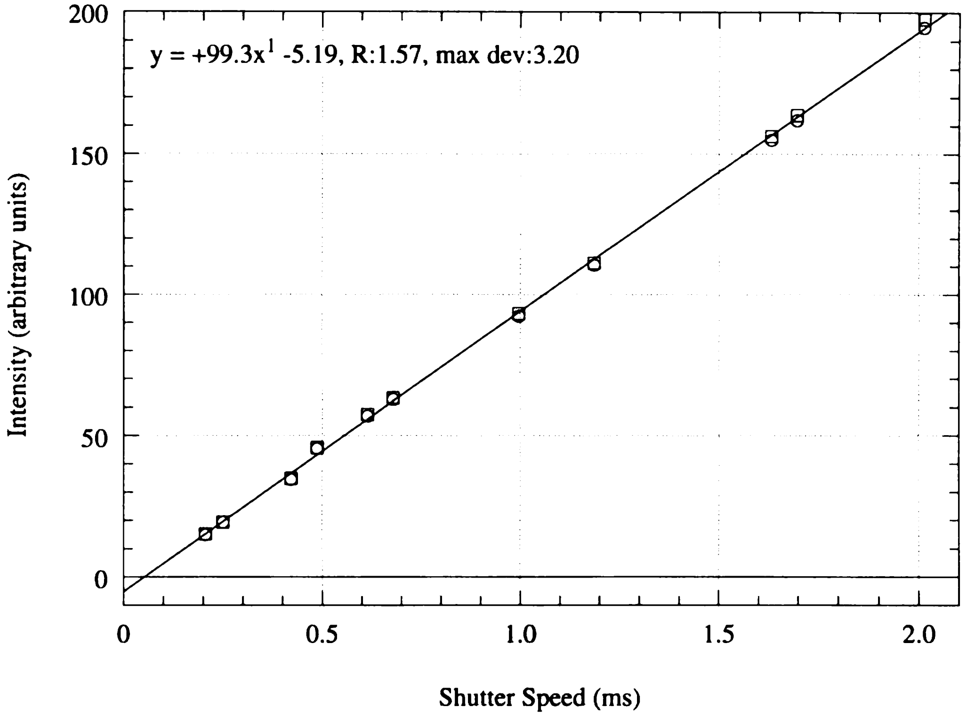

Figure B.5. Intensity versus exposure time for the Sony CCD camera.

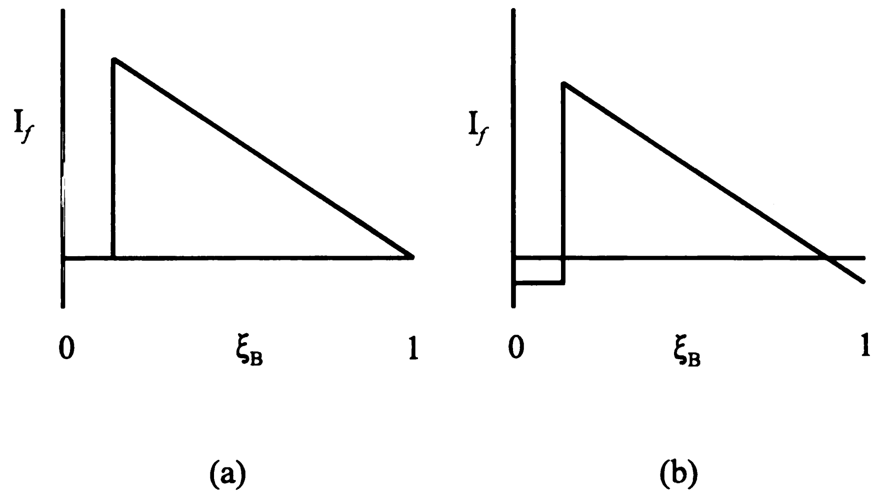

Figure B.6. (a) Example $I_f(\xi_B)$ plot for a camera with zero black level offset.
(b) $I_f(\xi_B)$ plot for a camera with negative black level offset.

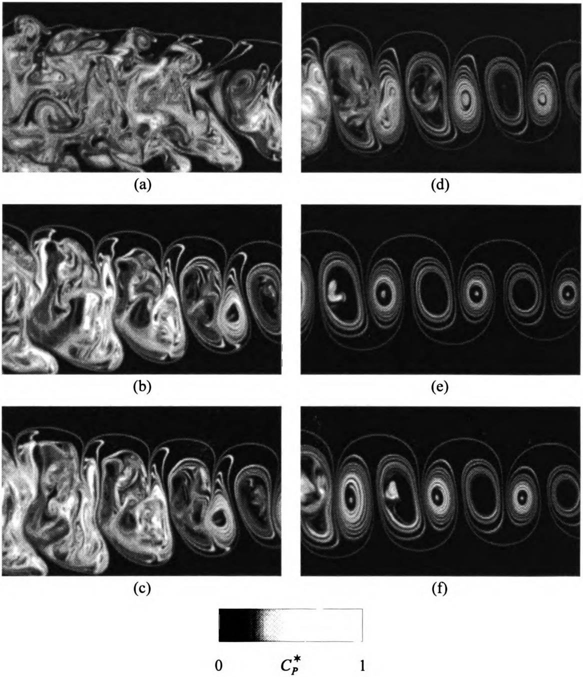

Figure C.1. Chemically reacting LIF images of a wake at different free stream speeds. U_o = (a) 7.17, (b) 8.50, (c) 8.77, (d) 9.94, (e) 11.54, (f) 11.56 cm/s.

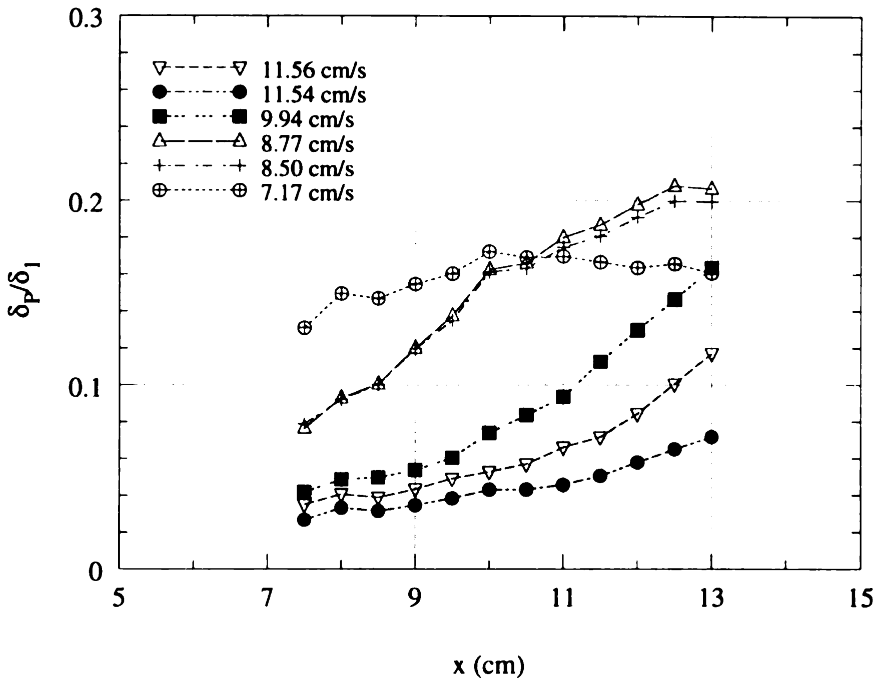

Figure C.2. δ_P/δ_1 versus x for various wake free stream speeds.

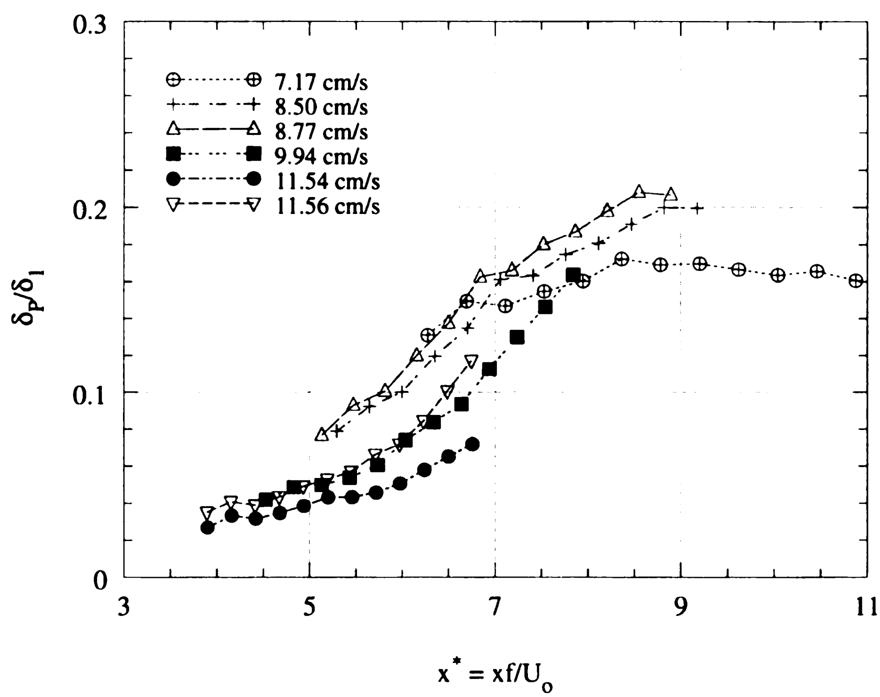

Figure C.3. δ_P/δ_1 versus x* for various wake free stream speeds.

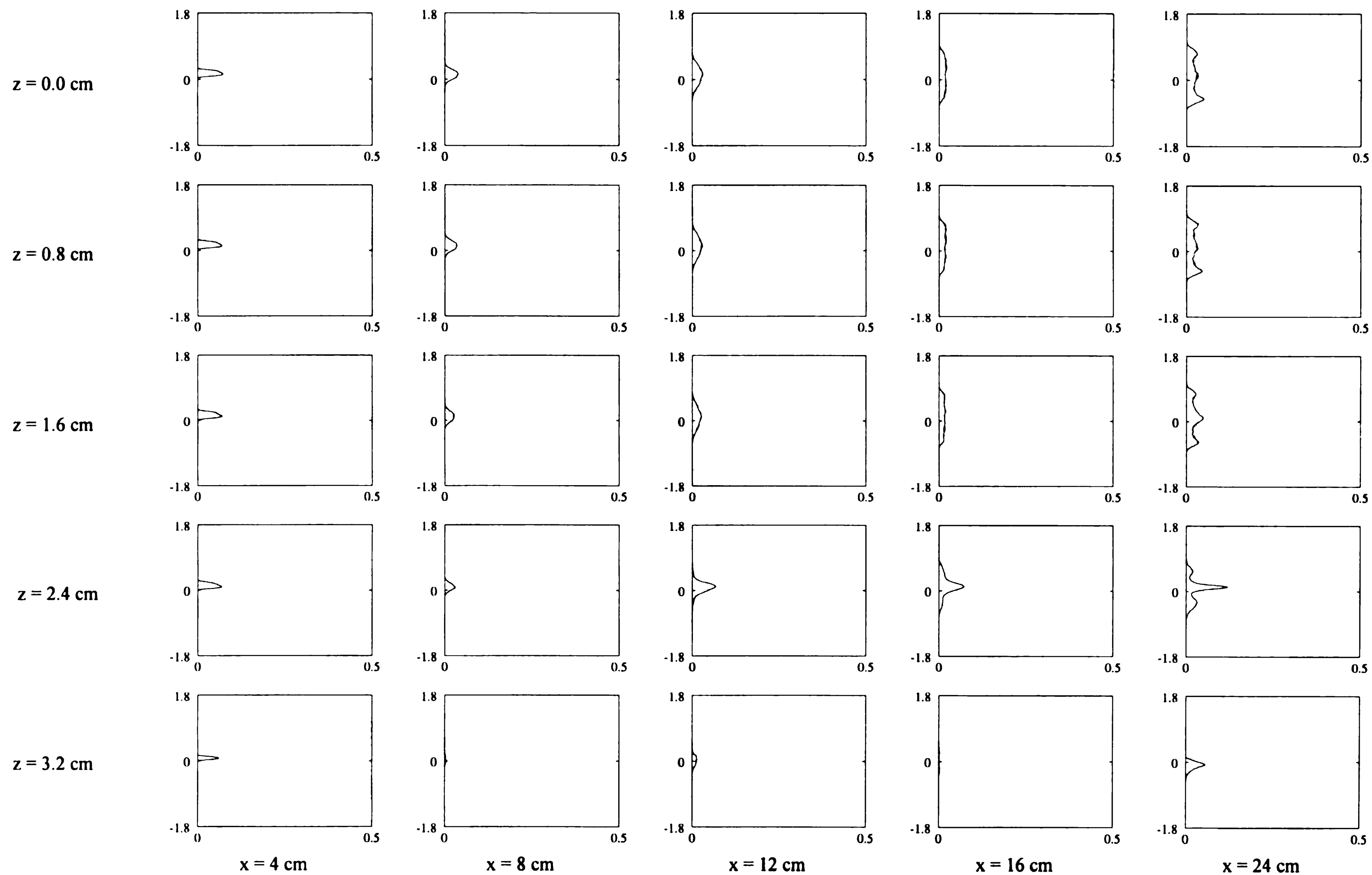

Figure E.1. $\overline{C_P^*}(y)$ profiles at various x and z locations; unforced.

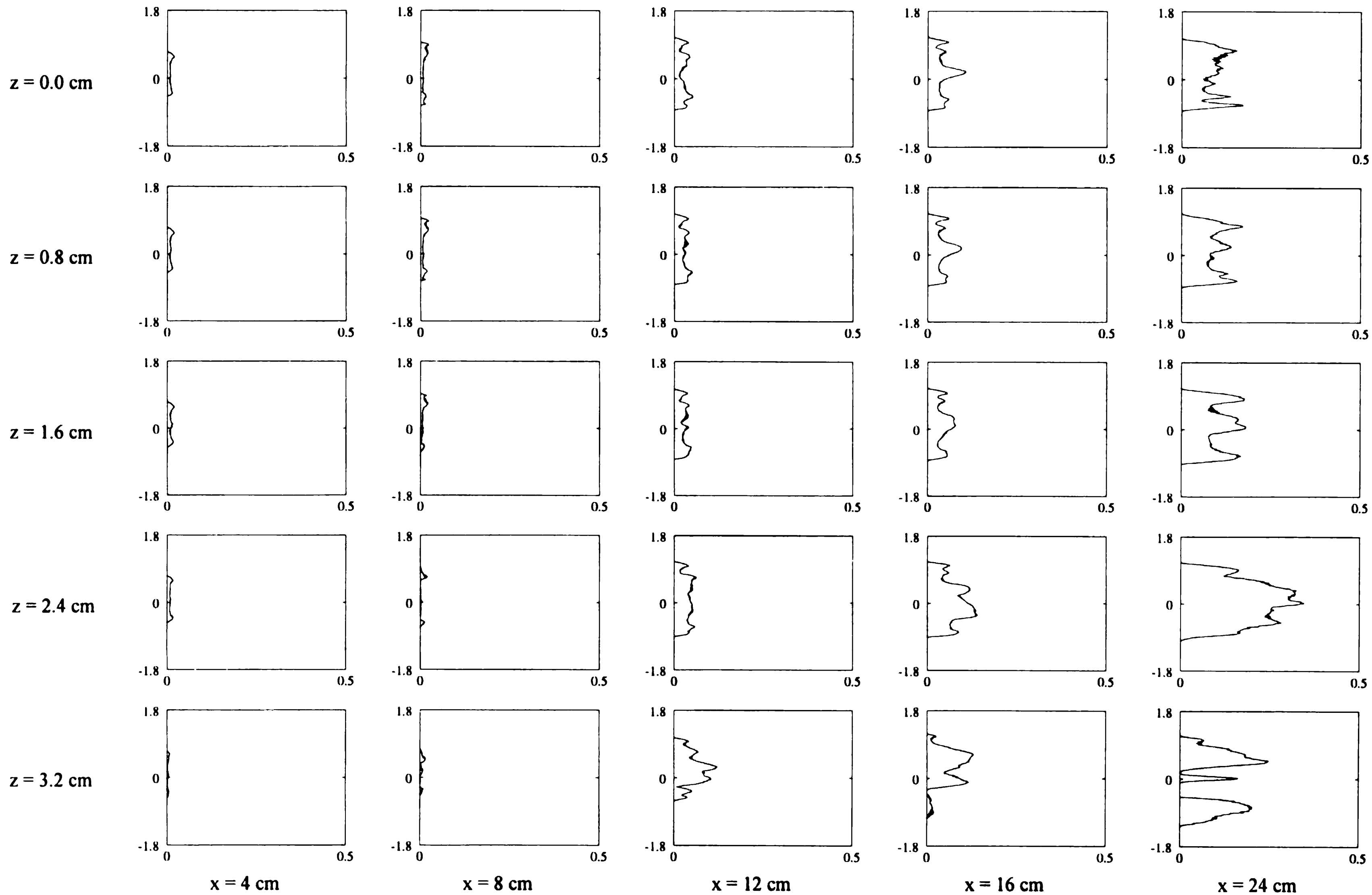

Figure E.2. $\overline{C_P^*}(y)$ profiles at various x and z locations; 2% forcing amplitude.

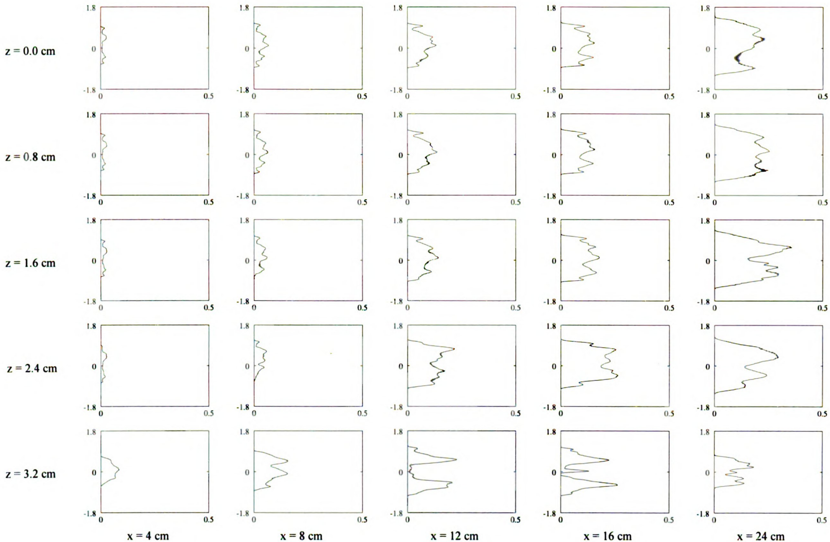

Figure E.3. $\overline{C_P^{\star}}(y)$ profiles at various x and z locations; 5% forcing amplitude.

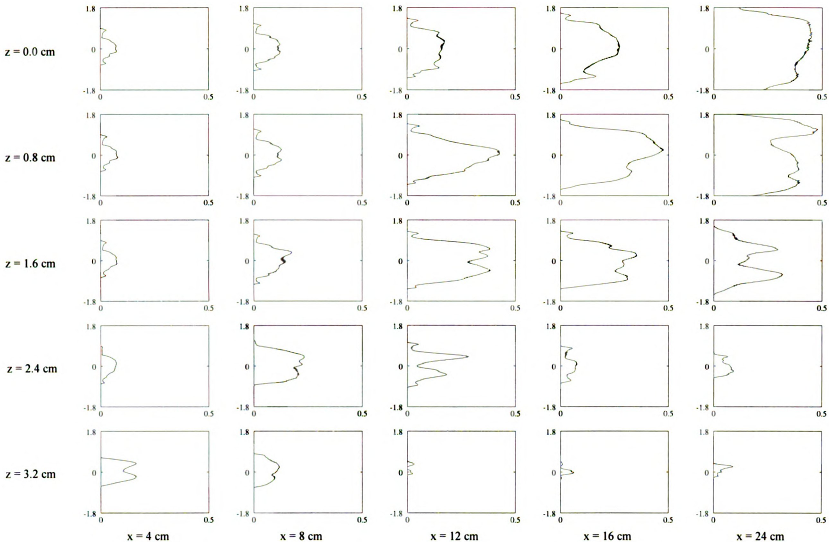

Figure E.4. $\overline{C_P^{\star}}(y)$ profiles at various x and z locations; 9% forcing amplitude.

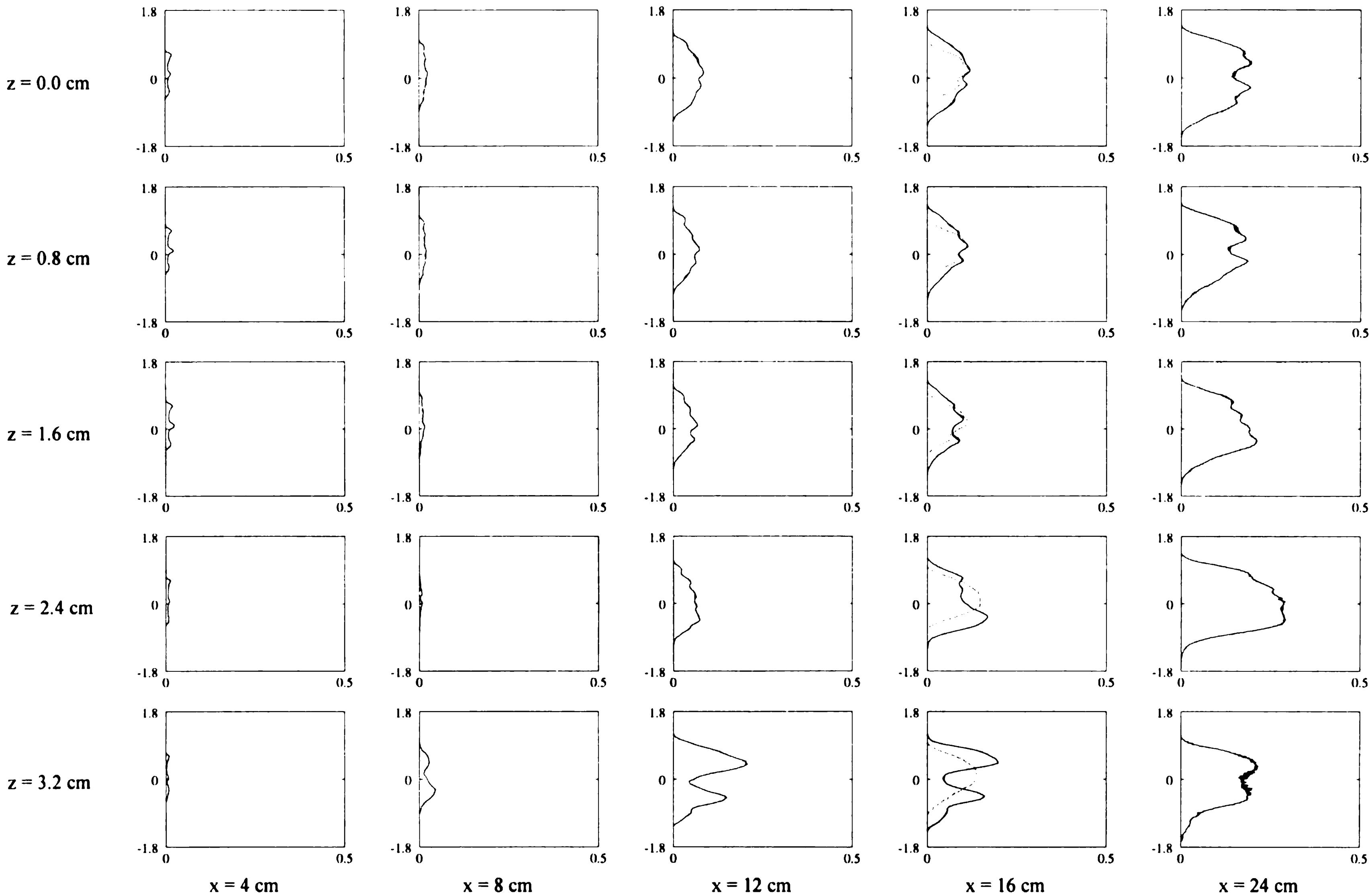

Figure E.5. $\overline{C_P^*}(y)$ profiles for the higher speed wake at various x and z locations. —— forced .... unforced.

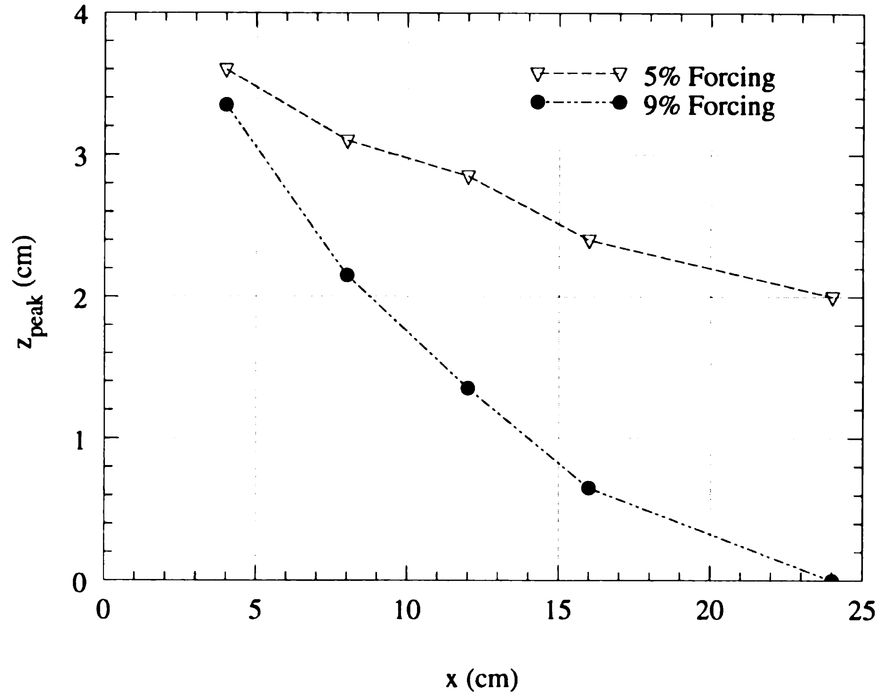

Figure F.1. Z_{peak} versus x from spanwise imaging for 5% and 9% forcing amplitude.

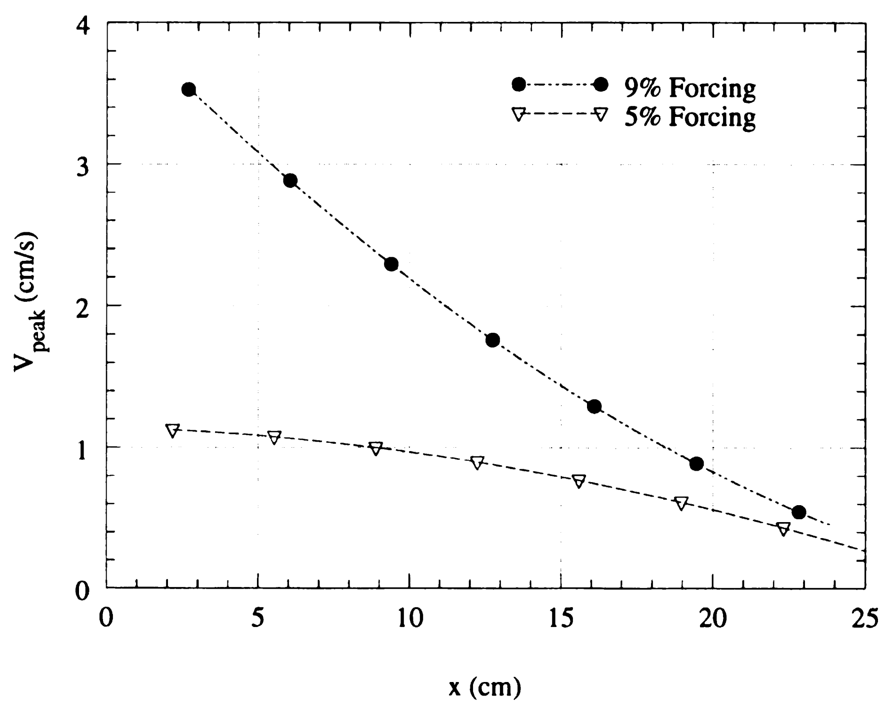

Figure F.2. V_{peak} versus x from spanwise imaging for 5% and 9% forcing amplitude.

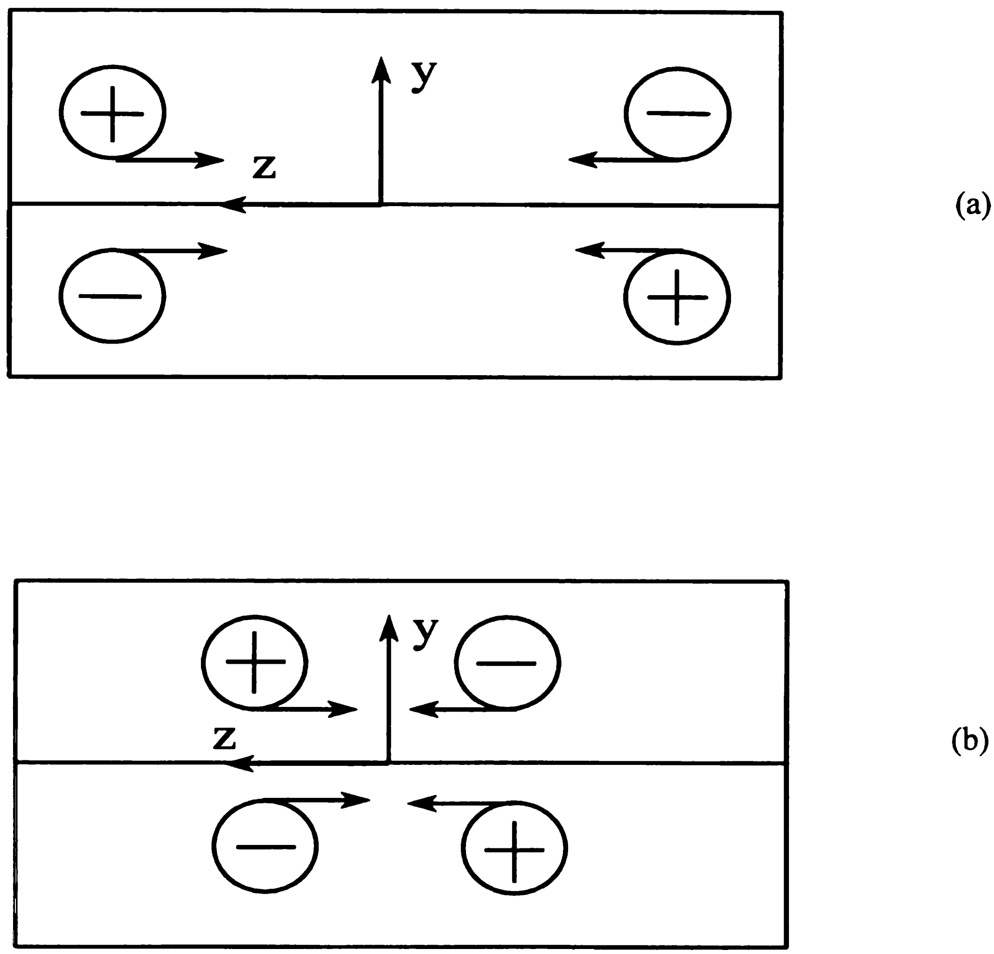

Figure F.3. Model illustrating streamwise vortex evolution. (a) low x, (b) high x.